THÈSE

En vue de l'obtention du

DOCTORAT DE L'UNIVERSITÉ DE TOULOUSE

École doctorale : GEET – Génie Electrique Electronique et Télécommunications : du système au nanosystème

Unité de recherche : LAPLACE – LAboratoire PLAsma et Conversion d'Energie -CNRS-UPS-INPT

Présentée et soutenue par

HOUSSAT Mohammed

Le 25/02/2020

Nanocomposite electrical insulation: multiscale characterization and local phenomena comprehension

Sous la direction de Nadine Lahoud Dignat
et Jean-Pascal Cambronne

Devant le jury composé de :

M. Jérôme Castellon , Maître de conférences HDR, Université de Montpellier	**Rapporteur**
M. Alun Vaughan , Professeur, University of Southampton	**Rapporteur**
M. Philippe Leclere , Directeur de recherche, Université de Mons	**Examinateur**
Mme. Christina Villeneuve-Faure, Maître de conférences HDR, Université Paul Sabatier	**Examinatrice**
Mme. Nadine Lahoud Dignat, Maître de conférences, Université Paul Sabatier	**Directrice**
M. Jean-Pascal Cambronne, Professeur, Université Paul Sabatier	**Co-directeur**

This thesis is dedicated to my parents.

For their endless love, support and encouragement

ACKNOWLEDGEMENTS

Content

General introduction

Due to their low cost, ease of processing, chemical inertness and highly attractive electrical properties, polymer materials have been widely used in electrical insulation systems. However, with the new trends for developing more efficient and reliable electrical insulation in the field of electronics and electrical engineering, polymer insulating materials which contain few weight percent of nano-fillers (usually lower than 10 wt. %), called nanocomposites, have gained increased attention in power systems and high-voltage engineering.

In fact, it was demonstrated that nanocomposite organic/inorganic hybrid materials assure a distinct improvement of their high temperature/high voltage functioning and allow the electrical insulation to strengthen its dielectric properties. Recently, it was shown that some modifications of the electrical properties such as permittivity, dielectric breakdown, partial discharges resistance or lifetime are often awarded to the nanoparticle/matrix interphase, a region where the presence of the nanoparticle changes the matrix properties.

Moreover, recent studies have shown that the nanoparticle surface functionalization allows a better particles dispersion within the host matrix. This better dispersion affects the interphase zone and plays a major role in the nanocomposite properties improvement as well. However, the role of the interphase remains theoretical and few experimental results exist to describe this phenomenon. Accordingly, because of its nanometer scale, the interphase properties characterization remains a challenge.

In the present thesis work, a multi-scale characterization is performed on a polyimide/silicon nitride nanocomposite in order to provide a better understanding of structure/properties relationship in polymer nanocomposite. First, a nanoscale characterization using, among other techniques, the Atomic Force Microscopy (AFM) permits measuring local materials properties based on their surface mapping with an excellent resolution. In this context, AFM is employed to make at the same time qualitative and quantitative measurements of the interphase zones in nanocomposite. The Peak Force Quantitative Nano Mechanical (PF QNM) AFM mode reveals the presence of the interphase by measuring mechanical properties (Young modulus). Electrostatic Force Microscopy (EFM) mode is used in order to detect and measure the matrix and interphase local permittivities. Moreover, the effect of the nanoparticles surface functionalization on the interphase regions is analyzed. Mechanical and electrical quantitative results permit comparing the interphase dimension and properties between treated and untreated nanoparticles.

In addition, a macroscopic investigation on the dielectric properties and breakdown strength of neat polyimide, untreated and treated nanocomposite films is performed. Thus, it is possible to

correlate local observations with the macroscopic behavior of the studied materials. A phenomenological model proposal is given in order to understand the local phenomena that affect this behavior, and thus to be able to predict and tailor them better when designing polymer nanocomposite systems.

This PhD dissertation is divided into four chapters. A brief description of the content of those chapters is given below.

Chapter 1: From dielectrics to nanodielectrics: the role of the interphase

This chapter gives general information about solid dielectrics with a focus on microdielectrics and nanodielectrics. The assumption of the "nano effect" is detailed and related to the interphase concept. Several interphase models found in the literature are exposed. A state of the art of currently used high resolution imaging and characterization methods for interphases probing in composite systems is also presented.

Chapter 2: Materials, sample processing and experimental description

Chapter 2 presents the materials used during this work as well as the different steps of the nanocomposite films fabrication process. Then, the preparation of the different test structures for electrical and morphological characterizations is presented. Finally, an exhaustive presentation of the different experimental techniques used in this work in order to characterize nanocomposite films is given.

Chapter 3: Nanocomposite local measurements

In this chapter, a new approach is performed and allows us to characterize the interphase area using AFM measurements. Indeed, two AFM derived modes are used together (PFQNM and EFM) to determine morphological, mechanical and electrical interphase properties. Conclusions on the effect of the nanoparticle functionalization on the interphase area are also presented.

Chapter 4: Interphase effect on macroscopic properties

The last chapter focuses on the impact of the nanoparticle presence on the electrical properties of nanocomposite materials up to 350 °C. After an analysis of the moisture effect on the electrical properties, the impact of the interphase area will be analyzed through dielectric spectroscopy and dielectric breakdown field measurements. Finally, a phenomenological approach to correlate nano and macro behaviors is presented.

1. From dielectrics to nanodielectrics: The role of the interphase

Content

1.1. Introduction

In the history of electrical insulation, the introduction of a truly new insulating polymer is quite a rare event. The majority of "new" systems have often involved the use of additives to existing materials, blends and copolymers, etc. However, today's research on advanced materials for electrical engineering applications working under sever constraints (high temperature and high electrical stress) is needed. For example, particular type of polymer composites with required dielectric properties can cater the need for pulse power energy storage systems with high energy density by combining the scope of processibility and breakdown field strength of polymers along with materials of high dielectric constants (such as ceramic fillers).

This first chapter highlights the current state of polymer composites used for insulation in electrical engineering applications. Then, a state of the art of the most recent studies and results concerning the dielectric properties of micro and nanocomposites materials will be detailed, specifically for dielectric spectroscopy (permittivity, conductivity, loss factor), breakdown field strength and space charge measurements. Then, the "nano effect" will be described leading to the introduction of the "interphase", a region between the matrix and fillers with properties different from both the matrix and fillers. The role of this interphase in the enhancement of nanocomposite macroscopic properties will be also detailed. Afterwards, a state of the art of existing models to describe the interphase is presented. A focus on various recent investigations of particles surface functionalization to improve the compatibility with polymers and therefore to modify the interphase area will be exposed.

To finish, nanoscale interphase characterization techniques are introduced. A special interest on using Atomic Force Microscopy (AFM) to study the interphase is addressed. The last part focuses on Peak Force Quantitative NanoMechanical (PFQNM) and Electrostatic Force Microscopy (EFM) modes used to highlight the presence of the interphase and measure its local properties.

1.2. Dielectrics for electrical insulation

Solid state matter is divided into three main types of materials: metals, semiconductors and insulators. The latter are also called "dielectrics". These three categories are defined and classified according to their electrical conductivity, or more precisely, to the state of their electron energy bands, and mainly, to the width of the energy gap between their valence and conduction bands. The boundary between a dielectric behavior and a conductive one is not absolute. The matter can be sometime conductive, sometime insulating, depending on its intrinsic and external conditions. The major electrical properties usually considered in selecting an insulation system may be its electric strength, relative permittivity and dielectric loss (as typified by the loss factor).

Dielectric materials are widely used as electrical insulation in a wide variety of applications, from microelectronic components as electronic circuits encapsulation to eliminate and prevent any electrical short-circuit, to components in the space environment, such as satellites. Moreover, dielectrics are usually used in power cables for electrical energy transmission and in capacitors for energy storage etc. Many polymers are dielectrics, which have poor bulk conductivity and can survive high electric fields as they have no free charge carriers and large band gaps in their electronic structures.

Polymer materials have been used in electrical insulation systems and have shown great interest in the fields of microelectronics and electrical engineering due to their low cost, ease of processing, chemical inertness and highly attractive electrical properties. Polymers are known to have high dielectric strength, good mechanical properties but low permittivity and thermal conductivity [1] . Otherwise, ceramics present high dielectric permittivity (from 10 to 1000) [2] and high thermal conductivity (from 10 to few 100 $W.m^{-1}.K^{-1}$) [3]. However, they often exhibit a relatively low dielectric strength (compared to insulating polymers) [4], poor mechanical resistance and are not easy to process.

In the field of plastic engineering, polymer/ceramic composite materials are typically desired to be employed instead of neat polymers due to their enhanced performances involving high mechanical strength, heat resistance, thermal endurance and chemical stability, etc. Moreover, the advantage of these composite materials is that they often offer the advantages of both polymers and ceramics in the field of insulation materials. While composites are an interesting mean to improve physical properties, micro and nano-composite materials are a promising way of research to get even better results, not only to increase composite material characteristics, but also to create unique properties [5]. Depending on the matrix nature, nanocomposites can be classified in three major categories: polymer matrix nanocomposites, metal matrix nanocomposites and ceramic matrix nanocomposites [6]. In the field of insulation, polymer mico/nano composites show a distinctive advantage and offer promising concepts for the next generation of high-voltage applications [7] (figure 1-1).

Figure 1-1. The next generation of high-voltage applications employing polymer-based nanocomposites .

1.3. What about micro and nano dielectrics

1.3.1. Microcomposites dielectric properties

In polymer composites, fillers often give a specific property to the insulating structure such as enhanced permittivity, breakdown strength, thermal or mechanical performance, etc. Several examples can be found in the literature of enhanced properties in composites. Fiber-reinforced plastics (FRP), which are composed of epoxy resin and glass/carbon fibers, are widely used in various applications. Results of SiC (5 wt %) filler addition showed higher mechanical properties compared to unfilled epoxy. It has been found that the tensile strength, flexural strength, and hardness of the glass reinforced epoxy composite increased with the inclusion of SiC filler. However, a drastic reduction in dielectric constant after the incorporation of conducting SiC fillers into epoxy composite has been observed [8]. Moreover, Desmars *et al.* in their work on h-BN epoxy microcomposite (epoxy composite Ep-30N filled with 30 wt% of micron sized h-BN), have demonstrated the effect of the microparticle addition that managed to lead to a significant decrease in the overall conductivity values. The addition of micro h-BN to the epoxy matrix leads to an improvement of many properties amongst the one required for high voltage insulation. The influence of the electric field E upon electrical conductivity of neat epoxy and Ep-30BN at 60°C is given in figure 1-2. Both materials exhibit a region of constant low conductivity at low fields, followed by an increase in conductivity at higher fields [9].
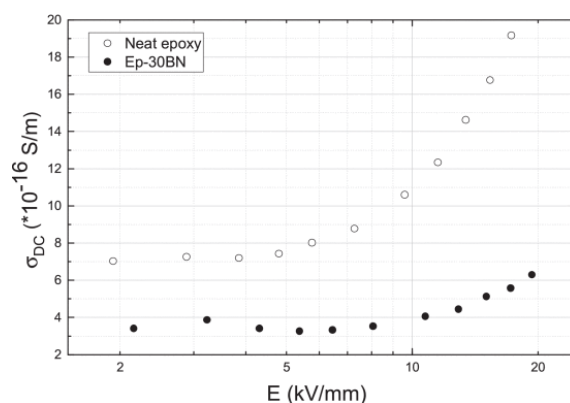
Figure 1-2. Influence of electric field E upon conductivity

In addition, Alias *et al.* have revealed that the performance of PI films can be improved by incorporating Al_2O_3 into the PI matrix. Figure 1-3 shows the evolution of the permittivity and loss factor of a PI/Al_2O_3 (500 nm) as a function of the loading rate. As it can be seen, the dielectric constant increases from 3 to about 6 with only 30 wt% Al_2O_3 loading, whereas the dielectric loss increases from 0.005 to around 0.008 at a sweep frequency of 1 MHz. Meanwhile, the thermal properties of PI film have been improved with the addition of Al_2O_3 [10]. However, the increase in permittivity and thermal conductivity are still limited compared to bulk ceramics, even at high filler content (>20 vol%). Typically, at very high filler content, a value of 200 can be obtained for the permittivity of an $epoxy/SrTiO_3$ (90 vol%) composite [11] or below 10 $Wm^{-1}K^{-1}$ for a polyimide/ AlN + BN (70 vol%) thermal conductivity [12]. Hence, it is not surprising that such high filler content should weaken the mechanical properties as well.
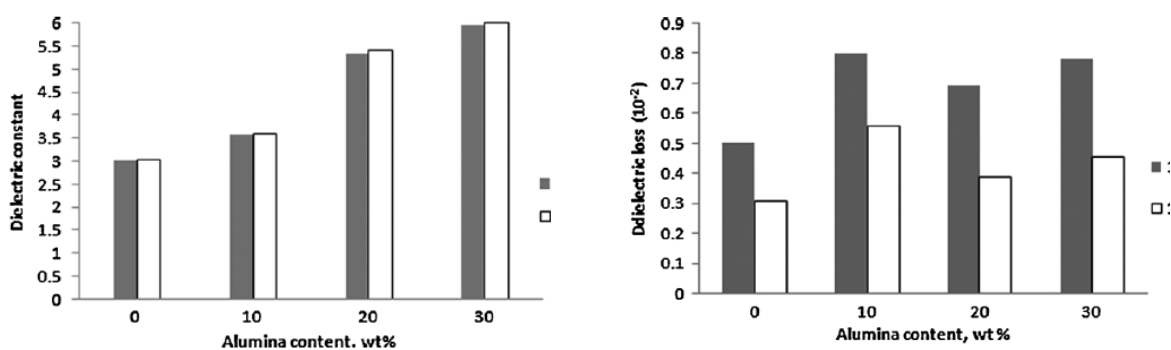
Figure 1-3. PI/Al_2O_3 (0,5 μm) Permittivity and loss factor

1.3.2. Comparison between micro and nano composites dielectric properties

The introduction of nano-sized fillers to insulating polymers has demonstrated multiple properties improvements such as the increase of the breakdown strength and the time to failure, the decrease of the trap controlled-mobility and space charge accumulation at medium fields. These improvements have been commonly noticed upon filler size reduction [13]-[14]. Nanocomposites

differ from traditional composites in three major aspects: first, they contain a small amount of fillers (usually less than 10 wt % vs. more than 50 wt % for microcomposites), second, filler is in the range of nanometers in size (10^{-9} m vs 10^{-6} m for composites) and finally, they have tremendously large specific surface area compared to micro-sized composites [5]. An example, which illustrates these mechanisms, is shown in figure 1-4, taken from Nelson and Fothergill on an epoxy system filled with titanium dioxide microparticles compared to nanoparticles [14]. At high frequencies the micro-composite has a higher relative permittivity, probably because the filler has a high permittivity ($\varepsilon_{TiO2} = 99$). In the other hand, at low frequencies a less pronounced interfacial polarization is revealed in nano-composite compared to base resin and micro-filler. For instance, at 1 kHz, the measured real permittivities are: 9.99 (base resin), 13.8 (micro-composite) and 8.49 (nanocomposite). It is interesting that the nanocomposite has a lower permittivity than the base resin. This may be in part due to the very small size of the particles giving rise to limited cooperative movements of dipolar reorientation within them, but it is probably also due to the restriction by the nanoparticles of movement of end-chains or side-chains of the epoxy molecules [15].
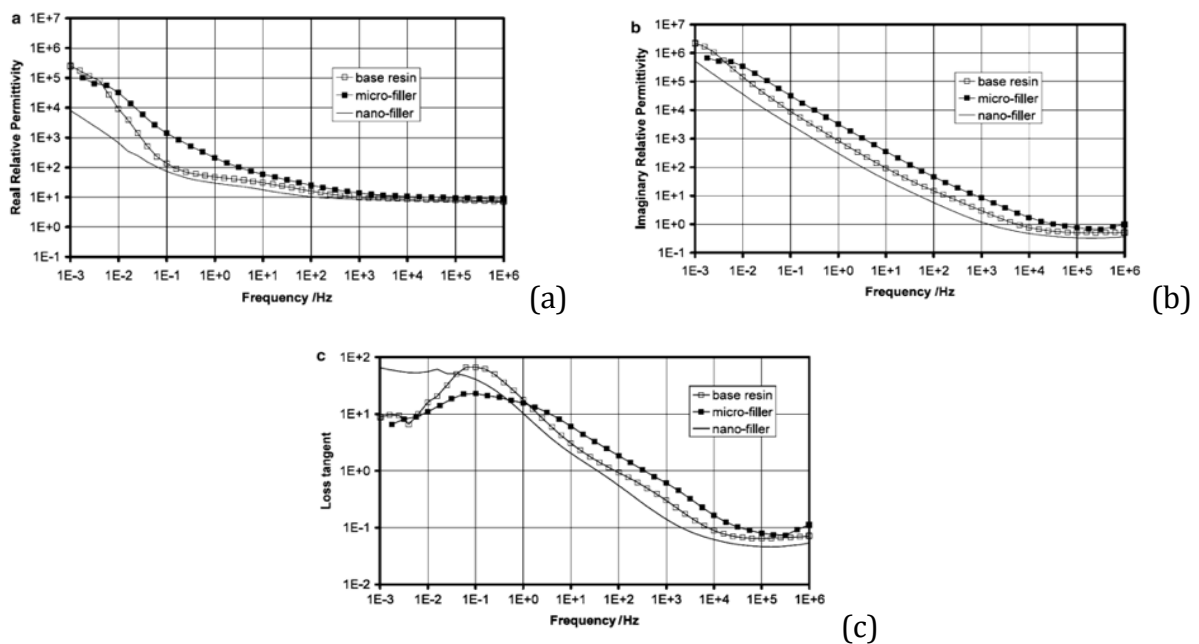
Figure 1-4. Dielectric response of TiO_2/epoxy composite (a) real and (b) imaginary parts of permittivity and (c) loss tangent

In this section, a comparison between epoxy and epoxy/ceramics (micro and nano) composites dielectric properties is presented in order to establish trends in the particle size effect. In this context, J. Castellon *et al.* have analyzed the dielectric behavior of an epoxy-based materials with different contents of micro and nanoparticles of silica, where the weight %-content of the silica

fillers and the particles size were varied. Figure 1-5 shows the frequency dependence on the dielectric permittivity and the dielectric losses factor. At low frequencies, the high values of the dielectric permittivity (those containing micrometric silica) correspond to those exhibited by a polar material. In other hand, at low frequencies the values of dielectric losses factor generally give information on the material conductivity. Thus, it would appear that materials containing micro fillers are more conductive than neat epoxies [16].
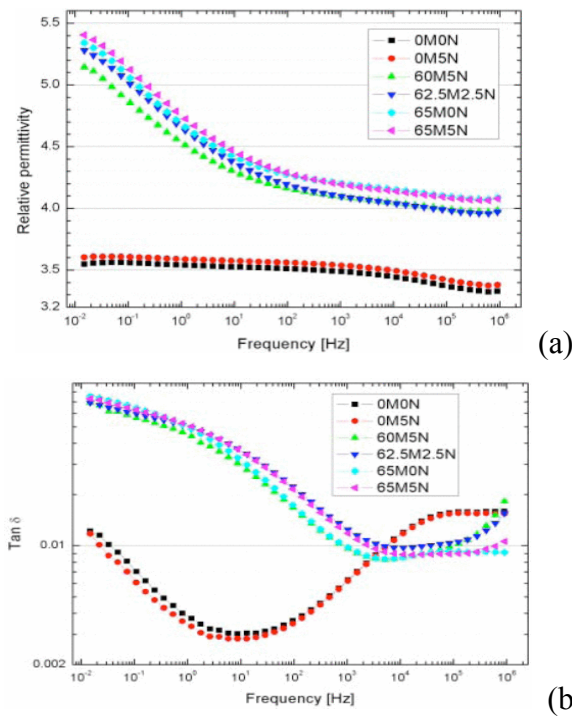
Figure 1-5. (a) Dielectric permittivity and (b) losses factor spectra at 60°C

Furthermore, it can be noticed from [14-20] that epoxy-based nanocomposites have demonstrated some advantages in both mechanical and dielectric properties compared to pure resin systems and epoxy resin composites with micro-fillers at low concentration (1−10 wt %). It was found that over a wide range of frequencies, the permittivity values of epoxy nanocomposites were reduced significantly compared to the base resin and epoxy micrometer-size filler at low concentration. It was also revealed that the reduction of the permittivity values strongly depends on filler type as well as filler size [20,21].

1.3.3. Comparison between micro and nano composites breakdown strength

It is highly attractive to boost the dielectric constant of a polymer composite in the order of hundreds or even thousands by using suitable inorganic fillers with higher level of permittivity in comparison to that of the polymer matrix at very high size and content. As a consequence, to realize this practical expectation, an increase in the effective dielectric constant comes through an

increase in the average field in the polymer matrix that allows relatively little energy storing capacity in the high permittivity phase. Moreover, it is also possible to cause a loss in compatibility between the polymer matrix and the filler that may contribute to poor level of homogenous composite. In addition, there are chances that the large contrast in permittivity between two phases can lead to highly inhomogeneous electric field [22].

In order to study the behavior of the micro and nanocomposites, Zhe *et al*. have shown the role of nano-filler on dielectric breakdown strength of micro and nano Al2O3 / epoxy composites. From figure 1-6, it is clear that micro-composite has a lower breakdown (BD) strength as compared to neat epoxy. BD strength decreases by about 60 % from 202 to 88.3 kV$_{rms}$/mm. It increases by 8.2 % from 88.3 to 95.6 kV$_{rms}$/mm when the microcomposite is loaded by nano-fillers. However, the modification of the inorganic filler surface by a coupling agent achieves suitable compatibility of the inorganic filler with the polymer matrix and seems to have a small effect on BD strength in this case [23]. Moreover, epoxy-layered silicate nanocomposite has higher insulation breakdown strength than that of an epoxy resin without layered silicate fillers. The electrical treeing progress with many branches in the nanocomposite seemed to result in an increase in insulation breakdown strength [24].
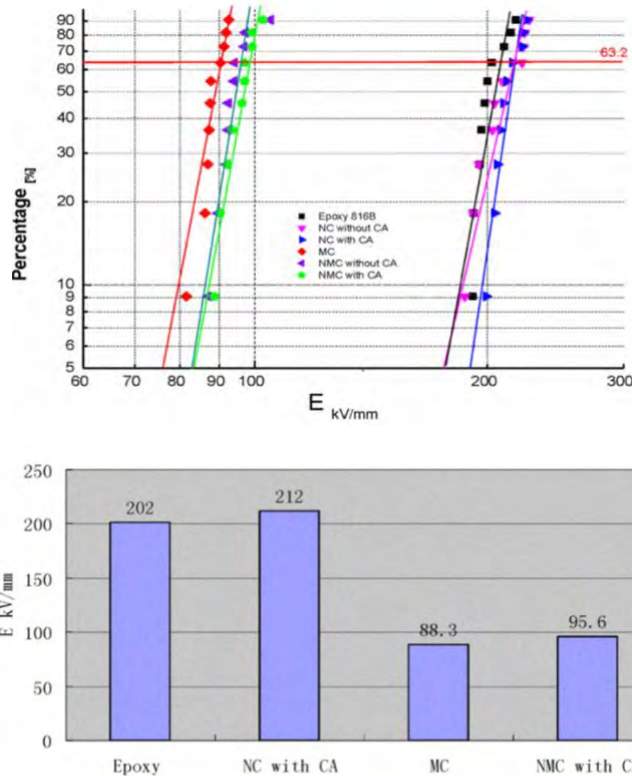
Figure 1-6. (Top) Weibull distribution of breakdown strength evaluated for 4 kinds of samples by the sphere-flat sample-sphere electrode system and (bottom) the breakdown strengths (percentage is 63.2%). NC: Nano-composite, MC: Micro-composite, NMC: Nano-micro-composite, CA: Coupling Agent

1.3.4. Micro and nano composites space charge accumulation

The accumulation of space charge has a huge influence on dielectric properties of insulation systems. Earlier researches in this field showed that the accumulation of space charge could affect the internal electric field which can present important local intensifications and may lead to partial discharges, electrical treeing and to an early breakdown of the insulation [25]–[27]. Consequently, it is very important to reduce space charge accumulation and its influence on dielectric behavior of insulating materials. Recent investigation showed that the presence of nanofillers in epoxy resin affects the space charge accumulation in polymer matrix [28][29][30]. Results obtained from J. Castellon *et al.*, highlighted the influence of the content of silica on the electrical properties [25]. The best ratio between micro and nanoparticles contents could be unraveled as indicated by a reduced space charge accumulation as presented in figure 1-7 [28]. Moreover, several works revealed that epoxy nanocomposites could accumulate less charge than neat epoxy resins [27]. It was also observed that epoxy nanocomposites provide faster charge dynamics, especially for negative charges [31]. Thus, it is important to study the influence of matrices and the chemical structure of fillers on the space charge accumulation in order to avoid and/or reduce their influence on the lifetime of polymer composites used in electrical engineering.
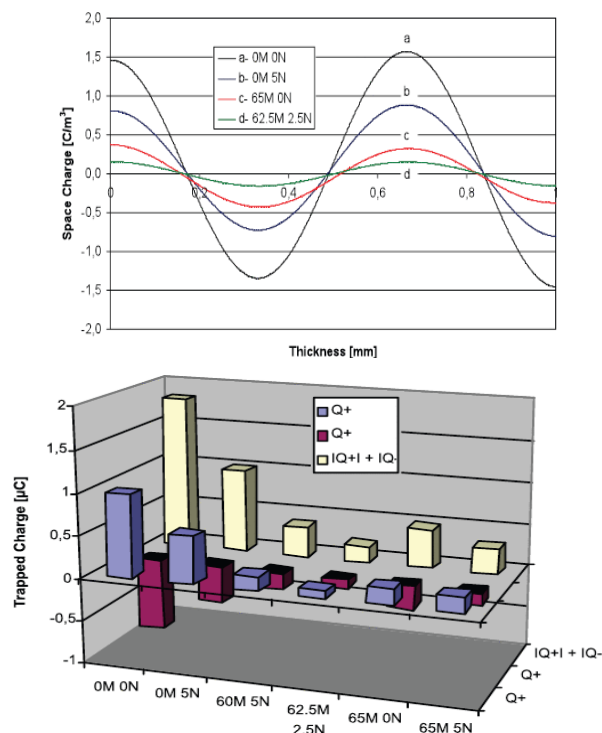
Figure 1-7. (a) Space charge profiles on each material and (b) total trapped charge for each material

1.4. The nano-effet leading to the Interphase concept

Due to the complexity of nano and micro-fillers interactions with the matrix, there is a large number of variables that can adjust novel properties in the final materials, which could be interesting for scientists and material engineers [32]. At the nanometric level, the behavior of any material becomes predominantly monitored by the properties of its interface with the surroundings [33]. In fact, as the size of a spherical particle, for example, is reduced, the number of atoms and molecules present at its surface increases exponentially compared to the ones present in its volume. Consequently, the state of surface molecules will tailor the physical properties of the particle, if it is used alone, or if it is mixed with another material. The properties of the surface differ from the volume since surface molecules and atoms of a condensed phase exhibit lower number of bondings with the bulk phase, increasing their reactivity [34]. At very low dimensions, quantum mechanical effects can also arise, changing casual bulk particle properties [35]. Indeed, the origin of the properties modification between nano and micro composites is based on the assumption that the use of nanoscale filler particles causes a highly increased interfacial area (see figure 1-8).
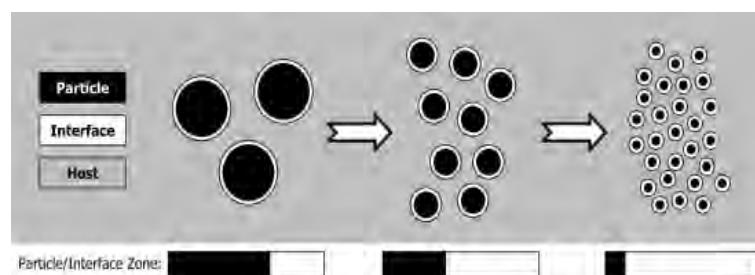
Figure 1-8. Schematic representation of the ratio particles/interfaces changes with the size of the filler

The interface properties in nanocomposites are of the most importance, explaining most of their macroscopic behaviors; particulary, their electrical properties. Indeed, it is suggested that the interface area is not a simple boundary, but rather involves an interaction zone (introduced by Lewis in 1994 [36]). In that sense, a truly new material is formed, it may not behave in the same way as the base polymer from which it is derived. Thus, it is evident that the challenge is to engineer the interaction zone in a way that provides the desired properties. Moreover, it is interesting to note that, in Finite Element Analysis (FEA) for example, an interface is typically modelled in zero dimensional terms, but in practice it is not simply the point at which the matrix ceases and the particle reinforcement begins. In the current context, the interface may be described as the boundary between two layers of different chemistry and/or microstructure. However, such boundaries are rarely devoid of chemical interaction, and therefore we can also define a region, called the interphase as a three-dimensional zone (distinct from a two-dimensional interface),

representing the volume of material affected by the interaction at the interface. Such an interphase zone will lead to a properties gradation from one phase to another rather than an abrupt change observed in a two-dimensional interface. Furthermore, the nature of such interactions in the interphase varies considerably from one reinforcement/matrix system to another and complete chemical definition of the nature of such interactions is rare.

However, without being concerned with the exact nature of these interaction zones, figure 1-9 shows how they might look (a) for a conventional micron-sized filler and (b) for a nanofilled material. Although it's clear that the interfacial region surrounding the particles is dominant for the nanocomposite, whereas it is insignificant for the conventional material. It is also evident from figure 1-9(c) that, as the particule size is reduced (below 100 nm) the specific surface area becomes very large even for filled materials with quite modest loadings. Moreover, the surface area associated with these internal interfaces becomes dominant and the proportion of the total material, which appears at the interface, starts to become very significant [37]. In fact, it becomes clear that, for a nanocomposite, most of the bulk material is composed of interface. Consequently, although the composite may have been compounded from a base polymer and a nanometric inclusion, the properties of the resulting composite may be more likely to resemble those of the interaction zones rather than those of the original constituents [37].
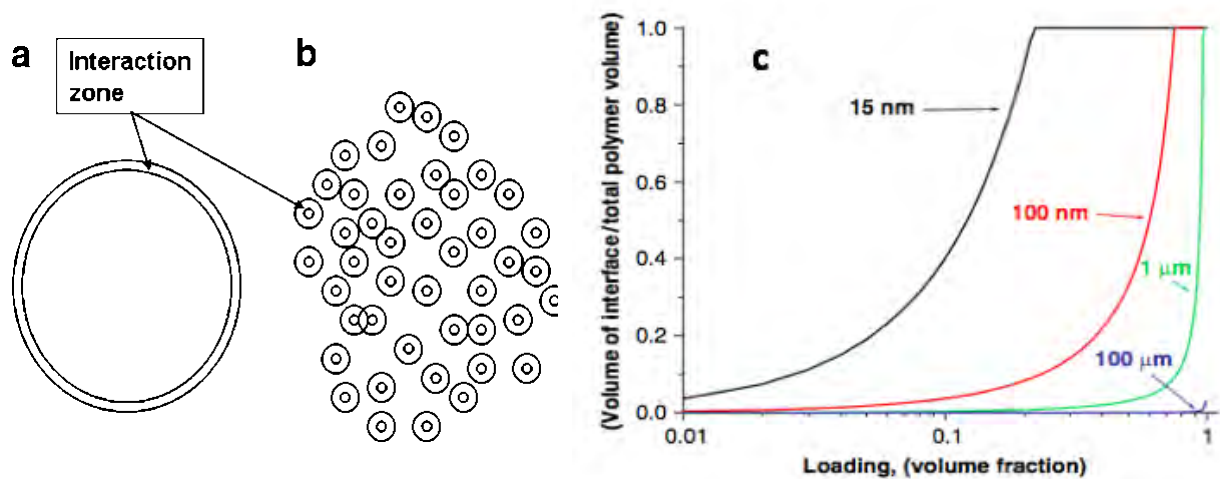
Figure 1-9. Representation of interactions zones for (a) a microparticle and (b) an assembly of nanoparticles (not to scale), (c) Surface-to-volume ratios of nanocomposites as a function of nanoparticle loading

J. Keith Nelson and John C. Fothergill have noticed that the incorporation of a nanometric particles results in a substantial change in the behavior of the nanocomposite. The anomalous behavior of nanocomposites has been attributed to the nanometric size of the fillers (the nano effect)[14]. At this scale, and for the same weight of material, the ratio of atoms and molecules present at the surface of the nanoparticles regarding the bulk ones increases exponentially compared to

microparticles. Moreover, the reactivity of surface molecules of a condensed phase is high. At the contact with another phase, a series of interactions occurs at their mutual interface in order to establish a thermodynamical equilibrium. Indeed, the nanoparticles/matrix interface leads to the formation of an interaction zone between inorganic fillers and organic polymers. In the same way, since nanocomposite are composed of nano-sized fillers embedded into the polymer matrix, the regions at the interaction zone between particle and matrix possess special intrinsic properties and occupy a high volume in the material. Moreover, these interactions zones favor the emergence of a region with unique properties different from both the matrix and filler (commonly called the interphase presented in figure 1-10) [38]. As a consequence, material properties which rely on mechanisms taking place at the interphases become altered. Because of the difference on the interface bonding strength between polymer and particle, this region can have a higher or lower mobility than the bulk material. Interphase represents the key to understand mechanisms and phenomena which control the properties of nanocomposites used as advanced dielectrics.
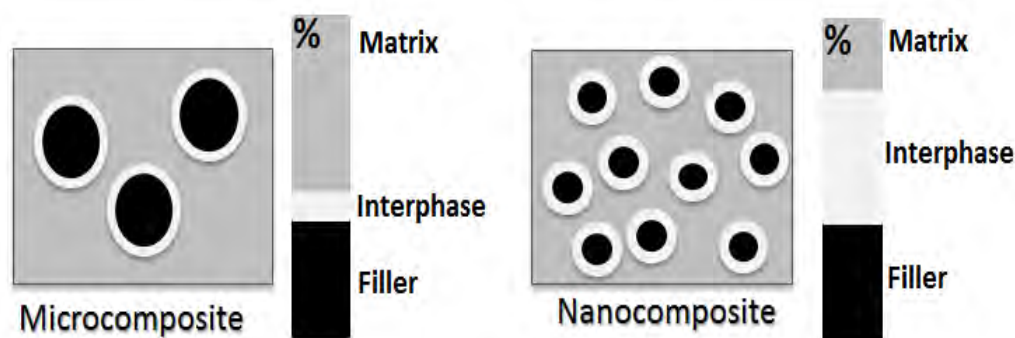
Figure 1-10. Sketch illustrating the percentage of interfacial regions for the same amount of filler in a composite, for micron-sized particles compared to nano-sized particles

Thus, a field of research (around 2000) in the domain of electrical insulation was born: Nanodielectrics, a nowadays popular term in the dielectrics community, has been the subject of intensive research over the past 10 years. Whereas polymer nanocomposites concern polymers within which nanometer-sized fillers are homogeneously dispersed at just a few weight percentages (wt%), the term "nanometric dielectrics," [36] or "nanodielectrics" [39][40], refers to nanocomposites of specific interest in connection with their dielectric characteristics. Nevertheless, for the scope of HV electrical insulation research, the terms "nanocomposites" and "nanodielectrics" are used interchangeably to refer to polymer/ nanoparticle mixtures of dielectric interest.

1.4.1. Interphase role in nanodielectrics

The interphase region is considered to extend from the surface of the particle through a region of modified polymer, until the polymer properties resume those of the host polymer. Thus, the inorganic particle surface is included in the interphase area. The influence of the interphase on the dielectric properties of epoxy/silica composites was studied by Sun et al [41]. They found that permittivity and tan(δ) of nanocomposites were higher than of micro-composites at low frequencies. S. Diaham et al, have studied the effect of boron nitride nanofiller size in polyimide/boron nitride (PI/BN) nanocomposite films from 20 to 350 °C. At low filler content (1–2 vol.%), the results show very large improvements of the electrical insulating properties at high temperature (> 200 °C) particularly for the smallest BN nanoparticle diameter [42]. Another study has provided a characterization of micro- and nano-particlte of Titanium Dioxide (TiO_2) when embedded in a resin matrix. Various electrical insulation properties, such as relative permittivity and space charge formation are improved with nanofiller addition compared to their unfiled and micro filled [43]. Moreover, It was found that the addition of Si_3N_4 into epoxy nanocomposite presents a good approach to increase the dielectric breakdown strength and partial discharge resistance. It was also clarified that the dispersion level of nano-fillers is the key failure factor in BD strength process [44].

The role of interphases was also emphasized in [45], where it was shown that nanocomposites with higher interphase content have a higher resistance to tracking and erosion than nanocomposites with lower interphase content. In [46], the role of the interphase between silica nanoparticles and the organic polymer (epoxy resin) through the silane coupling helps to reduce the mobility of charge carriers and thus increase the partial discharge resistance.

In the same way, since particle/particle interactions induce aggregation, matrix/filler interaction leads to the development of an interphase. Van der Waals forces play a crucial role in the development of nanoparticles/polymer interactions. Moreover, it's necessary to mention that, single particles tend to agglomerate due to their interfacial tension and the properties of composites are altered. Therefore, the surface treatment of particles is very important to achieve homogeneous distribution, to avoid any cluster formation in the polymer composite and to improve the adhesion between the polymer and the filler [47]. Nanocomposite properties are usually modified by the surface treatment of the filler. Reactive treatment, i.e. coupling agents are mainly applied in the preparation of spherical nanoparticles and the formation of the associated polymer nanocomposites. Coupling agents are typically fairly low molecular weight chemicals with chemical end groups (functionality) for chemical reaction to both an inorganic particle surface (typically a particle, of nanometric (or micron) size, or a fibre) with one of the end groups and to

a polymer molecule with the other end. The importance of a coupling agent applied to the surface of a nanoparticle is that it sets the stage for the quality and properties of the interphase region involving the polymer matrix before the matrix resumes its normal properties. Different studies have explored the effect of the functionalization. Roy et al. have shown that an appropriate surface functionalization using different systems based on XLPE/SiO2 functionalized with aminopropyl-trimethoxysilane (AEAPS), hexamethyl-disilazane (HMDS) and triethoxyvinylsilane (TES) agents may increase the breakdown strength [48]. Figure 1-11 provides a comparison on the basis of Weibull statistics between the DC electric strength of a XLPE-SiO2 nanodielectric, its microcomposite counterpart and the base polymer from which it is formulated. Their results certainly appear to show that surface functionalization is capable of increasing the characteristic breakdown strength.
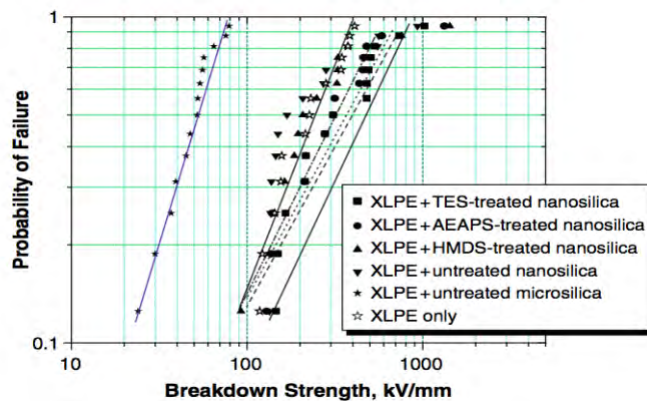
Figure 1-11. Weibull plots of the breakdown probability of XLPE together with a variety of composites

In addition, authors have studied the effect of temperature on the breakdown characteristic. Results were obtained for several temperatures started from 25°C to 80°C. Table 1-1 provides breakdown data as a function of temperature. As it can be seen, the enhancement in breakdown value is evident for treated nanosilica compared to untreated nanoparticles and unfilled XLPE. Moreover, the enhancement is more accentuated at high temperatures [48].

Table 1-1. Characteristic breakdown voltage (kV/mm) of XLPE and several nanocomposites at a range of temperatures (Weibull shape parameter in parenthesis).

Temperature Materials	25 °C	60 °C	70 °C	80 °C
XLPE	269 (2.49)	183 (2.65)	129 (3.66)	79 (3.84)
XLPE + Untreated Nanosilica	314 (2.07)	260 (2.27)	213 (2.49)	83 (3.09)
XLPE + AEAPS Treated Nanosilic	400 (1.69)	266 (2.20)	263 (1.79)	134 (2.11)
XLPE + HMDS Treated Nanosilic	336 (1.69)	225 (1.97)	208 (2.14)	128 (2.09)
XLPE + TES Treated Nanosilica	446 (1.73)	422 (2.22)	344 (2.17)	220 (2.87)

In similar perspectives, Roy et al have analyzed the dielectric behavior of unfilled XLPE in order to compare it with different systems based on XLPE/SiO2 micro and nano treated/untreated one [49][50]. From figure 1-12, the dielectric spectroscopy analyses provide considerable insight into the nature of the structure, which contribute to the polarization and loss. The results show that the untreated nanocomposites exhibit a relative permittivity lower than the unfilled polymer, which suggests the presence of an interfacial zone around the particles with smaller permittivity compared to the bulk polymer [49]. A marked loss factor dispersion was observed in the case of unfilled XLPE at the frequency of 1 Hz but was eliminated for the case of functionalized nanocomposites. With the respect of the loss tangent, it is very significant that a conduction region appears in the case of untreated nanoparticles, which suggests the presence of a conductive interface in their case. Low frequency dispersion can be observed in microcomposites which is absent in all nanocomposites [49].

In other hand, a recent paper has reported that nanoparticles surface treatment using a coupling agent reduces the presence of aggregates and affect considerably the rheological properties and dielectric performance, in particular a considerable improvement of the breakdown strength as well as a reduction of dielectric losses are observed [51]. Andritsch et al. have reported that a successful surface modification of nanoparticles leads to the formation of a rigid layer around each nanoparticle. The polymer chains rearrangement at the nanoparticles interface creates an immobilized layer forming the interphase [52].
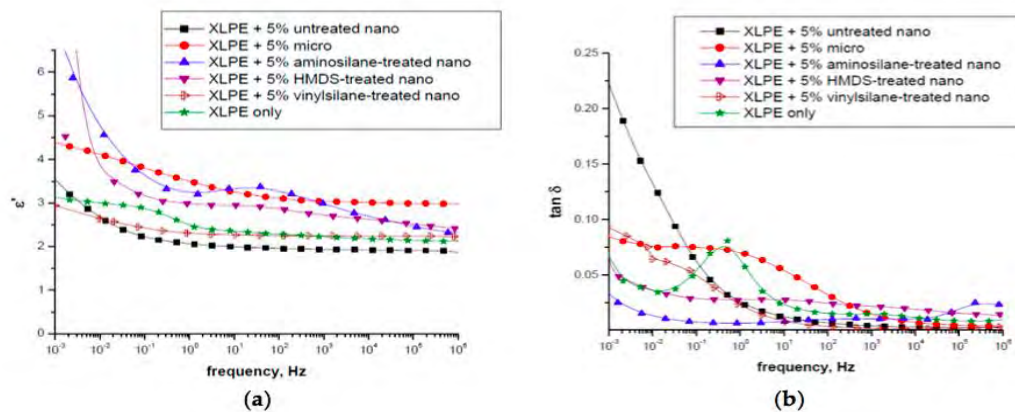
Figure 1-12. (a) Real part of relative permittivity and (b) loss tangent of functionalized XLPE at 23 °C.

1.4.2. Functionalization effect

Nanoparticles are generally agglomerated as a result of their high surface energy, therefore avoiding nanoparticles agglomeration before or during composites manufacturing proves to be a key issue in obtaining a good filler dispersion and to bring the nanoparticles into full play [53]. Additionally, switching the surface feature of nanoparticles from hydrophilic to increase the

filler/polymer matrix compatibility is also critical. The modification of the filler surface by coupling agents improves their dispersibility in organic matrices. Based on literature, different types of silane coupling agents are used for the chemical treatment of particle surfaces. Vinyltriethoxysilane, vinyltrimethoxy silane, 3-glcidoxypropyltrimethoxy silane ("Glymo") and 3-aminopropyl triethoxysilane ("APTES") are some of the most commonly used coupling agents in the nanocomposites field.

Figure 1-13(a) shows how silane coupling agents can react with hydroxyl groups present in the inorganic particle surface via condensation reaction [53][54]. Indeed, hydroxyl groups attack and displace the alkoxy groups on the silane (hydrogen bond), thus forming a covalent -Si-O-Si- bond (chemical bond). Figure 1-13(b) shows the principle applied to a polyolefin–silica nanocomposite where the silica nanoparticles have been treated with triethoxyvinylsilane [50].

(a)   (b)
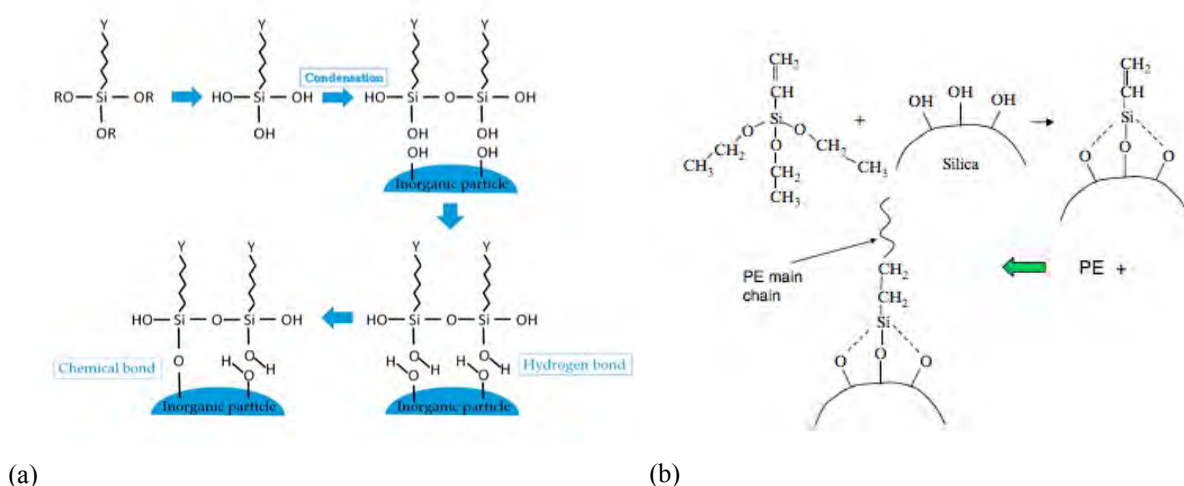
Figure 1-13. (a)Schematic representation of inorganic particles surface functionalization via silane condensation reaction (b) The use of a vinylsilane functionalizing agent with a polyolefin-silica nanocomposite

One can notice that the most effective way to engineer the interphase region is to chemically adjust the nanoparticles surface so as to modify the bonding with the matrix and/or generate chemical species that can play a role in the charge storage and transport in the nanocomposite. In this context, it has recently been shown using Electron Paramagnetic Resonance (EPR) techniques that the application of such methods can generate surface states that provide trap sites which, in turn, can modify several of electrical characteristics [55]. Moreover, the change in the nanoparticles surface polarity enables a better dispersion between the modified nanoparticles and polymer matrix [47].

Hereafter, a description of different interphase models set in order to describe this nanometric region in nanodielectrics is presented.

1.5. Interphase Models

As already stated, the surface area formed by nanoparticles (and consequently the interfacial surface area) is three orders of magnitude larger than that of the microparticles [5]. Moreover, with the addition of nanoparticles in a base polymer, the mobility and the structure of the surrounding polymer change considerably. The physico-chemical state of interphases has been first characterized by indirect spectroscopic techniques such as the Fourier-transform infrared spectroscopy, Raman spectroscopy and X-ray photoelectron spectroscopy, which lead to several interphase models [56]. Various theoretical models have been recently introduced to describe the role of the interphase and explain the effect of nanosized filler materials in polymers.

1.5.1. Lewis model: the intensity model

A classical description of interfacial zones has been explained with the intensity model of Lewis. This model (figure 1-14) considers an interface between two uniform material phases A and B. Each atom or molecule interacts at the interface with its environment according to different types of long- and short-range forces. Thus, the forces and consequently the intensity of a chosen material property, which can be any physical or chemical property in general, is constant within each of those phases and will become increasingly modified as the interface with the other phase is approached. The range over which the forces in question are different from the bulk values in each phase is defined as the interface AB where the intensity of a chosen property changes from the value in the bulk phase A to the value in the bulk phase B [57]. The thickness of the interfacial zone may be less than a nanometer when only low range forces exist, and reaches 10 nm and more regarding long range forces, as is the case with electrically charged surfaces [58][59]. In the case of a organic/inorganic fillers nanocomposite, the solid phase is made of nanoparticles and the amorphous polymer matrix is approximated to represent the mobile phase. In fact, the chains in a polymer can slightly move, in contrast to the ceramic filler structures.
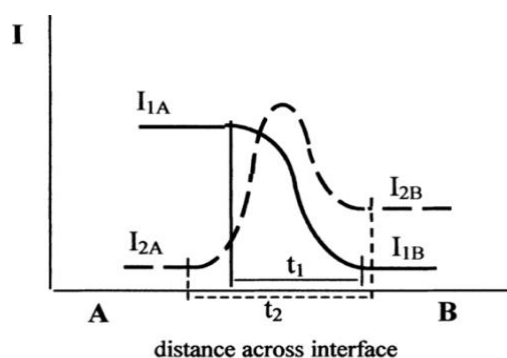

Figure 1-14. The interface between two phases A and B defined by the intensities I_1 and I_2 of properties 1 and 2 as they vary over effective distances t_1 and t_2 between A and B. t_1 and t_2 will be of nanometric dimension

Lewis model of electrical double layer (see figure 1-15) is encountered when a part or the whole surface of nanoparticles is electrically charged [58]. In response to this charge, the matrix creates a shielding layer against the surface charge. Lewis defines the two layers of this model as: (i) the first is named Stern layer of molecular thickness. It mainly contains oppositely charged ions regarding the particle surface (counter-ions) at high densities and of rigid binding with the surface through strong forces. The intensity of these forces makes the ions in this layer almost immobile in the normal direction to the charged surface. (ii) The second layer is named Gouy-Chapman layer, which is less dense than the first layer (diffuse layer). Gouy-Chapman layer is connected to the surface by Columbic forces. Stiffness and thickness of this layer are inversely proportional to the conductivity of the matrix [58].
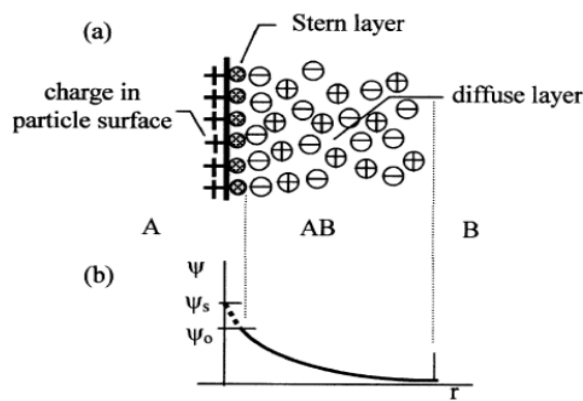
Figure 1-15. (a) The diffuse electrical double layer produced by a charged particle A in a matrix B containing mobile ions, and (b) the resulting electrical potential distribution $\Psi(r)$

The role of interfaces has been pointed out in [36], it is proposed that around the nanoparticles a Stern layer and a diffuse double layer (layer Gouy-Chapman) are formed, which have a high conductivity in opposition to the low conductivity of the surrounding material. Charge movement through these layers is relatively easy [14]. In this way, a current flow is possible between the nanoparticles. In another paper [43], it was noted that the significant interfacial polarization in conventional polymers is mitigated in nanocomposites, where a short-range highly immobilized layer develops near the surface of the nanoparticle. This layer affects a much larger region surrounding the nanoparticle in which conformational behavior and chain kinetics are greatly altered. It is that this interaction zone is important for the material property modifications, especially if the curvature of the nanoparticles approaches the chain conformation length of the polymer.

1.5.2. Tanaka model: the multi-core model

The multi-core model proposed by Tanaka *et al.* is presented in figure 1-16 as a three layers model, overlapped by a Gouy-Chapman diffuse layer [60]: (i) the first layer (Bonded layer) of nm order

thickness with hard core is the layer that firmly connects the inorganic nanoparticle to the matrix. This bonding is usually provided by coupling agents added to the surface such as silane. (ii) The second layer (Bounded layer) of about few nanometers thickness depends on the intensity of the present forces, with morphological regularity. This is the part of the interphase that consists of polymer chains in strong bonding and/or interaction with the first layer and the inorganic particle. (iii) The third layer (Loose layer) of several tens nm thickness with amorphous morphology is the layer that follows the first two layers and that reacts loosely with the bounded layer. Its corresponding polymer chains are generally considered to have different conformations, mobility and even free volume or crystallinity from the organic bulk. It can also consist of a less stochiometrically cross-linked layer.

Furthermore, Columbic forces superimpose the above chemical layers. When the particle is charged, an electrical double layer overlaps the three layers with far field effect as mentioned in the Lewis model. This model also states that polymer chains order diminishes with the transition from the first to the third layer. Hence, charge carriers traps can be deep in the first ordered layers, and superficial in the rest. Moreover, this model has been used to explain the previously mentioned decrease in the dielectric permittivity of nanofilled polymers. Authors explain that by the decrease of chains mobility in the second layer, and the decrease of free volume in the third. The interphase region is likely to encourage the forming of a conduction path. Meanwhile, the interphase behavior between the nano particles and the matrix polymer is more complex than originally thought [60].
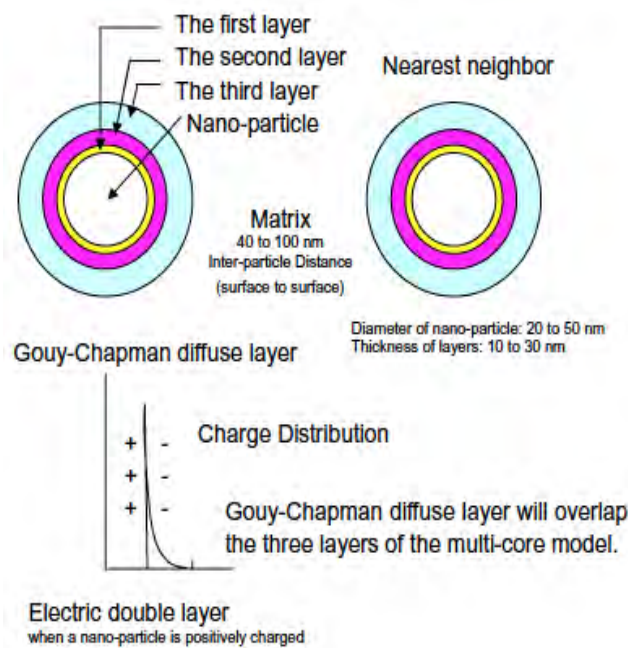

Figure 1-16. Multi-core model for nanoparticle / polymer interphase

1.5.3. Tsagaropoulos model

Tsagaropoulos model consists of two basic layers around the nanoparticle. The first contains the chains of the polymer that are strongly related to the particle, and the second is the least bonded layer [61]. A third layer of unaffected polymeric chains has been later added to the model [62]. The movement of polymers is restricted in the first layer and becomes suspicious in the second to become almost free in the third. The morphology of polymer chains was used in order to explain the two glass transition temperatures (T_g) sometimes measured in nanodielectrics [61]. Explaining Tsagaropoulos model in other words, one can note that the loosely bound polymer exhibits its own glass transition, whereas the tightly bound does not participate in the glass transition. At lower concentrations of nanoparticles, the interparticle distances are large and the mobility of the polymer next to the tightly bound layers is not influenced. Such regions cannot form a second glass transition, despite the fact that the temperature of the first glass transition decreases. By the nanoparticle concentration, the interparticle distances are reduced. When the loosely bound layers start to overlap (a critical interparticle distance is reached) they can exhibit their own glass transition. When the nanoparticle concentration increases further, the polymer regions with reduced mobility decrease but the immobilized regions increase. Consequently, the loosely bound layers are converted into tightly bound layers and thus, there is a reduction of the second glass transition temperature. The second (T_g) has been found to correspond to the more restricted polymer chains of the loose layer created by sufficiently close particles at appropriate filler content [61].

1.5.4. Interphase volume model

The interphase volume model by Raetzke *et al.* assumes that the interphase consists of polymer chains which have different morphology than the remaining uninfluenced matrix materials, due to the bindings and interactions between filler particle surface and polymer. The model aims at giving the dependency of the interphase volume fraction regarding filler weight percentage [45]. The model assumes that an interphase region surrounds the particles of any diameter, and which satisfies three suppositions:

1. particles are homogeneously dispersed in the matrix.
2. they are all spherical.
3. their disposition is similar to a face centered cubic lattice.

The interphase volume is shown in figure 1-17 for an effective particle diameter of 40 nm, respectively. It can be seen that for high interphase thicknesses of 20 nm and 30 nm, a distinct maximum of the interphase volume is formed in the material [45].
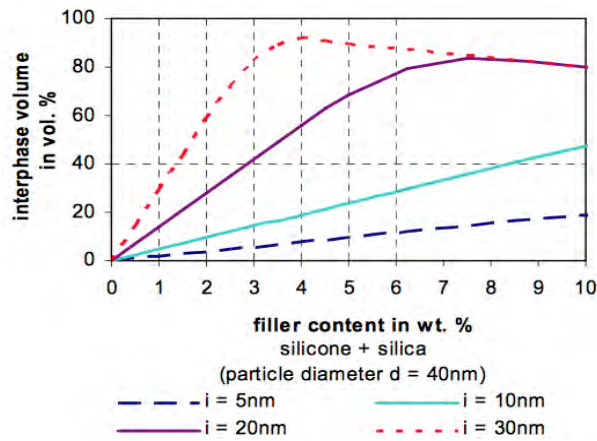
Figure 1-17. Interphase content according to the interphase volume model for a silicone matrix with SiO2 nanoparticles and interphase thicknesses i for a particle diameter d

Four cases of interphase neighboring particles are taken into consideration and shown in figure 1-18: not overlapped, overlapped, highly overlapped and absolutely overlapped. Each case mainly depends on the distance between particles center, which is dependent on the filler content, or the interphase thickness. As presented in figure 18-d, the interphase zone around the particles can overlap in the nanocomposites, thus may be expected to improve the dielectric properties.
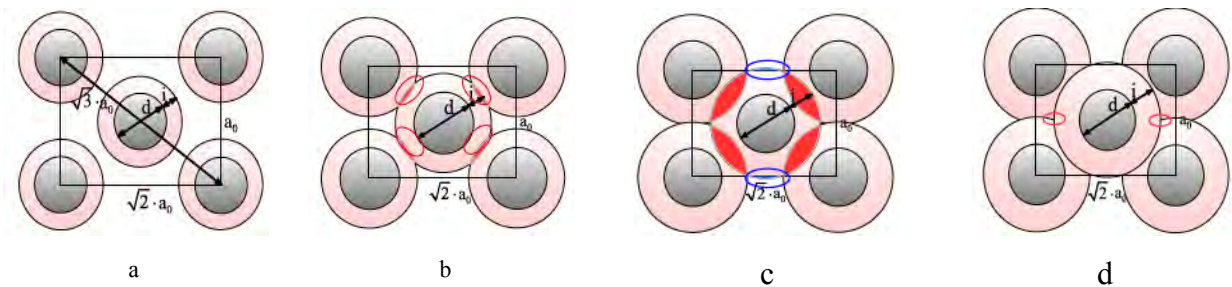

| a | b | c | d |

Figure 1-18. View on the body diagonal: a. interphases do not overlap; b. interphases of the nearest neighboring particles do overlap, c. interphases of the neighboring center particles do overlap, and d. triple points reached: the whole material is only consisting

1.5.5. Polymer chain alignment model

The polymer chain alignment model presented in figure 1-19, is especially influenced by the Tanaka model and the interphase volume model. It assumes that the polymer structure of the host material of a nanocomposite changes as a function of the distance to a surface modified nanoparticle. When a coupling agent is used to connect organic chains to the inorganic surface, this connection can result in a restricting of the surrounding host matrix. A layer of perpendicularly aligned polymer chains is then formed around the particle surface that is treated by a curing agent. This layer forms a rigid polymer structure [52]. The alignment is also extended beyond this layer since polymers often consist of long chains. Furthermore, an interpenetrating polymer network

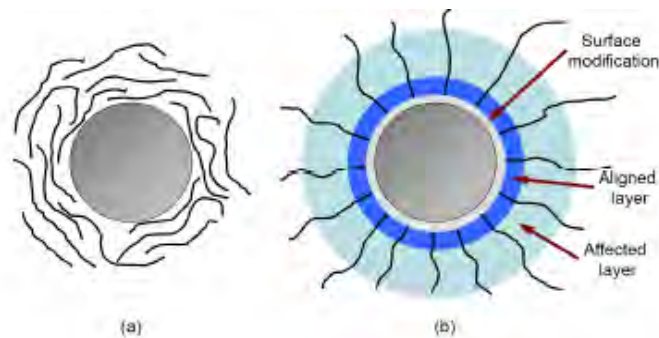can be formed between polymer chains leading to physical properties unlike those of particle or host [52].

Figure 1-19.(a) Particle without surface modification and thus only weak interaction with the host; (b) Particle with layer of surface modification, resulting layer of aligned polymer chains, further affecting the surrounding area and thus restructuring the polymer

1.5.6. Other interphase models

The water shell model, proposed by Zou *et al.* in 2008 [63], is based on Lewis and Tanaka models in order to explain the nanodielectric materials behavior in the presence of humidity. Based on characterization results of an epoxy nanocomposite system, authors assume that three types of water shells surround the nanoparticle, which itself plays the role of a "core". In this model it is considered that the water molecules are concentrated around the nanoparticles and, in low concentrations, in the polymer matrix. If the water concentration around the nanoparticles is high, percolative paths are formed through overlapping water shells, which affect the dielectric properties of epoxy nanocomposites [63][64]. More recently, T. Tanaka presented a new model for nanodielectrics explaining several of their electrical behaviors [65]. In this model, nanoparticles are represented as quantum dots. Since quantum dots possess negative dielectric permittivity, the author notes that this can simply explain the commonly observed permittivity decrease in nanocomposites.

Polymer nanocomposites models presented above give an idea about the physico-chemical and electrical properties of the interphase between nanoparticles and polymer matrix. Parts of the experimental results were explained through these models, but with some limitation since the interphase regions have not been made visible until now in polymer nanocomposites.

1.6. Overview on interphase characterization

1.6.1. Introduction

As seen previously, different models were proposed to describe the interphase morphology and structure. In addition, some authors have proposed to extract interphase properties from macroscopic experimental characterization methods as summarized in table 1-2.

However, this overview emphasizes that the interphase exhibits a lower dielectric permittivity than matrix and its dimension presents a strong dispersion with values higher than 10-20 nm as proposed by Tanaka [60]. It can also be noticed that only one interphase property is given from each experimental technique and there is no quantitative value for the interphase dielectric property. Moreover, both theoretical models and experimental results on the interphase properties are based on unreal hypotheses (monodispersed nanofillers, spherical nanoparticles, equidistant fillers…). Consequently, as reported by Pourrahimi et al., the interphase needs to be characterized at the nanoscale [66]. Probing locally the interphase is nowadays mainly addressed by two imaging and characterization methods of high resolution: electron microscopies and scanning probe microscopies.

Table 1-2. Interphase properties in terms of width or thickness Wi and dielectric permittivity εi compared to matrix one εm for different nanodielectrics investigated in the literature.

Matrix	NPs	Techniques	Interphase properties
Epoxy	40nm Al_2O_3	Dielectric spectroscopy	W_i=200nm [67]
	Al_2O_3	DMTA	W_i=30-65nm [68]
LDPE	65nm Al_2O_3	Dielectric spectroscopy	W_i=5-20nm $\varepsilon_i < \varepsilon_m$ [69]
	100nm Al_2O_3		W_i=30-40nm $\varepsilon_i < \varepsilon_m$ [70]
Silicon rubber	10nm SiO_2	Dielectric spectroscopy	W_i=14-19nm $\varepsilon_i < \varepsilon_m$ [71]

1.6.2. Electron and ion microscopies

Electron microscopies can be divided into four main types: Transmission Electron Microscopy (TEM), Scanning Electron Microscopy (SEM), Scanning Transmission Electron Microscopy (STEM), Focused Ion Beam (FIB) and Dual Beam microscopy. Briefly, in a SEM the signal is obtained from the surface of the sample that has been bombarded with the beam, in contrary to the TEM where the transmitted signal is detected from the opposite surface of the beam direction. The FIB is similar to SEM except that a beam of ions replaces electrons and provides higher resolution

imaging. Several informations can be derived out of the signal depending on the type of electron beam-sample interaction, among which, density contrasts, cristallinity, chemical elemental composition etc.

TEM has been widely used to study the interphase of coated ceramic fibers in a ceramic matrix[72], the interphase in carbon reinforced composites [73][74] and ceramic fiber reinforced polymers [75]. A gradient variation in the structure at the interfacial region has been reported in ref [73]. Later, authors from [74] studied the effect of three types of sample preparation on the accuracy of interphase study with TEM: Focused Ion Beam (FIB), Ion Beam etching (IB) and Ultramicrotomy (UM). Ion beam prepared cross-sections showed that the interphase is a transition region from crystalline states to amorphous ones. However, electron microscopies present some limits which are due to the easily deflected or stopped electron beam in the matter. This explains the necessity to work under low pressure and the requirement of very thin samples especially for TEM measurements (< few hundreds of nanometers). Moreover, when used to study electrical insulations, electron microscopies resolution is reduced and image artifacts can appear due to charging effects [76][77][78][79][80].

1.6.3. Nano-indentation and Nano-scratch

As interphases affect the global physical properties of composites, their macroscopic mechanical behavior has also been shown to be correlated to the quality of the interface between the filler and the matrix [81]. In the following, a brief description of nano-indentation, nano-scratch methods and their corresponding state of the art for interphase study will be addressed. The nano-indentation method uses an indenter that is pressed into the material while recording loading-hold-unloading cycles in function of the displacement [82]. Calibrating the indenter geometry and assuming a linear elastic behavior on the onset of loading, the hardness and quasi-static elastic modulus can be derived [83]. On the other hand, nano-scratch tests also use a characteristic tip of calibrated geometry but placed in contact with the sample. The latter is moved below the tip creating linear scratches. Nano-indentation and nano-scratching methods have been used to study interfaces in several types of composites, among which, glass-reinforced polymers [82][84][85][86] and single-wall-carbon-nanotubes [87]. Similarly, to SEM, these types of composites have been investigated in cross-sectioned specimen. Authors have been able to show the diffusion into the interphase of water molecules due to water ageing [86], and the dissolution of silane coupling agents in the interphase [82]. The interphase widens with water ageing and silane coupling agent concentration. Interfacial regions in fiber-reinforced composites frequently show a gradual change in hardness and stiffness between matrix and filler [87]. The reported

interphase thickness values are very different, varying from 0.1 - 1.5 μm for example [85][88][89], to 2 - 6 μm [84][86]. The measured width depends on the type of material components, as well as the specific measured property with the corresponding adopted experiment.

Although these techniques have shown to be useful for interphase study, they are however limited in resolution. They might be applicable to microfilled composites, possible to be cross-sectioned, but they quickly reach limitations for nanofilled polymers. In this context, scanning probe microscopy has been used as a novel alternative method. All of these techniques probe different interphase properties in order to differentiate it from initial material components. A brief description of these techniques and their recent advances in interphase study of variously filled composites will be developed in the following paragraphs.

1.6.4. Nanomechanical atomic force microscopy

As a novel approach for nanomechanical characterization, atomic force microscopy (AFM), adapted to mechanical testing, has emerged to study composite materials that present extremely narrow interphase regions and/or nanometric fillers, difficult to be distinguished in casual mechanical techniques. The Atomic Force Microscope (AFM) uses a physical probe in the form of a micrometric cantilever with a very sharp tip at its end. The probe senses interaction forces with the sample while placed either in contact (contact mode) or at few nanometers from the surface (non-contact or tapping mode). AFM nanomechanical mappings are of particular interest for the study of heterogeneous materials, as they open the access to the nanoscale structure and local mechanical properties. Several operational methods can be adopted in order to investigate numerous material properties according to the physical nature of the tip-sample interaction and to the mechanism of signal extraction. High lateral resolutions (atomic scale) and sensitivities (< 10 pN) can be achieved with AFM on almost all kinds of surfaces with minimal treatment in many environments, contrarily to SEM. The high resolution mainly relies on the precise and accurate motions provided by piezoelectric devices. A detailed description of AFM will be presented in chapter II.

Since the first profiles across fiber-matrix interfaces using AFM nanoindentation by M der and Gao [90], the mapping of the local modulus and of additional properties such as tip-sample adhesion force and energy dissipation allowed a more complete and more accurate understanding of the role of interfaces and interphases in composite materials. A growing number of AFM nanomechanical studies, leading to a better understanding of both parts: on one hand, the relation between structure and properties of composites, and on the other hand, how AFM should be used for an optimal accuracy and how nanomechanical properties can be interpreted.

In the case of micro and nanocomposites, AFM also gives important information on the dispersion and nature of particles and phases, which can weight their contribution to the overall mechanical behavior [91]. The potential of AFM nanomechanical measurements in the understanding of composites is currently helping the growth of the biocomposites field. Cellulose based composites have been widely studied by AFM, particularly with Peak Force Quantitative Nanomechanical (PF-QNM) mode [92][93]. Khelifa and collaborators [94] have studied the evaluation of the structuration and mechanical properties of thin films such as acrylic/cellulose nanowhiskers (CNWs) composite films. The authors reported a modulus increase of the film by almost two orders of magnitude when adding 50%wt of CNWs to the acrylic matrix, reaching 11 GPa, which is higher than a pure CNWs film (i.e. 9 GPa). They could verify, also by AFM, that it is due to a specific organization of CNWs when blended with the matrix. Furthermore, Cranston et al. have measured the Young modulus of nano brillated cellulose/polyethyleneimine (PEI) multilayer thin films using strain-induced elastic buckling method. A value of 1.5 GPa was obtained for the film [95]. In other hand, from the Young modulus of this material in a bulk state (i.e. 5.5 GPa), the DMT moduli of different components of the blend measured by PeakForce QNM (i.e. 0.85 GPa for cellulose, 0.3 GPa for PEI and an average of 0.8 GPa), show more similar mechanical behavior between the film and the nanoscale components than that of the bulk materials. They deduced that the mechanical behavior sometimes is better predicted by nanoscale measurements such as PeakForce QNM AFM mode. Moreover, authors from [96] have shown that cellulose nanofibers can increase the crystallinity acting as nucleating agents in polyamide 11 (PA11) nanocomposites, exhibiting a higher structural order than for neat PA11 (figure 1-20) [97]. This result shows that AFM nanomechanical mappings could be particularly efficient at highlighting the crystalline structuration in semi crystalline polymer. Generally, crystalline zones are evidenced by an increased local modulus.

Panaitescu et al. have pointed out a local modulus drop in the matrix around fillers underlining a poor interface in polyethylene/nanosilica composites [98]. The use of relatively small quantities of polyethylene grafted with maleic anhydride (PE-MA) resolved the modulus drop, thus improving the interfacial interaction leading to better overall macroscopical mechanical properties. The authors have, with PeakForce QNM mappings, also pointed out the different crystallization behaviors of the polyethylene, depending on the composition of the composite: the size of the spherolites in neat PE decreased with PE-MA (see figure 1-21 a and b), while the viscosity induced by the nanosilica particles hindered their formation, leading to a lamellar structure (Figure 1-21 c and d) [98].
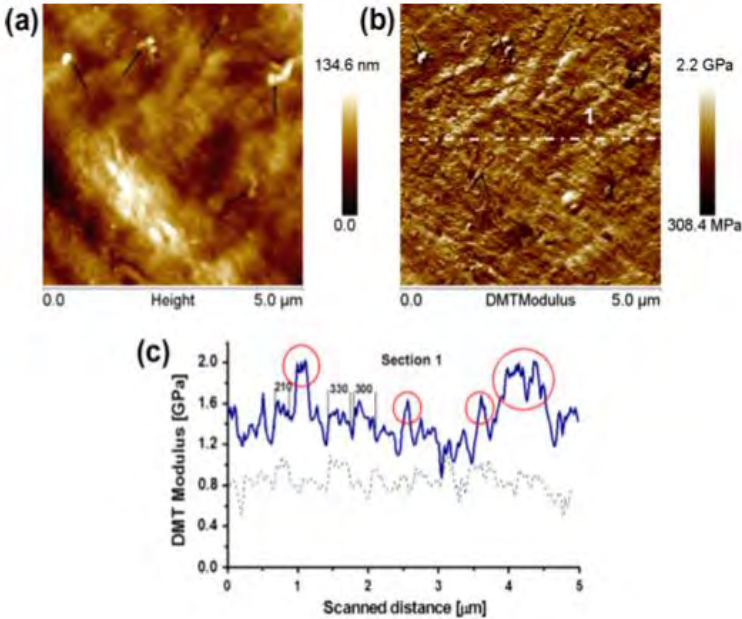
Figure 1-20. (a) AFM topographical and (b) DMT modulus images of a PA11/cellulose nano fibers composite. (c) modulus profile taken across the white dashed line in (b), represented by the blue solid line. The red circles indicate modulus peaks, hinting the presence of cellulose nano bers close to the surface. The gray dashed line represents an equivalent DMT modulus profile acquired on neat PA11
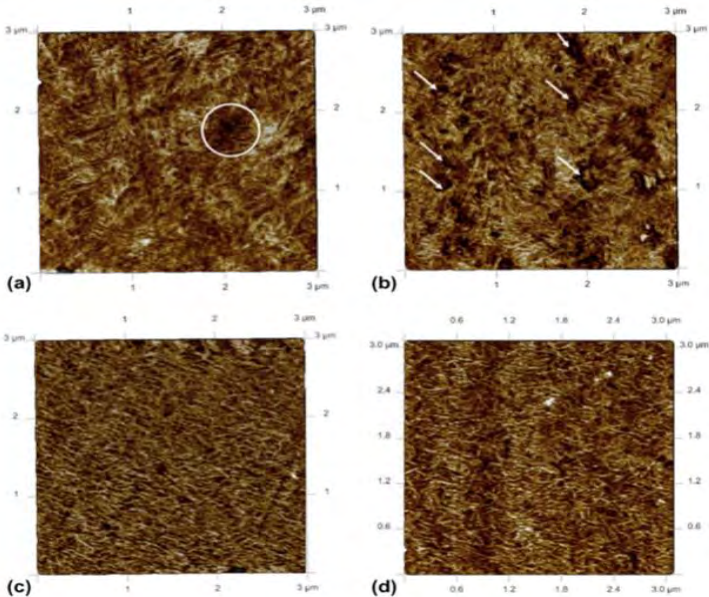

Figure 1-21. AFM 3 × 3 μm^2 DMT modulus images of (a) neat PE; (b) PE-MA; (c) PE with nanosilica (5wt%); (d) PE with PE-MA (5wt%) and nanosilica (5wt%). Circles and arrows mark low-modulus zones. The modulus scale is not given, but moduli are typically in the 200-300 MPa range

More recently, nanomechanical property mapping of poly(butylene-adipate-co-terephthalate)/poly(lactic acid) PBAT/PLA blends compatibilized with ionic liquids was performed by Megevand et al [99], exploring the differences induced by the nature of the counter

anion for a given phosphonium-chloride ionic liquid IL (il-Cl) and phosphonium-phosphinate IL (il-TMP). The AFM PF-QNM mode was used. From figure 1-22, quantitative DMT modulus mappings highlighted a decrease in the nanoscale DMT modulus of both phases with the addition of ionic liquids, especially with il-Cl. Consequently, the Young modulus (which is measured at the macroscale) increase could be explained by more favorable interfacial interactions between PBAT and PLA mediated by the ionic liquid. DMT modulus and adhesion data analysis confirmed these assumptions. il-Cl led to a two times thicker interphase inducing a better local miscibility of PBAT and PLA phases, explaining the improvement of the macroscopic mechanical properties such as the strain at break. il- TMP induced a slighter effect on the local miscibility but formed an interface layer ensuring interactions with both polymers. In addition to the basic understanding of the morphology of these specific polymer blends, the authors confirm that ionic liquids can offer new routes for polymer blends compatibilization [99].
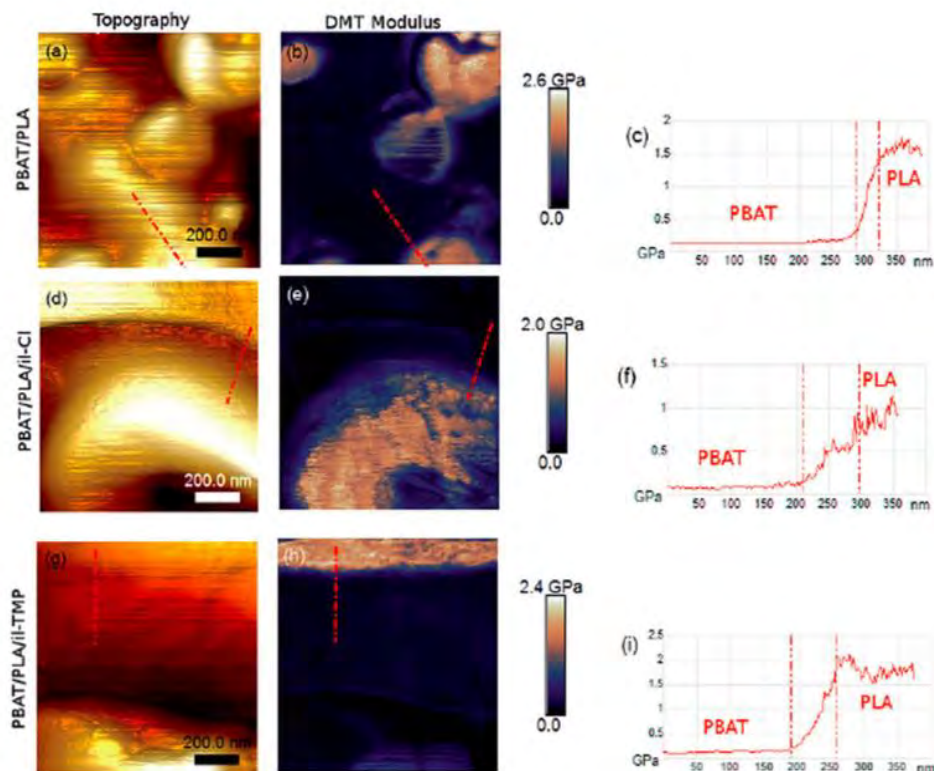

Figure 1-22.AFM 1 μm^2 topography (left) and DMT modulus (center) images with corresponding modulus profiles for PBAT/PLA (a–c); PBAT/PLA/ il-Cl (d–f); and PBAT/PLA/il-TMP (g–i). The modulus profiles are taken following the red dashed line in (b), (e) and (h) .

The gradient of properties, as mentioned for polymer blends [99][100][101], is also a relevant parameter in the study of composites interphases. A thick modulus gradient from one phase to another (i.e. a filler) is generally interpreted as a cohesive interphase [102]. Pakzad et al. showed that the gradient of properties (i.e. DMT modulus and adhesion) at an interface also depends on the size of the filler in the case of poly (vinyl alcohol) (PVA)/poly (acrylic acid) (PAA)/cellulose

nanocrystals (CNC) composites [103]. Nanomechanical properties of the interphase (the zone between CNC surface and polymer matrix) were quantitatively characterized using peak force tapping mode in AFM. As opposed to topography images, nanomechanical and adhesion maps enabled the detection of CNCs embedded in the PVA–PAA polymer matrix. The interphase in the composites containing PAA exhibited a higher gradient in adhesive and mechanical properties in comparison to samples with no PAA (figure 1-23). From the polymer matrix to the CNC surface, the average elastic modulus increased from 9.9 to 12.8 GPa, and the adhesion to the AFM tip decreased from 36 to 25.6 nN, respectively. The observation of higher gradient in properties of the composites with PAA was related to the increase in the density of ester linkages from the polymer matrix to the CNC interface. It was also shown that the interphase thickness depended on the CNC size. Because larger CNCs have higher surface area, the influence of CNC penetrating deeper in the polymer results in higher interphase thickness [103].
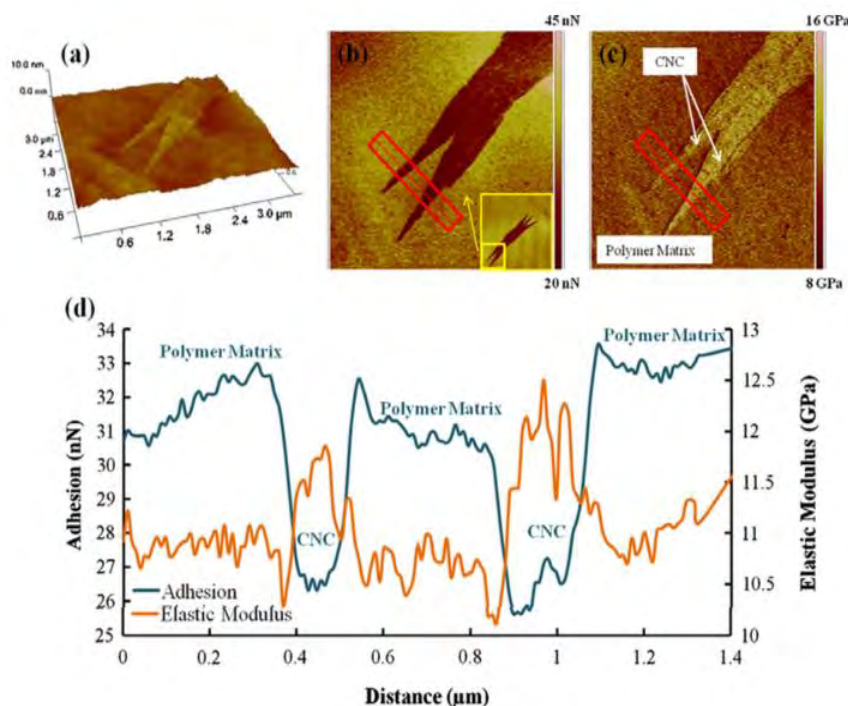

Figure 1-23. (a) 3D height, (b) adhesion, and (c) elastic modulus maps (3.5 μm²). Inset in (b) shows the scanning area (PVA 80–CNC 10–PAA 10). (d) The average adhesion and elastic modulus profiles of the area in the red boxes in (b) and (c). Polymer matrix and CNC regions are marked on the profile. Interphase region is the distance that adhesion and modulus profiles are overlapped

Moreover, M. Mousa et al. used PeakForce Tapping-Quantitative Nanomechanical Mapping in order to demonstrate for the first time direct three-dimensional topography and physical measurement of nanophase mechanical properties between nanodiameter bamboo charcoals (NBCs) and poly (vinyl alcohol) (PVA) in polymer nanocomposites. Here, the interphase dimensions can be determined according to AFM height and adhesion images of PVA/NBC composite samples. As evidently seen in figure 1-24 (a) and (b), the height of NBCs is much

greater than that of PVA with a linearly increasing tendency from interphase regions near PVA matrices to those close to NBCs. NBCs can be easily distinguished from PVA matrices owing to their different adhesion properties. It is clearly shown that the tip adhesion to PVA matrices of nanocomposite sample is 10.76 ± 3.42 nN, which is much greater than 2.1 ± 0.87 nN for NBCs. Accordingly, interphase thickness is represented by the scan distances of 16 and 13 nm with a sharp decreasing adhesion gradient from PVA matrices to NBCs on both sides of selected material regions, as illustrated in figure 1-24 (c) and (d) [104].
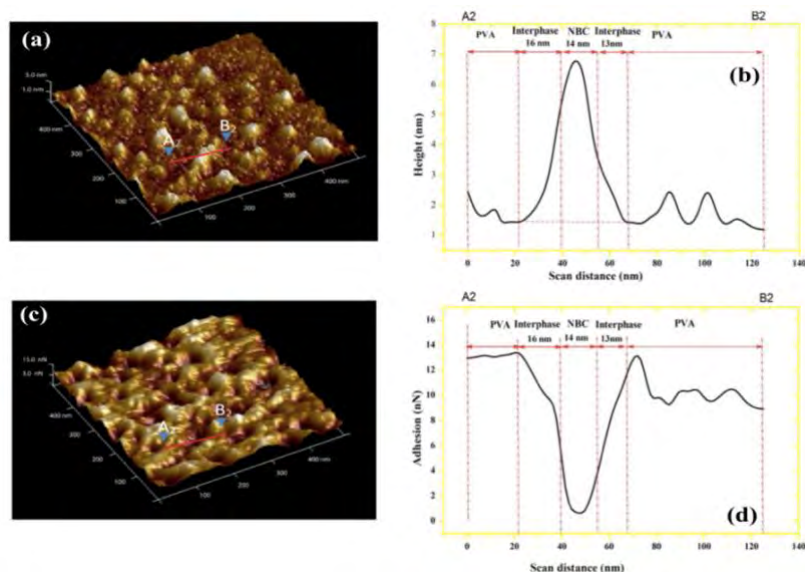
Figure 1-24. (a) 3D AFM height mapping image of PVA/3 wt% NBC nanocomposites, (b) height profile of corresponding nanocomposites taken along the line A_2B_2, (c) 3D AFM adhesion mapping image of PVA/3 wt% NBC nanocomposites, and (d) adhesion profile of corresponding nanocomposites taken along the line A_2B_2

The properties mappings have been extensively used to visualize the sub-micrometer structure of many kinds of materials, from cells and proteines to nanocomposites. The use of elasticity, adhesion, dissipation and/or deformation as contrasting informations in AFM images helps to understand how such materials are organized. Nevertheless, beyond simple contrasting, the data measured by AFM nanomechanical mappings are quantitative and reproducible if an appropriate calibration is performed, opening a novel way to study relations between structure and properties. From the above AFM PFQNM overview, it can be noticed that the measured thickness range of the interphase, performed on nanocomposites, varies considerably between different studies. This can be attributed at the first sight to the different composites compositions and thereby, physico-chemical interfacial interactions. However, this is also highly related to the scanned property, and most importantly, to possible scanning artifacts.

Additionally, authors suppose certain assumptions on the subsurface composition of the probed region, on which they have based their interpretations of the interphase.

1.6.5. Electrostatic force microscopy

As previously seen, the interphase thickness was probed using mechanical properties modifications in tapping [105][106] (phase images) or in Peak Force Quantitative Nanomechanical (PF-QNM) modes [103]. In addition, electrical characterization techniques, based on scanning probe microscopies (SPM), have been developed giving access to local electrical properties. For example, the interphase permittivity could be probed at local scale using Electrostatic Force Microscopy (EFM) [107][108].

D. El Khoury et al [109] have demonstrated the accurate detection of interphases in nanocomposites using three EFM-based experimental protocols employing reference samples. Samples were prepared to electrostatically model a nanodielectric material with an interphase (particle + interphase + matrix). They were based on spherical polystyrene (PS) particles deposited on a metallic substrate. Al2O3, SiO2 and PVAc were used to cover the particles and to mimic either the interphase layer or the matrix layer. In these samples, three types of dielectric materials, each with a specific dielectric permittivity, were assembled in the form of sub-micrometer particles covered by two thin shells that represent the interphase and the matrix in the "real" systems. The quantification of the dielectric permittivity of the used materials, within all types of association, was possible by comparing experimental data and numerical simulations. The authors also discussed the possibility of using the developed approaches to distinguish the composition and dielectric properties of "unknown" interphases in "real" nanocomposites with 3D inclusions, as well as in other types of heterogeneous nanometric materials, with reduced ambiguity about the real origin of the measured signals.

Another interesting paper, published at the end of 2016, used EFM to show the presence of the interphase in low density polyethylene nanocomposite with titanium dioxide nanoparticles of 50 nm radius [110]. Authors have studied thin sectioned parts of the bulk composite. Through the extraction of the *2ω*-phase shift EFM component, three areas of different composition have been distinguished: the matrix alone, a particle exposed at the surface of the sample and a matrix bump due to the nanoparticle underneath the surface. In order to investigate the physics of an EFM measurement, simulations over each specific type of complex material must be addressed. After the interpretation of phase shift values at these regions, and through the corroboration with numerical simulations, authors have declared the presence of an interphase around the nanoparticles (figure 1-25). The signal at the bump position could not be explained through simulations unless an interfacial layer of lower permittivity than the bulk polymer is present. Typical dielectric permittivity and thickness of the interphase have been found to be 1.6 and 20 nm respectively [110].

These results demonstrate that EFM is a powerful tool to probe interphase dielectric properties but some assumption about interphase thickness are needed to determine interphase dielectric permittivity[109] which is less than matrix one[110]. The existence of a charge layer in the interphase area was also demonstrated using EFM [111]. Based on the method introduced in [111] to measure model free surface charges, Deshler et al. have studied the existence of surface charges on particles in a nanocomposite and presented an hypothesis of the presence of an electric double layer around the particles, at the interfacial region [112].
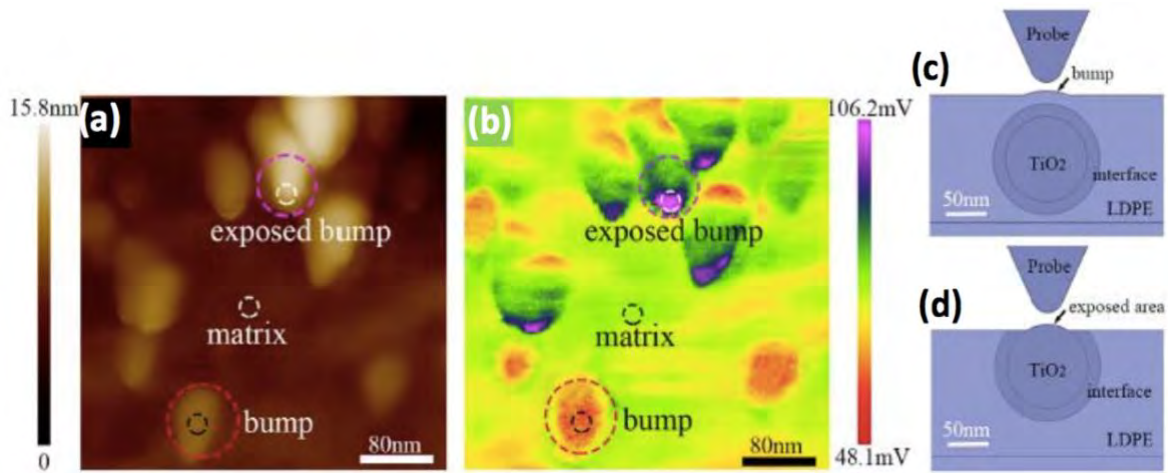
Figure 1-25. a. topography image, and b. $|\Delta\phi c\ (2\omega)|$ signals amplified by the LIA. c. and d. present the local finite models corresponding to two cases with interface: "bump" and "exposed bump"

1.7. Conclusion

In this first chapter, a special interest was given to nanodielectrics, a combination of nanoparticles in a polymeric matrix, because of their mechanical, thermal and insulating properties improvement, contrarily to their microcomposite counterparts. The explanation behind the special properties in nanodielectrics is usually attributed to the interfacial zone between filler and matrix called the interphase. As interactions zone can lead to regions with unique properties compared to both nanoparticles and polymer and due to their high volume percentage at the nanoscale, the interphase intrinsic properties are of the utmost importance.

Several physico-chemical interphase models have been established to understand the final nanocomposite experimental results. (i) A multi-core model proposed by Tanaka et al. has presented the interphase as a three layers zone. In addition, an electric double layer is superimposed on the three cores with far field effect as mentioned in the Lewis model. The interface region is likely to encourage the forming of a conduction path. Meanwhile, the interface zone around the particles can overlap in the nanocomposites, these overlapped interface zone is

expected to improve the dielectric properties. The exact reason causing this properies amelioration is not yet known. But, as a working hypothesis explained in the interphase volume model given by Raetzke and al. it is assumed that the interphase consists of polymer chains which have different morphology than the remaining uninfluenced matrix materials, due to the bindings and interactions between filler particle surface and polymer. Water molecules have been also reported to adsorb and accumulate in the interfacial region, clarifying the macroscopic increased permittivity.

Furthermore, interphases are critical in the understanding of the structure/properties relationships in nanocomposites. Consequently, a local characterization of the interphase becomes essential. Mostly used methods to study the interphase at the nanometric level are electron microscopies and nanomechanical characterization techniques, such as classical nano-indentation and nano-scratch methods. However, these techniques present some limitations, such as sample preparation complexity for TEM measurements in addition to imaging artifacts. Thus, interphases in nanocomposite materials have been particularly investigated with AFM techniques. First, AFM nanomechanical mappings offer an optimal way to evaluate the underlying mechanisms occuring at a local scale in nanocomposites. The measurement of local properties implies the in-situ scanning of interphases, which are not easily accessible by traditional characterization methods, but are critical in the understanding of the overall mechanical behavior of polymer blends and nanocomposites. In addition, due to the electrical application of nanodielectrics, we have been interested in the dielectric polarization properties of these materials. Since the permittivity of the interphase is supposed to be different than mixing components, this characteristic is thereby going to be another property of interest for interphase characterization. Consequently, the electrostatic force microscope will be utilized as a potential technique for both local and dielectric characterization method with the aim of interaction zones detection.

Finally, the measured interphase thickness importantly varies in literature. This is mainly due to the nature of composite components, measuring technique and most importantly, results interpretation. Thus, the necessity of both local nanomechanical and dielectric characterization is needed. Moreover, interphase was never characterized in term of morphology, mechanical and electrical properties in the same time to be compared with model as Tanaka's one. In this context, the main objective of this thesis is to characterize mechanical (Young modulus) and electrical (dielectric permittivity) properties of interphase using PF-QNM and EFM measurements in order to correlate them with nanocomposite macroscopic properties (dielectrics properties).

In the following chapter, sample preparation, macroscopic measurement technique and an introduction to PFQNM and EFM basic principles will be presented.

2. Materials, sample processing and experimental description

Content

2.1. Introduction

In the electrical insulation filed, polyimide (PI) has shown great electrical properties. Even if PI presents a good thermal stability (up to 300°C in the long term), its mechanical and electrical properties may deteriorate at these temperatures, in particular its dielectric properties, electrical conductivity and failure field. However, new requirement for thermostable insulating materials operating in applications with high temperatures is needed. An innovative way to enhance physical properties at high temperatures could come from the introduction of inorganic nanoparticles into the PI matrix. Indeed, in the analysis of the state of the art, this approach seems promising at least according to the theory of the "nano effect" presented in Chapter 1.

In this chapter, polyimide matrix and silicon nitride nanoparticles are introduced. Nanoparticles functionalization is then presented in order to optimize the dispersion of nanoparticles in the polyimide matrix. This better dispersion affects the interphase zone and plays also a major role in the nanocomposite properties improvement. In the following, polyimide/silicon nitride nanocomposite (PI/Si_3N_4) manufacturing steps are presented in addition to test structures and experimental techniques used during this thesis. A morphological characterization is first performed by transmission electron microscopy (TEM) in order to visualize the quality of the nanoparticles dispersion in nanocomposite films. Moreover, the atomic force microscopy (AFM) is employed to investigate nanocomposite surface morphology, to obtain roughness parameters and to map the quantitative differences of surface properties in order to investigate the interphase area. AFM is used to make at the same time qualitative and quantitative measurements of these interaction zones within PI/Si_3N_4 nanocomposite. The Peak Force Quantitative Nano Mechanical (PF QNM) AFM mode reveals the presence of the interphase by measuring mechanical properties (Young modulus, deformation and adhesion). Electrostatic force microscope (EFM) is used in order to detect and characterize matrix and interphases local permittivity. Furthermore, macroscopic properties of PI/Si_3N_4 films were studied through dielectric spectroscopy and breakdown strength measurements for different temperatures.

2.2. Materials

2.2.1. Polyimide

Polyimides (PIs) are advanced polymeric materials well-known for their excellent thermal, electrical, mechanical and chemical properties [113]. PIs are particularly attractive in the microelectronics industry due to their high thermal stability (Td), high glass transition temperature (Tg), low dielectric constant, high resistivity, high breakdown field, inertness to solvent, radiation

resistance, easy processability…etc. [114][115]. Moreover, one should note that PIs used as electrical insulators in microelectronics and electrotechnics are interesting because the constraints related to their implementation process are generally simple compared to those of inorganic materials. Indeed, their precursors are generally commercially available in the form of a resin that can easily be deposited in thin layers by spin coating, doctor blade coating or enameling techniques. In addition, PIs can be deposited in multilayers to increase the final deposition thickness. Thus, it is possible to deposit from a few micrometers to about twenty µm thick.

In 1965, Endrey and Sroog were the first to synthesize polyimides [113][116][117][118] from polyamide salts. In the described method, the synthesis is carried out in two steps. The first consists in preparing a polyamic acid (PAA) solution that is the precursor of the polyimide. PAA is synthesized by reacting two precursor monomers, a dianhydride and a diamine, at room temperature and in polar aprotic solvents such as N-methyl-2-pyrrolidone (NMP), N,N-dimethylformamide (DMF) or N,N-dimethylacetamide (DMAc). Many varieties of PAA can be synthesized leading to hundreds of different aromatic polyimides as presented in table 2-1.

Table 2-1. Thermal, electrical and mechanical properties of the main aromatic PIs

	T_g (°C)	T_d (°C)	ε_r	E' (GPa)	TS (MPa)	Film stress on Si wafer (MPa)	CTE (ppm/°C)
PMDA-ODA	>380	586	3.4	3.0	170	29	30-40
PMDA-PDA	>450	610	3.0	12.2	296	-10 (compression)	2
BPDA-ODA	325	531	3.3	3.0	230	34	28
BPDA-PDA	>330	595	3.1	10.2	597	5	3-7
BTDA-ODA	280	554	3.0	3.0	150	40	40
BTDA-PDA	>370		2.98	7.1	248	30	35
ODPA-PDA	>370		3.0	8.1	263	42	35

T_g: glass transition temperature; T_d: degradation temperature defined at 10% wt. loss; ε_r: dielectric constant; E': Young's modulus; TS: tensile strength; CTE: coefficient of thermal expansion between 50 °C and 300 °C. Film stress is given for film below 20 µm of thickness.

The thermal conversion of PAA to polyimide is carried out in two steps. The first is to partially heat the PAA to evaporate the polar aprotic solvent in which precursor monomers are dissolved. The PAA is then gradually heated to a temperature between 250 and 400°C under inert atmosphere to avoid oxidation problems (it is generally maintained from 30 minutes to 1 hour). This last conversion step is called imidization (i.e. formation of imide heterocyclic rings) and produces the final insoluble and infusible polyimide through the evaporation of water molecules from the material. Figure 2-1 shows the synthesis steps of 3,3',4,4'-biphenyltetracarboxilic dianhydride

(BPDA) with p-phenylene diamine (PDA) in order to form BPDA-PDA. Note that this polyimide presents a higher thermal stability (Td= 595 °C) [1].
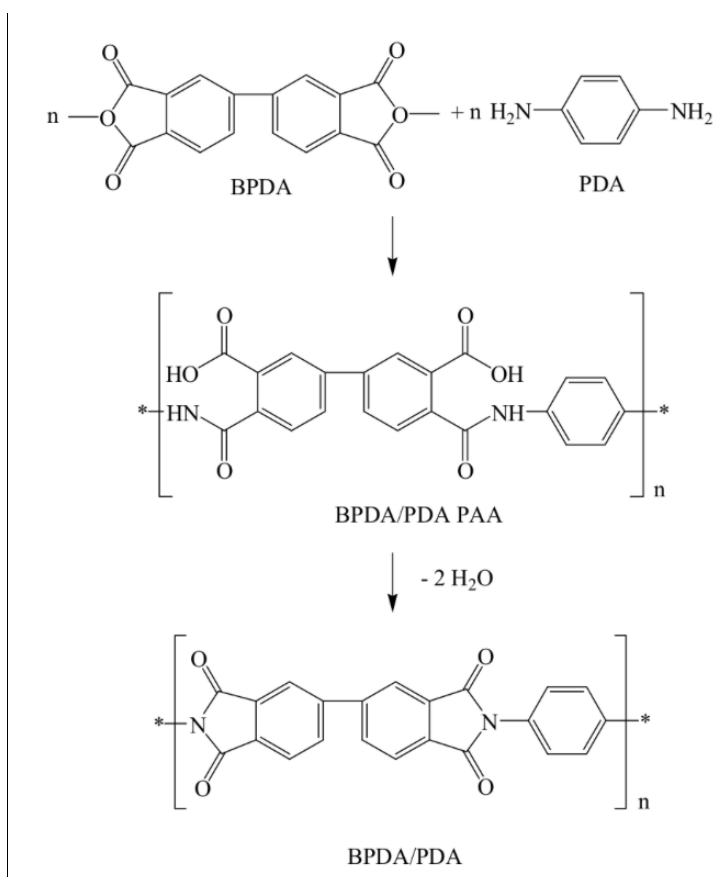

Figure 2-1. Synthesis steps of the BPDA-PDA polyimide

PI properties change as a function of temperature, in particular with a degradation of the electrical resistivity, dielectric properties and failure field. In general, the electrical properties of PI have been studied in the temperature range up to 300°C [119][120]. It was noted that the electrical conductivity varies with both the temperature and the applied electric field. Kapton-H (commercial film) gains two decades of electrical conductivity by increasing the temperature from 120°C to 200°C from 10^{-16} $\Omega^{-1}.cm^{-1}$ to 10^{-14} $\Omega^{-1}.cm^{-1}$. It increases by two more decades at 300°C reaching 10^{-12} $\Omega^{-1}.cm^{-1}$. More recently, Diaham et $al.$ [121] have measured permittivity and loss factor for temperature ranges up to 400 °C for deposited PI films (BPDA-PDA). They concluded that permittivity and loss factor also change strongly with temperature. Figure 2-2 shows an example of the evolution of these parameters as a function of frequency in this temperature range (200 °C to 400 °C). The strong variation in permittivity and dielectric losses observed at low frequencies and high temperatures has been assigned to the presence of charge carriers (electronic and ionic) accumulating at the interfaces and forming a dipole of macroscopic size.
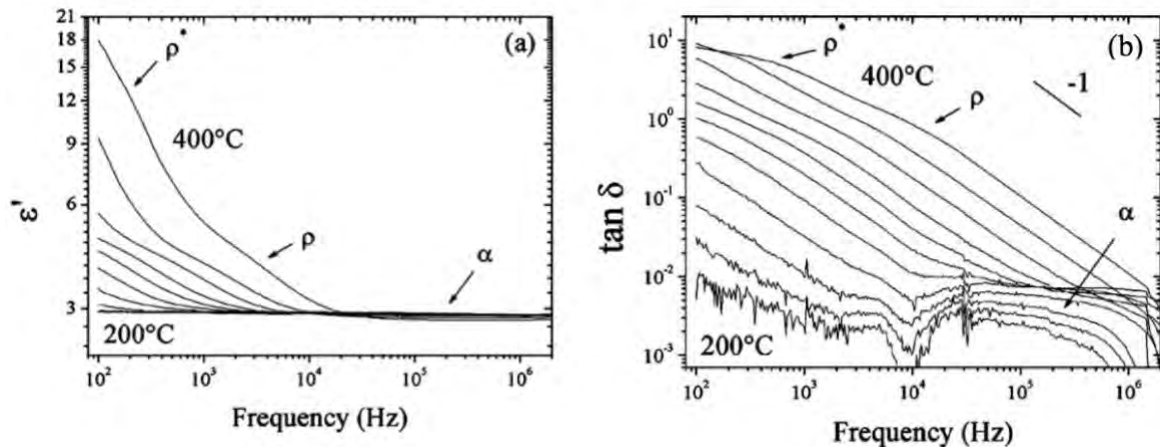
Figure 2-2. Permittivity (a) and loss factor (b) as a function of frequency for polyimide (BPDA-PDA) between 200 and 400 °C (20 °C step)

Moreover, it is well known that PI naturally has a high dielectric strength (>2 MV.cm^{-1}) at 25°C for a few micrometers thick. While, more recently, the effect of the temperature has been characterized by a decrease in the PI dielectric breakdown field with increasing temperature whatever the film thickness or the electrode area. It has been repeatedly shown that between low temperatures (-200°C) and ambient temperature (25°C), the PI failure field reaches values generally between 4 and 5 MV.cm^{-1}. While, for higher temperatures its rigidity decreases to values below 2 MV.cm^{-1} at 250 °C [122][123].

In this thesis, the polyimide host matrix used is a commercial PI2600 series product purchased from HD microsystems based on biphenyltetracarboxilic dianhydride and p–phenylene diamine precursor monomers (BPDA-PDA). The PI2600 product is supplied as a polyamic acid (PAA) precursor solution in N-methyl-2-pyrrolidone (NMP) based solvent. This polyimide has a volumetric mass density of 1.40 g.cm^{-3}. The rigid rod polyimide structure of cured PI2600 products exhibits a desirable combination of film properties such as low stress, low coefficient of thermal expansion (CTE), low moisture uptake, high modulus and good ductility for microelectronic applications.

2.2.2. Nanoparticles choice

As previously seen, PIs lose their mechanical and electrical properties at high temperatures. An innovative way to enhance polyimide physical properties at these temperatures could come from the introduction of inorganic nanoparticles into the matrix. In addition, these new materials would have the advantage of being deposited in the same way as standard PIs. Moreover, for technological applications, it may sometimes be useful (or even very important) to also be able to increase the thermal conductivity of insulating materials so that they contribute to a better heat

dissipation. Therefore, this focuses interest on the types of nanoparticles that are both electrically insulating and thermally conductive.

Studies of recent electrical properties for PI-based ceramic composites are still very rare. The first works date from 2003 and few authors have published on these materials. Some preliminary work shows the evolution of the permittivity and loss factor of a PI/Al_2O_3 (500 nm) [10] and PI/SiO_2 (20 nm) [124] as a function of the loading rate. In both cases, a degradation of dielectric properties was observed when the loading rate increases, which does not allow positive effects related to particle presence to be observed. These negative effects can be explained by the presence of large agglomerates (> 0.5-1 μm). However, a recent literature review on this topic found that a significant improvement in electrical properties can be achieved, especially when the PIs are low loaded with electrical insulating nanoparticles and properly dispersed. Cao *et al*. have studied the electrical properties in a PI/SiO_2 nanocomposite (40 nm) [125], and more recently, Li *et al*. in PI/Al_2O_3 (60 nm) [126]. In both cases, a decrease of conductivity can be observed for low loading rates (2%wt). For higher loading rates, a degradation of electrical performances is noticed and could be related to the formation of agglomerates of submicron or even micron size. Recently, Diaham *et al*. [127] have investigated the electrical conduction and the dielectric breakdown of polyimide/boron nitride (PI/BN) for low filler content (1–2 vol.%), in a large temperature range from room temperature up to 350 °C. The authors highlighted that w-BN (35 nm) nanoparticles act as deep traps for mobile ionic species particularly activated with temperature. Moreover, up to 150 °C, it was confirmed that the nano-structuration of PI slightly decreases the DC conductivity and increase the breakdown field.

In this thesis, it was decided to study PI (BPDA-PDA) matrix loaded with silicon nitride nanoparticles (Si_3N_4). Indeed, Si_3N_4 naoparticles would have the double advantage of being able to strengthen the electrical insulation properties of the PI, while improving its thermal conduction. In addition, these nanoparticles have the advantage of being deposited in the same way as standard PIs. The Si_3N_4 nanoparticles were provided as spherical amorphous nanoparticles (with a volumetric mass density of 2.67 g.cm^{-3} and a diameter of 20 to 40 nm) by SkySpring Nanomaterials Inc., Houston, USA. Although the improved dielectric properties of PI/Si_3N_4 nanocomposite seem promising from both an understanding and an application point of view, it is clear from the state of the art that they have been studied very little to date. This could be explained by the great difficulty in obtaining good quality materials. In addition, the dielectric properties at high temperatures (>150°C) are completely unknown today.

2.2.3. Dispersion and functionalization

According to what has been presented above, it seems obvious that the dispersion quality of nanoparticles in the polymer matrix and the presence of agglomerates (micron size) will play a very important role in controlling the final physical properties of nanocomposites through the development of large interaction surfaces. It can then be expected that the " nano effect " on dielectric properties can be observed when the nanoparticles are well dispersed. As an example to support this, Yang et al. [128] have investigated the nanoparticles dispersion effect on epoxy/ZnO nanocomposite as shown in figure 2-3. It can be seen that its electrical resistivity is improved when ZnO nanoparticles (20 nm) are well dispersed (NEP) compared to cases where they are aggregated (NDNEP) or micron-sized (2-5 μm) (MEP). Moreover, the reduced dielectric loss factor of NEP compared to that of MEP may be due to this "nano effect". However, as the dielectric loss introduced by fillers increases faster, the dielectric dissipation factor of 5 wt% NEP is greater than that of pure EP. NDNEP has the highest dielectric dissipation and this should be attributed to its filler aggregation.

According to the section 2.2.2, we have highlighted the importance of the quality of the nanoparticles dispersion within the polymer matrix in order to obtain improvements in dielectric properties. Moreover, many researches have tended to focus on the strong structural/property links in these materials, which unfortunately remain almost unknown to this day. However, first dielectric properties results, reported mainly at room temperature, seem to show the great difficulty of dispersing nanoparticles in the PI and the considerably negative effects it induces.
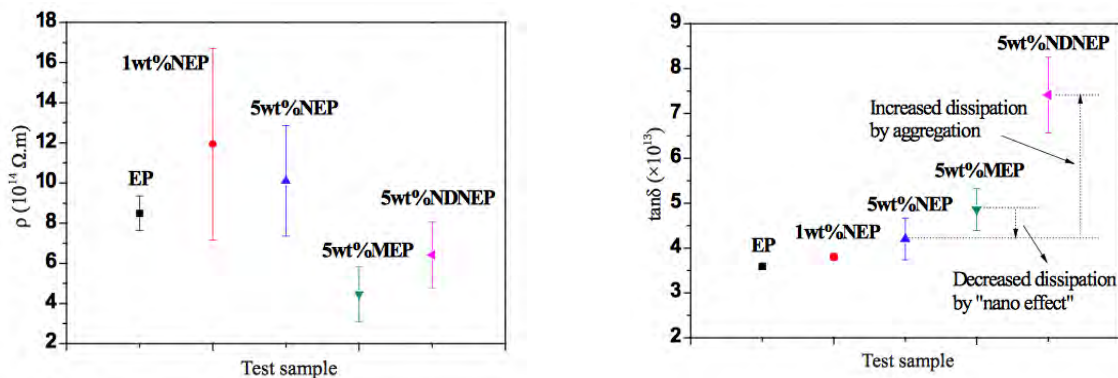
Figure 2-3.Resistivity (left) and tanδ (right) of Epoxy/ZnO nanocomposite. EP: epoxy, NEP: epoxy/ZnO nano dispersed , NDNEP : epoxy/ZnO aggregated, MEP : epoxy/ZnO micro (2-5 μm)

Beyond the dispersion, the quality of the nanoparticle/polymer interphase also appears to be fundamental to the development of nanodielectric effects. Indeed, it is necessary to create as many links as possible between polymeric chains and nanoparticles. In general, surface chemical

treatments of inorganic nanoparticles play a significant role in improving coupling with the polymer and have a significant influence on these materials properties. Chemical elements, known as "compatibilizers" or "coupling agents", increase the interaction and adherence between the polymer and nanoparticles. Moreover, inorganic materials such as clays and oxides are generally hydrophilic, while polymers are generally hydrophobic. This difference in the chemical functionalities of the materials creates a difference in surface tension that reduces affinity, making inorganic nanoparticles and polymers incompatible. For this reason, it is necessary to reduce the surface tension difference between both of materials in order to obtain a good coupling. To solve this problem, silane is commonly used to couple the organic polymer with inorganic reinforcements as mentioned in the first chapter (section 1-5-2).

In this thesis, the Si_3N_4 nanoparticles surface functionalization is obtained by (3-Aminopropyl) triethoxysilane (APTES, 98%) (linear formula: $H_2N(CH_2)_3Si(OC_2H_5)_3$ and molecular weight = 221.37 g/mol) purchased from Sigma-Aldrich. Silane is a silica-based chemical compound containing two types of groups in the same molecule: organic and inorganic (figure 2-4).
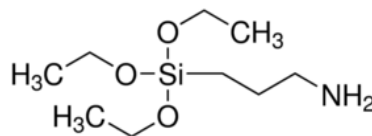
Figure 2-4. (3-Aminopropyl) triethoxysilane (APTES, 98%) formula

2.3. Sample preparation

2.3.1. Manufacturing process

The nanocomposite elaboration process (figure 2-5) is composed of five steps: (1) A 1 wt.% aqueous solution was prepared by mixing 5g of polyamic acid (PAA) with 0.05g of silicon nitride nanoparticles for 15 min in order to obtain a homogeneous solution. Another solution was prepared with the addition of a silane coupling agent in order to obtain a nanoparticle treated sample. (2) An ultra-sonication process (70 °C and 300 W) for one hour (cycles of 2s ON and 12s OFF) was used to reduce the size of agglomerates formed during the mechanical dispersion. Then, to get rid of residual aggregates, (3) a centrifugal decantation by micro centrifuge (Pico21) was used. PAA/Si_3N_4 solutions were placed in 3 ml tubes before being subjected to 21 000 G (14 400 rpm) centrifugal force for 25 min. Only the supernatant mixture was used (1 ml). (4) In order to promote the adhesion between silicon wafer substrate and nanocomposite films, an adhesion promoter (VM-652) from HD MicroSystems was used. Then, the nanocomposite solution was spin-coated

for 30 seconds (3000 rpm) to obtain a thin film with controlled thickness. (5) The obtained PAA/Si$_3$N$_4$ nanocomposite thin film was placed on a hot plate for an annealing at 100°C for 1 min and 175°C for 3 min. Finally, in order to obtain PI from PAA by the imidization process, the thin film was thermally cured in a SPX Blue-M electric oven (figure 2-6) [129].
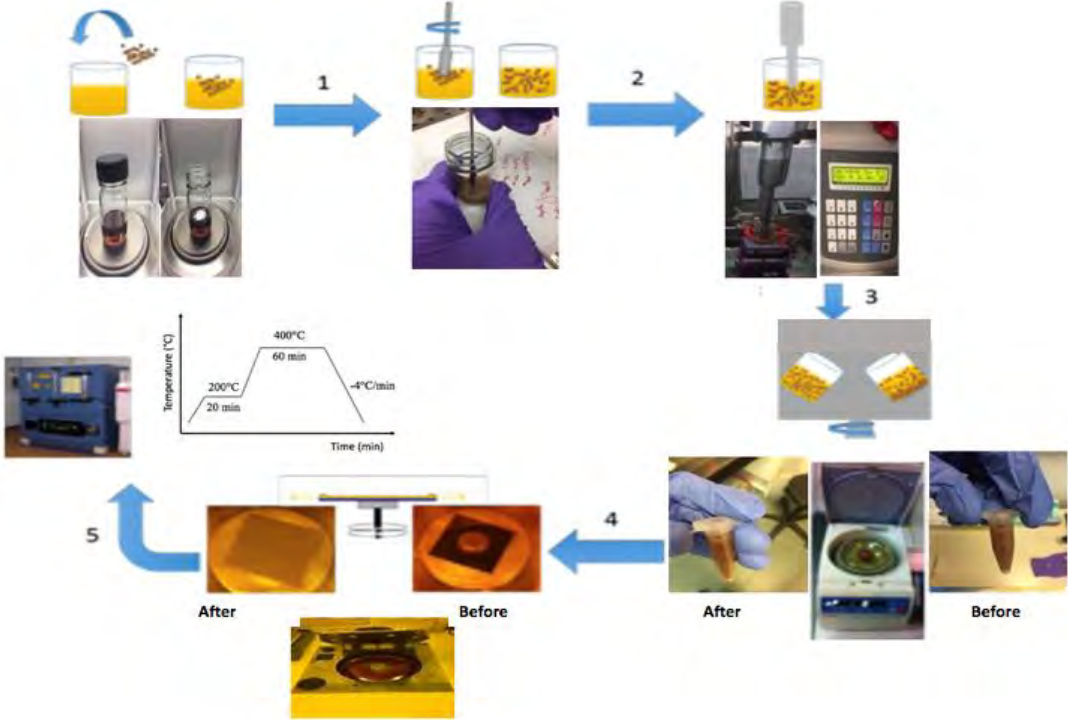

Figure 2-5. Elaboration process of the PI-Si$_3$N$_4$ nanocomposites

The curing cycle for imidization process is shown in figure 2-6 as the following: a first heating cycle at 200°C is applied for 20 min followed by a cycle at 400°C for one hour under nitrogen atmosphere with a controlled cooling of 4°C/min.
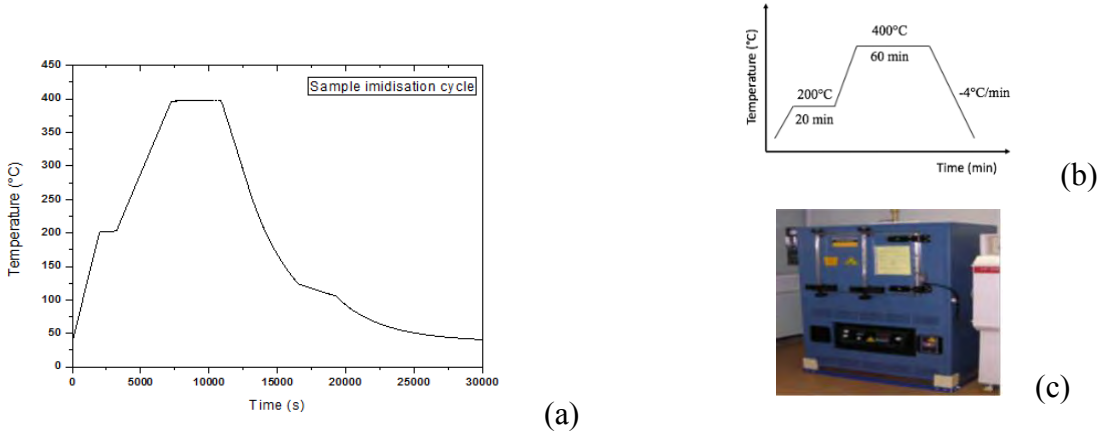
Figure 2-6. (a) Measured and (b) theoretical curing cycle in a (c) SPX Blue-M electric oven for imidization reaction of PI

2.3.2. Sample structure description

Macroscopic electrical measurements were made using capacitive Metal-Insulator-Semiconductor (MIS) structures. To produce such structures, insulator films were deposited on highly doped with phosphorus silicon wafers substrates (N-Ph-type, resistivity between 0.002-0.008 Ω.cm) of 275±25 μm in thickness and 2 ″ (50.8 mm) in diameter. In order to complete the fabrication of MIS structures, a 150 nm gold (Au) counter metallization is applied by sputtering over the entire surface of the nanocomposite films. Then, a wet etching step through a resin mask made by photolithography makes possible to define the geometry of the upper electrodes. Figure 2-7 schematically shows the gold/polyimide/silicon wafer capacitive structures used for electrical tests (cross-section and top side view). Special thanks to Benoit Schlegel who performed the photolithography step.
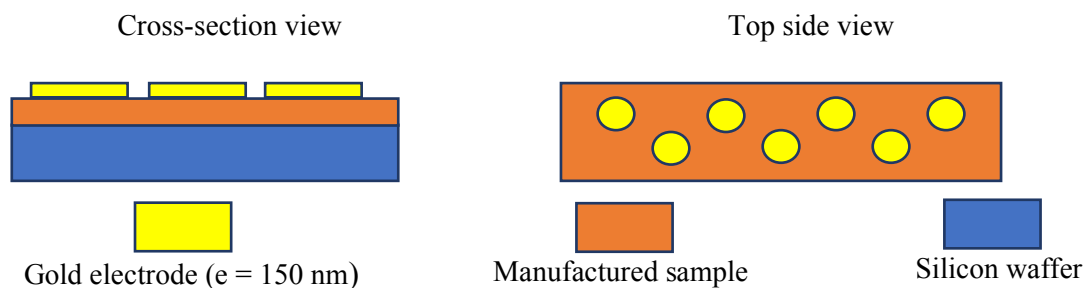
Figure 2-7. Schematic representation of a Metal-Insulator-Semiconductor structure (MIS) with circular geometry

One can distinguish, from figure 2-8, different MIS structures used for electrical measurements. Two diameters of circular electrodes were produced: 0.6 mm for breakdown measurements (a-b) and 5 mm for dielectric spectroscopy measurements (c-d).

(a)   (b)   (c)   (d)
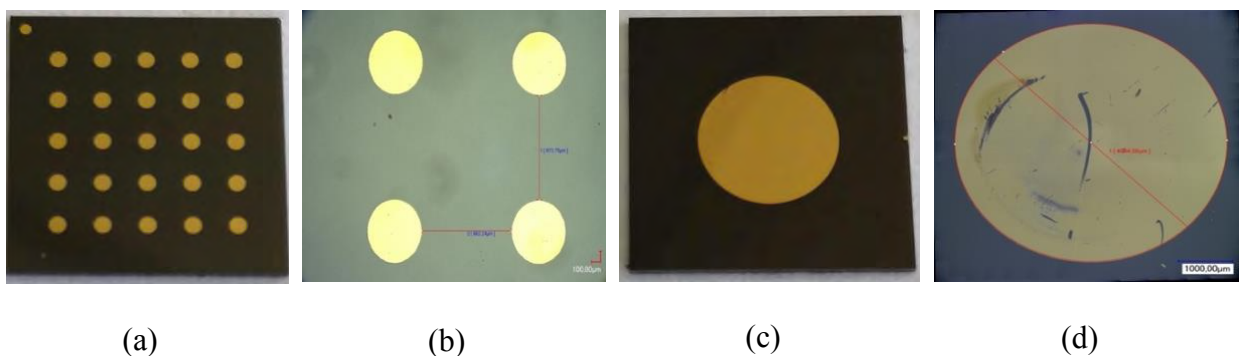
Figure 2-8. MIS structure for breakdown measurements with 0.6 mm diameter (a,b) and dielectric spectroscopy measurements with 5 mm diameter (c,d)

2.4. Macroscopic electrical experiments

2.4.1. Dielectric Spectroscopy

2.4.1.1. Principle

In dielectric (or impedance) spectroscopy, the applied signal is a sinusoidal voltage. This method consists in analyzing the amplitude and phase shift between the voltage at the sample terminals and the current flowing through it [130]. Figure 2-9 shows the measurement principle of dielectric spectroscopy and the waveforms of the recorded voltage signals.
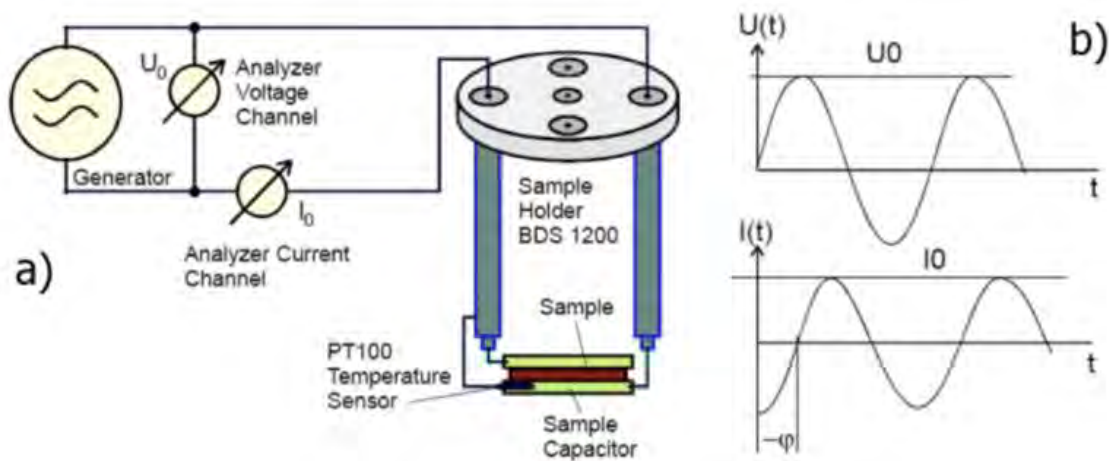
Figure 2-9. a) Principle of dielectric measurement [Novocontrol GmbH] and b) Amplitude and phase shift between ac voltage and ac current through the sample.

From the voltage/current amplitudes ratio, the impedance module |Z| is defined. The phase shift between voltage and current completes the information to give access to the real and imaginary parts of the complex impedance Z*.

$$Z^*(\omega) = Z'(\omega) + iZ''(\omega) = \frac{U_0}{I_0}[\cos\theta(\omega) + i\sin\theta(\omega)] \tag{2-1}$$

Dielectric spectroscopy makes it possible to obtain the complex dielectric permittivity ($\varepsilon*$) which is an intrinsic quantity of the material. The real part of the permittivity (ε') allows to quantify the polarizability of the material while the imaginary part (ε'') is related to the energy dissipated in alternating current. The complex dielectric permittivity and dielectric loss factor are given by:

$$\varepsilon^*(\omega) = \varepsilon'(\omega) - i\varepsilon''(\omega) = \frac{-i}{\omega Z^*(\omega)C_0} \tag{2-2}$$

$$\tan[\delta(\omega)] = \frac{\varepsilon''(\omega)}{\varepsilon'(\omega)} = \frac{-Z'(\omega)}{Z''(\omega)} \tag{2-3}$$

Indeed, the dielectric behavior of an insulator can be represented by an equivalent electrical circuit consisting of passive components R and C arranged in series and/or in parallel (Figure 2-10). The simplest scheme corresponding to the Debye's relaxation is a circuit consisting of a resistor and a capacitor placed in series or in parallel (Figure 2-10 (a) and (b)) [131][132].

The complex admittance Y* expression which represents this equivalent electrical circuit is:

$$Y^* = \frac{1}{Z^*(\omega)} = \frac{1}{R_p(\omega)} + i\omega C_p(\omega) = \frac{1}{R_s(\omega) + \frac{1}{i\omega C_s(\omega)}} \tag{2-4}$$

where R_P and C_P respectively represent the resistance and capacity of the parallel circuit and R_S and C_S those of the series circuit.
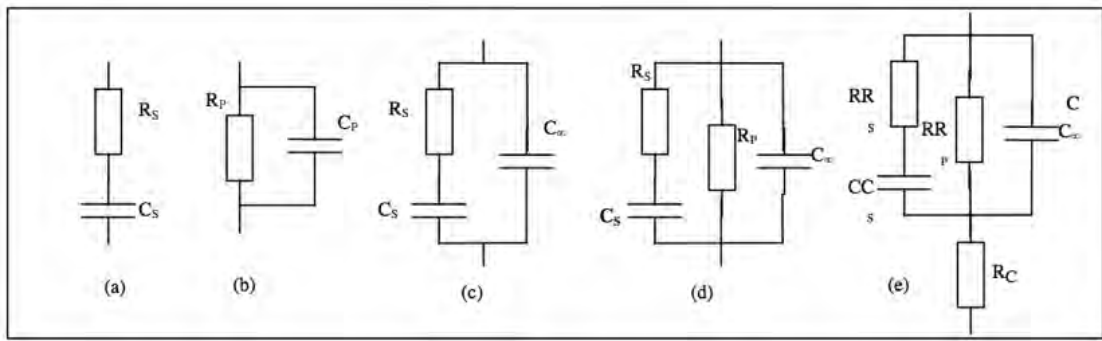
Figure 2-10. Equivalent electrical circuits of the dielectric behavior of an insulator. C∞ is a capacity representing any other physical process independent of frequency

In the following, a simple equivalent electrical circuit is generally used which can be assimilated to an imperfect capacitor (parallel R_P-C_P). Then, the real (ε') and imaginary (ε'') parts of the permittivity and the dielectric loss factor (tan δ) are calculated for each frequency according to the following equations:

$$\varepsilon' = \frac{C_p e}{\varepsilon_0 A} \tag{2-5}$$

$$\varepsilon'' = \frac{e}{\varepsilon_0 A R_p \omega} \tag{2-6}$$

$$\tan\delta = \frac{\varepsilon''}{\varepsilon'} = \frac{1}{R_p C_p \omega} \tag{2-7}$$

where, ω is the angular frequency, δ is the loss angle, ε_0 is the electric permittivity of free space, e is the film thickness and A is the electrode area.

2.4.1.2. Dielectric analysis measurements

The dielectric analysis measurements were carried out using a Novocontrol Alpha-A system shown in figure 2-11 (NOVOCONTROL Technologies GmbH & Co. KG, Germany). Each sample underwent two cycles with isothermal frequency sweeps from 10^6 to 10^{-1} Hz performed every 10°C under a controlled atmosphere of Nitrogen (N$_2$) from -150 °C to 350 °C, applying a sinusoidal alternating voltage of 0.5V RMS.
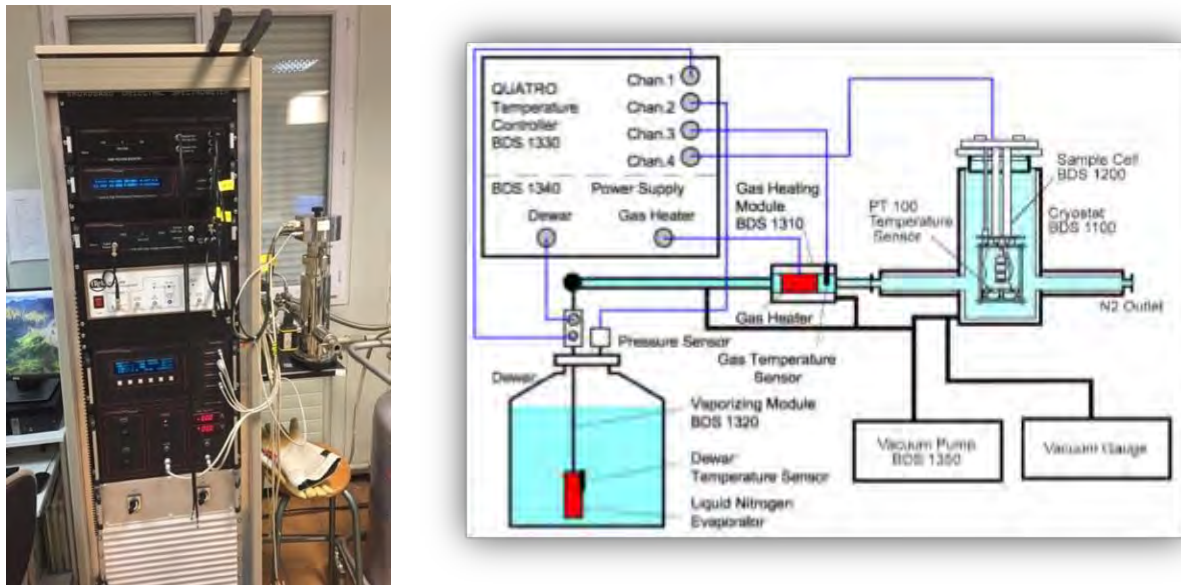
Figure 2-11. Novocontrol Alfa A measuring instrument

Before each measurement campaign, a calibration was performed to compensate interfering impedances related to the connectors as explained in figure 2-12 (calibration performed in open circuit, short circuit and on a standard load of 100 Ω). Temperature regulation and dielectric loss factor resolution are given respectively around ±0.1 °C and $5×10^{-5}$.
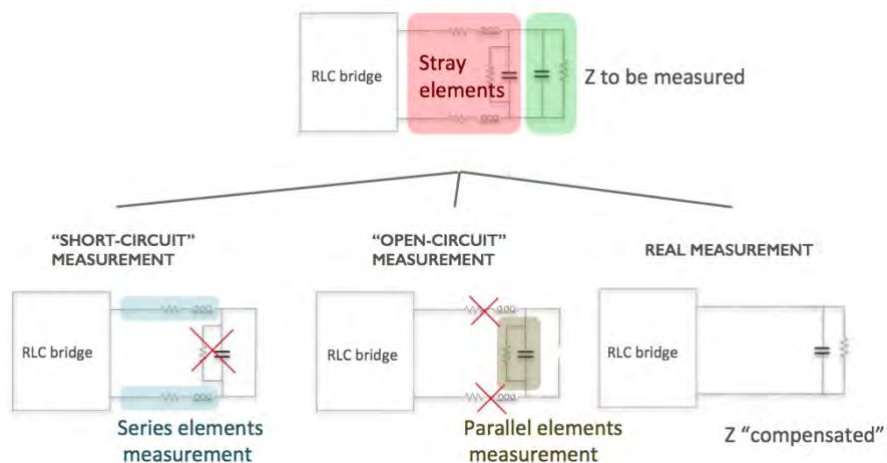
Figure 2-12. Interfering impedances compensation procedure

2.4.2. Breakdown strength measurements

The dielectric strength (or breakdown field) of a material is the maximum value of the electric field that can be applied to it without irreversible degradation making it impossible to reapply the voltage. The breakdown is preceded by a significant increase in the current flowing through the material with destructive consequences: fusion, evaporation, decomposition, carbonization...etc.

In practice, the dielectric breakdown field F_{br} is defined as the ratio between the measured breakdown voltage V_{br} and the distance between the electrodes d (equation 2-8) to which this voltage is applied under specified test conditions. The field should be uniform, i.e. electrodes should be flat and parallel with edges such that they do not cause field reinforcement at any point.

$$F_{br} = \frac{V_{br}}{d} \quad (V/cm) \tag{2-8}$$

Breakdown is the result of complex processes series, into the material under test, that involve mechanisms of intrinsic origin. Breakdown can thus, be due to electronic phenomena (collisions followed by electronic avalanches), electromechanical phenomena (when the insulator is compressed by electrodes that are subjected to electrostatic stress) or thermally if the sample is subjected to heating from conduction current and dielectric losses. Other practical causes can lead to the insulator breakdown in the vicinity of a defect or as a result of a progressive material degradation.

In this thesis, breakdown measurements were carried out using a Signatone S-1160 probe station equipped with micrometric positioners and a sample holder (Chuck) regulated in temperature between 25°C and 500°C thanks to the S-1600R heating system. A 6000 V source (FI 9035HT: electrical safety tester) was connected to samples through the probe station (figure 2-13).

Figure 2-13. Signatone S-1160 probe station (left) and the electrical safety tester FI 9035HT (right)

The station is placed in a Faraday cage to minimize external electrical disturbances and the effect of the ambient environment in the testing room (figure 2-14). Electrical signals are applied using low noise coaxial tips. During measurements, the sample temperature was controlled using a type K thermocouple placed in contact with the surface of the sample with resolution about 2°C. The electrical temperature measurements were thus carried out for 25, 100, 200, 250 and 300 °C.

Figure 2-14. Breakdown testing experimental set-up

Preliminary measurements have been made to adapt the ramp value according to ASTM D149-97a standard test method for dielectrics [133], recommending the use of plane-plane type electrodes to avoid local electric field reinforcements. A 150 V.s^{-1} ramp value was determined according to this standard which specifies that the breakdown must take place between 10 and 20 seconds. At break, the voltage across the sample becomes zero, and the voltage source switches to a current source applying a preset current of 1mA. The maximum voltage supported just before breakdown is recorded. However, primary tests under air showed that neat PI sample breakdown voltage is about 3kV, which corresponds to that of air. In order to avoid a bypass between the adjacent electrodes, the PI breakdown voltage measurements were performed under a dielectric fluid, the Galden HT 270. Since the breakdown is a random phenomenon, for each sample, 10 breakdown measurements on 10 different electrodes per temperature value (25°C - 100°C - 200°C - 250°C and 300°C) were done. A Weibull statistical treatment was applied on experimental data in order to calculate the breakdown strength for each test condition.

2.4.3. Weibull statistics

Empirical approaches have been used to better represent the stochastic nature of breakdown [134].Indeed, the (breakdown) failure is due to a weak point within the material that does not allow to take into account a homogeneous model of this latter. The Weibull model makes it possible to reproduce this dispersion and it is well adapted to lifetime and breakdown statistics. In probability theory and statistics, the Weibull distribution is a continuous probability distribution. It is named after Swedish mathematician Waloddi Weibull, who described it in detail in 1951 [135].

The Weibull distribution (2 parameters) is a reasonable model for describing the failure variability:

$$P(t) = 1 - \exp\left[-\left(\tfrac{t}{a}\right)^b \right] \quad for \ t \geq 0 \tag{2-9}$$

where α is called the scale parameter (or characteristic life) and β the shape. Its complementary cumulative distribution function is a stretched exponential function. The Weibull distribution is related to a number of other probability distributions; in particular, it interpolates between the exponential distribution with k = 1.

The Weibull probability is a graphical method. The data fit to a Weibull distribution can be visually assessed using a Weibull plot. The Weibull plot is a plot of the empirical cumulative distribution function P(t) of data on special axes in a type of $\log_{10}$ ln ($\log_{10}$) plot. The axes are $\log_{10}[-\ln(1-P(t))]$ versus $\log_{10}(t)$. The reason for this variables change is that the cumulative distribution function can be linearized:

$$
\begin{aligned}
P(t) &= 1 - \exp\left[-\left(\tfrac{t}{a}\right)^b\right] \quad for\ t \geq 0 \\
1 - P(t) &= \exp\left[-\left(\tfrac{t}{a}\right)^b\right] \\
-\ln(1 - P(t)) &= \left(\tfrac{t}{a}\right)^b \\
\log_{10}[-\ln(1 - P(t))] &= b\log_{10}\left(\tfrac{t}{a}\right) \\
\log_{10}[-\ln(1 - P(t))] &= b\log_{10}(t) - b\log_{10}(a)
\end{aligned}
\tag{2-10}
$$

The idea of Weibull plotting for a complete sample is to plot $\log_{10}[-\ln(1-P(t_i))]$ against $\log_{10}(t_i)$. Therefore, if the data came from a Weibull distribution then a straight line is expected on a Weibull plot.

There are various approaches to obtain approximation distribution function from data : the most accuracy method [136] (for less than 20 points) is to obtain the vertical coordinate for each point using the median rank of the ith of n samples:

$$
P(i, n) = \frac{i - 0.3}{n + 0.4}
\tag{2-11}
$$

Linear regression can also be used to numerically assess goodness of fit and estimate the parameters of the Weibull distribution by Monte Carlos method (IEEE standard).

2.5. Nanoscale measurements: morphological, mechanical and electrical

2.5.1. Transmission electron microscopy (TEM)

TEM has been used to visualize the nanoparticles shape and their dispersion in the obtained films, as well as the functionalization effect on the treated nanocomposite.

- **Transmission Electron Microscopy principle:**

The principle of TEM is that a beam of electrons is transmitted through an ultrathin section of the specimen. The image contrast is formed due to electron scattering when the beam hits the specimen. Electrons are emitted from an electron gun (filament). Below the electron gun are two or more condenser lenses which demagnify the beam emitted by the gun and control its diameter as it hits the specimen, which is held inside an objective lens just below the condenser lenses. There are two lenses after the objective lens, the intermediate and the projector. Each produces a real and magnified image, which then produces the image on the fluorescent imaging screen or film [137]. The measurements were done using a MET JEOL JSM 2100F -200kV (figure 2-15a).

- **Sample preparation:**

The sample preparation for TEM measurements was done at "Centre de microcaratérisation Raimond Castaing-Toulouse", using the following three steps: (i) the nanocomposite film on a silicon wafer was first sliced using a diamond wire. (ii) Then, the thin slices were sticked together in the form of a sandwich using a resin. (iii) The slices were mounted on copper grids which is adapted to the TEM sample holder (figure 2-15b). Once inserted into a TEM, the sample has to be manipulated to locate the region of interest to the beam, allowing sufficient electron transmission through the sample to obtain a signal for imaging.
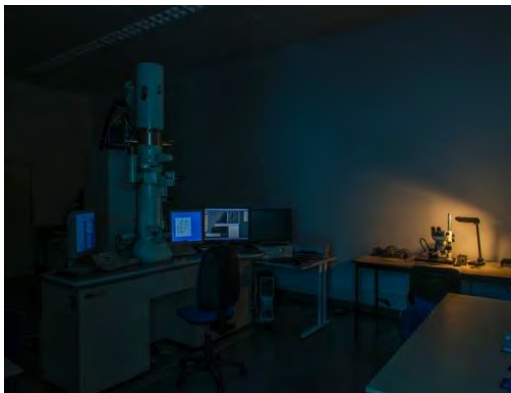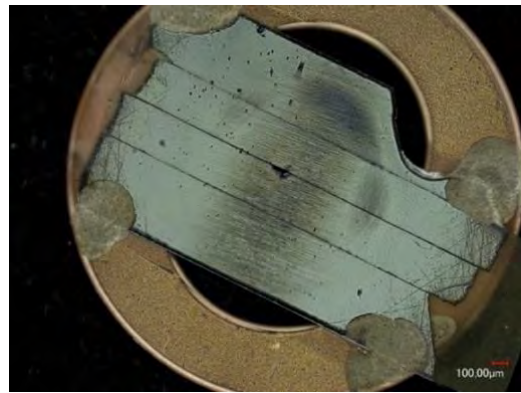
(a)   (b)

Figure 2-15. (a) TEM instrument and (b) Sample structure for TEM imaging

2.5.2. Scanning electron microscopy (SEM)

The principle of SEM is that an electron gun generates electrons and accelerates them through lenses which focus the beam with very small spot size. These electrons interact with the specimen and generate signals that are used to form the image. These microscopes have a resolution between 1 and 5 nm. In addition to the high resolution, they also have a large depth of field, which is the reason that the images appear three dimensional [138]. The JEOL JSM 6700F SEM was used in

order to visualize the atomic force microscopy (AFM) tip quality and geometry needed for the calibration step (see section 2.5.4.5).

2.5.3. Atomic force microscopy (AFM)

2.5.3.1. Principle

The scanning force microscopies started in 1982 with the scanning tunneling microscope (STM) invented by G. Binnig and H. Rohrer [139]. STM works by controlling the tunneling current flowing between a metallic tip and a conductive or semi-conductive surface in a vacuum atmosphere by monitoring the distance of the probe from the surface. However, STM reached limitations to image poorly conductive materials such as biomolecules that also need a specific atmosphere or insulator materials such as polymers. Those limitations served as a motivation for G. Binnig et al. to invent later in 1985 the atomic force microscope (AFM), that opened a broad range of new possibilities in surface analysis at extremely high resolution, giving access to a nanometric imaging with almost any kind of materials [140]. The probe motion in an AFM is altered by the interaction forces with the sample at close proximity (figure 2-16). That implies atomic scale forces, such as Van der Walls forces, electrostatic forces, repulsive forces...etc. [141].
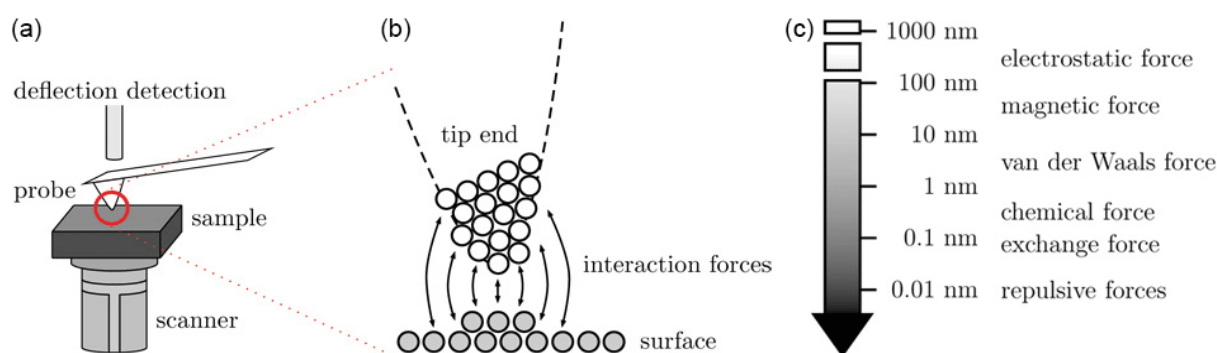
Figure 2-16. (a) Sketch of a macroscopically flat surface probed by a sharp tip. (b) At small separations the atomic structure of tip and sample become important. (c) By approaching the surface from a certain height in z-direction various distance dependent electromagnetic long- and short-range (interatomic) forces are detected

The operating principle of the AFM is as following: the probe is a nanometric tip maintained below a cantilever fixed at one end and free from the other one (see Figure 2-17). Diamond or silicon tip end is characterized by an apex that defines the shape and the curvature radius. The probe is brought into close proximity with the sample to be analyzed, then moved relatively to each other. The displacement system consists of a motor that allows the probe to approach the surface and three piezoelectric tubes, that allow scanning along the X, Y and Z axes. A first tube is used for lateral movements in the X and Y directions and a second tube is used for vertical movements, i.e. in the Z direction. The movement of the probe is usually followed optically by the reflection of a

laser beam from the back side of the cantilever. Reflected beams are collected on a four-segment photodiode (optical position sensitive detection system). A feedback mechanism keeps the cantilever deflection constant by moving it from bottom to top, depending on the topography of the sample. The image of the observed surface is obtained using the recorded data from the sample-tip interaction [142] [143].

(a)

(b)
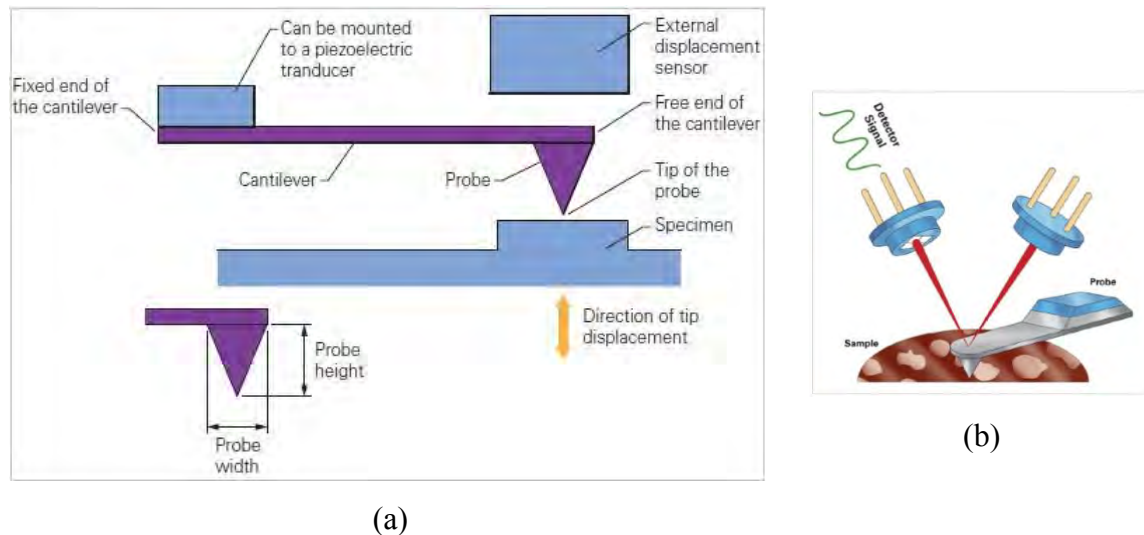
Figure 2-17. (a) Schematic of the cantilever-tip assembly used in an AFM and (b) Schematic of light source, cantilever, and photo detector reassembling the basic components of the light-lever AFM detection system

2.5.3.2. Tapping mode

In the early 1990s, the AFM Tapping Mode (amplitude modulation) emerged [144] and bypassed some limitations of the Contact Mode, particularly a risk to damage the sample surface (or to wear the tip) and an important dependence on humidity conditions and electrostatic forces, making it viable for imaging more sensitive materials. Moreover, the tapping mode used in this work is a Bruker-patented technique that maps topography with high resolution imaging of sample surfaces, by lightly tapping the surface with an oscillating probe tip.

Tapping mode imaging is implemented in ambient air, a sharp probe is brought into proximity with the specimen surface. The probe is oscillated vertically near its mechanical resonance frequency using a piezoelectric. The piezo motion causes the cantilever to oscillate with a high amplitude when the tip is not in contact with the surface. When the cantilever oscillates freely, the movements of the tip and that of the piezo correspond and are in phase. On the contrary, on contact with a sample, at each vibration cycle, the tip hits the surface, limiting and modifying the oscillation amplitude. As the oscillating cantilever begins to intermittently contact the surface, the cantilever oscillation is necessarily reduced due to energy loss caused by the tip contacting the surface. The reduction in oscillation amplitude is used to identify and measure surface features.

One of the main parameters is the Amplitude Setpoint, the fixed value for the reduced oscillation amplitude when the tip is engaged on the sample.

During Tapping Mode imaging, AFM allows capturing height (topography), amplitude error and phase data simultaneously allowing surface structure and material domains to be directly compared.

Topography: As the probe lightly taps the surface, the cantilever's oscillation amplitude changes with sample surface topography, and the topography image is obtained by monitoring these changes and closing the Z feedback loop to minimize them. Topography imaging is directly obtained when recording the vertical position of the piezo (without the oscillating part) (see figure 2-18a).

Amplitude error: The real oscillation amplitude of the probe may change slightly from the Amplitude Setpoint when important topographic variations occur on the sample (to readjust the amplitude so the setpoint, the feedback loop must first quantify the error). This error is recorded during the acquisition.

Phase: In addition to its amplitude, the probe motion can be characterized by its phase relative to a driving oscillator. The phase signal changes when the probe encounters regions of different composition (principally due to the viscoelastic properties) as presented in figure 2-18b. Indeed, phase imaging is a powerful tool that is sensitive to surface stiffness/softness and adhesion between the tip and surface. It is particularly useful in analyzing polymers, composites, and surface coatings (figure 2-18c). Phase shifts are registered as bright and dark regions in phase images, comparable to the way height changes are indicated in height images [145].

Figure 2-18. Schematic representation of the tapping mode: (a) the change in amplitude of oscillation is induced by the topography change, (b) the modification of the material properties introduces a phase shift of the oscillation (indicated in the figure by the arrows). (c) Phase shift over regions of different composition

According to the nature of the force and the usage of appropriate feedback mechanism, several physico-chemical properties can be deduced. In fact, there are several ways to use this technique, and many kinds of data can be deduced, reflecting different properties of surfaces. Thereby, since

its first development, an impressive number of AFM modes have been developed giving the capability of probing, in addition to the topography of different kinds of materials, their mechanical, electrical, magnetic, chemical, thermal and optical properties at the nanoscale.

In the following, a detailed description of Peak Force Quantitative Nanomechanical (PFQNM) and Electrostatic Force Microscopy (EFM) modes for local mechanical and electrical measurements respectively are presented.

2.5.4. Peak-Force Quantitative Nanomechanical mode (PF QNM)

2.5.4.1. Principle

The Tapping mode was a considerable advance in atomic force microscopy and a step towards nanomechanical characterization with its phase contrast, although purely qualitative. To draw this, Peak Force Tapping technology, developed in the late 2000s, allows to open the atomic force microscopy to quantitative characterization, and above all permits to measure materials nanomechanical properties. PeakForce Quantitative NanoMechanical mode (PF-QNM) is based on the Peak Force Tapping technology and is currently the main mode for the mapping of local mechanical properties [146][147].

The basis remains the same as for tapping mode, the vertically oscillating tip hits the sample at each cycle. However, the main control parameter is not anymore, the oscillating amplitude of the cantilever, but the maximum force, or peak force, applied by the tip on the sample surface at each contact. This force is known and monitored precisely with the feedback loop of the microscope. Moreover, in tapping mode the cantilever is excited at a frequency close to its resonance, while in PF QNM technique, using the main Z piezo element, the vertical motion of the cantilever is oscillated at a much lower frequency, typically few kHz. That facilitates the acquisition and the control of the applied force. At each probing position, the force is measured regarding the separation between the tip and the sample. By recording the position of the piezo (Z position) along with the time, successive phenomena, shown in figure 2-19, start first with tip approaching (A), then close to the surface, the force highly strengthens, which roughly drags the tip to jump into contact with the surface (attractive forces B). As the separation continues to decrease, both bodies stay in contact while repulsion forces between them increase. When the set-point Peak Force (C) is reached, the tip is brought to retract back from the surface. However, when the sample is relatively soft, the tip stays adhered to a certain extent (adhesion D) and finally withdraw (E). These curves contain useful information on the mechanical properties of each contact point [147] [148].
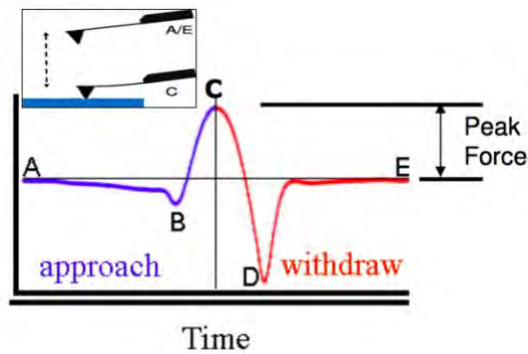
Figure 2-19. Vertical deflection (force) as a function of time for one cycle

For each individual tap, peak force and nanoscale material properties are calculated by collecting one force curve at each pixel on the acquired image. With, as an additional information, the deflection of the laser of the feedback loop on the cantilever, it is possible to deduce the tip position from the piezo Z position. The tip-sample distance is thus accessible. The principle of PF QNM lies on the extraction of force-distance curves that are allowed since the probe is slowly oscillating ($\approx$ 1 kHz) [148]. Figure 2-20 shows a typical force curve on which the local mechanical properties can be evaluated. Peak force is the maximum force value. Deformation is the difference of the separation from force equal to zero to the peak force, it corresponds to the distance made by the tip from the point defined as the contact to the point corresponding to the peak force. The modulus is evaluated from the slope in the beginning of the withdraw curve, just after the peak force (bold green line in Figure 2-20). Depending on the chosen contact model, the calculated modulus can take into account several external parameters, often related to the shape of the tip (see section 2.5.4.3). Adhesion force is the minimum force value, which is affected by the interaction between the tip and the sample and increases with the tip end radius. The adhesion force is the height of the negative force peak in the withdraw curve. The maximum adhesion force with the sample depends on the relative mechanical properties of the tip-sample system. Since the tip is usually sufficiently stiff, a high adhesion force represents a soft specimen, as it retains longer the tip to the surface. The dissipation energy is the area between the approach and the withdraw curves (yellow area in Figure 2-20) [147] [148].

The force curves obtained at each pixel of a scan are directly analyzed during the acquisition to obtain mappings for adhesion force, local modulus, dissipation energy and deformation, along with the traditional topography (height) image.
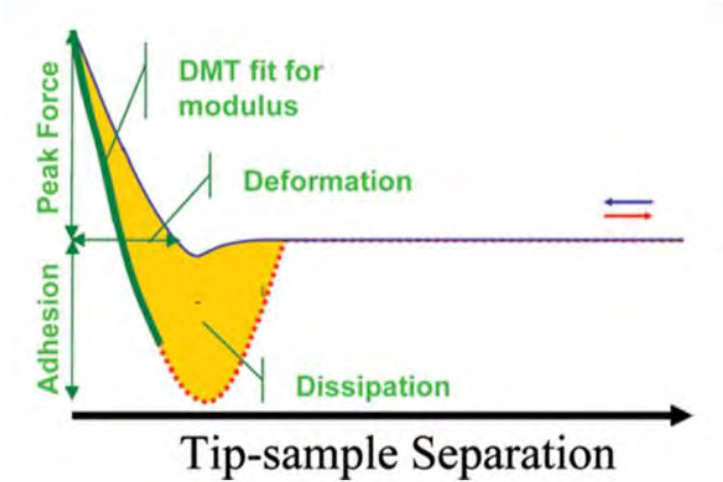
Figure 2-20. Nanoscale mechanical properties obtained from force vs. tip-sample separation curve

2.5.4.2. Peak Force QNM probe selection

It is important to choose a probe that can cause enough deformation on the sample surface and still retain high force sensitivity [149]. Moreover, the spring constant of their cantilever has to be adapted to the scanned material, especially in the case of mechanical measurements, as in Peak Force QNM mode. Therefore, cantilever stiffness should be selected based on the sample stiffness.

Table 2-2 and figure 2-21 present Bruker recommendations for probes selection with respect to the sample modulus value [147]. According to HD microsystems product data sheet, the BPDA-PDA polyimide (PI2611) young modulus is about 8.5 GPa [150]. Then, the chosen reference sample and the probe for PI modulus probing is Polystyrene (PS) and TAP525 respectively. This probe specifications are presented in table 2-3 [151].

Table 2-2. Bruker recommended probes

Sample Modulus (E)	Probe	Nominal Spring Constant (k)
1 MPa < E < 20 MPa	ScanAsyst-Air	0.5 N/m
5 MPa < E < 500 MPa	Tap150A, P/N MPP-12120-10	5 N/m
200 MPa < E < 2000 MPa	Tap300A (RTESPA), P/N MPP-11120-10	40 N/m
1 GPa < E < 20 GPa	Tap525A, P/N MPP-13120-10	200 N/m
10 GPa < E < 100 GPa	DNISP-HS	350 N/m

All the AFM measurements in this work were carried out using a Multimode 8 Scanning Probe Microscope with a Nanoscope V Controller (figure 2-22) and a Nanoscope8 Software version. For AFM image and force curves analysis, NanoScope Analysis v. 1.50 software was used (all from Bruker Corporation). Surface topography and mechanical properties of PI/Si_3N_4 nanocomposites were assessed in Tapping and PF QNM modes using, respectively, a RTESPA probes (nominal spring constant: 50N/m) and TAP525 (nominal spring constant: 200N/m).

Table 2-3. Tap525 specifications

Probe Specifications	Tap525
Tip Radius (nm)	8 nm
Front Angle (°)	15
Back Angle (°)	25
Tip Set Back (µm)	15
Tip Height (µm)	17.5
Side Angle (°)	17.5
Frequency (kHz)	525
k (N/m)	200
Width (µm)	40
Thickness (µm)	6.25
Length (µm)	125
Back Side Coating	40 ±10nm of Al
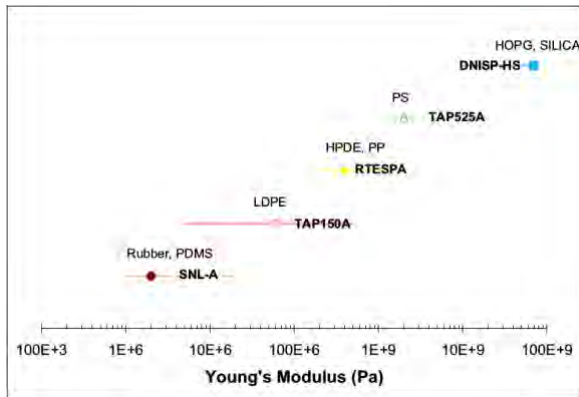
Figure 2-21. Modulus range covered by various probes from Bruker. The modulus of typical reference samples for each range is indicated as well

Figure 2-22. Bruker multimode8 complete hardware setup. 1: PC (monitor, CPU, keyboard and mouse), 2: Nanoscope V controller, 3: Multimode V8 Scanning Probe Microscope (SPM), 4: The OMV-UNIV optical viewing system (helps for aligning Multimode SPMs), 5: VT-102-2 which is an air table for vibration isolation to set the SPM on.

2.5.4.3. Tip/sample contact models

According to Hooke's law in its general form:

$$E = \frac{\sigma}{\varepsilon} \qquad (2\text{-}12)$$

where, E is the modulus, σ the stress, ε the strain. The stress, being a ratio of a force to a surface, depends on the contact geometry. For this reason, the elastic modulus does not depend only on

data accessible with the AFM (force and position of the tip) but also on the geometry of the tip/sample contact. Moreover, measuring properties such as the local elastic modulus requires to make some assumptions, particularly about the contact geometry (which, at nanoscale, cannot be exactly known) and about the general behavior of the material. Consequently, quantitative nanomechanical measurements depend on the use of different models based on contact mechanics. Many models can be applied to the measurement of local modulus by an AFM tip. The models differ mainly between themselves by how they take into account the adhesion forces and by the tip geometry considered. These models exist because it is impossible to know the exact geometry of the actual contact for any tip and at any point on a surface. Each one therefore applies an approximation in particular cases. In the following, a summary on the AFM contact model is described.

Hertz theory

At the end of the nineteenth century, Hertz [152] was the first to describe the distribution of local stresses caused by the contact of two curved surfaces deforming each other in their elastic domain. The Hertz model is based on the following assumptions: (i) the material is isotropic, (ii) all deformations are in the elasticity domain of the material, (iii) the elasticity is linear, (iv) the normal force F, pushing the solids 1 and 2 against each other, follows the same direction than the straight line defined by the centers of the two spheres and (v) there is no friction nor adhesion.

Derjaguin-Muller-Toporov (DMT) model

In order to model the contact point between the AFM tip and a sample surface, two spheres are thus considered (except for Sneddon model). Table 2-4(a) illustrates the tip/sample contact for a hertzian model. However, the Hertz model does not take into account the adhesion forces. The works of Derjaguin, Muller and Toporov [153] have established a model in which such attractive forces act outside the contact (which is repulsive). The contact remains hertzian and these adhesive forces are not able to deform the material. The assumptions of the Hertz model are always applied, and viscoelasticity is neglected. The DMT relation is thus similar to the equation 2-14, with the addition of the adhesive term F_{adh} (equation 2-15). The adhesion force during each contact cycle is directly accessible in AFM Peak Force mode via force curves.

Johnson-Kendall-Roberts (JKR) model

The model introduced by Johnson, Kendall and Roberts [154] describes a non-hertzian sphere-sphere contact or sphere-plane. Unlike the DMT model, the attractive adhesive forces inside the contact zone are taken into account and the exterior forces are neglected. The JKR model was

developed from observations on gelatin and rubber spheres. The model predicts an increase of the contact radius when the interaction is in the repulsive domain, as shown in table 2-4(b).

Sneddon model

The Sneddon model [155] is only applied when the tip is assimilable to a cone, i.e. if the curvature radius of the tip is negligible compared to the depth of indentation. This model describes the contact between a rigid cone and an infinite semi-space. It is more accurate for important indentations (i.e. more than 30nm). Adhesive forces are neglected. Table 2-4(c) illustrates the considered geometry.

Table 2-4 illustrates the tip/sample contact for each model with the respective relations between F the force on the tip, R the tip radius of curvature (this data is evaluated during a calibration step), d the indentation depth, F_{adh} the adhesion force, a is the contact radius, θ the tip angle and E* is the reduced elastic modulus. This modulus represents the elastic deformation that occurs in both sample and tip.
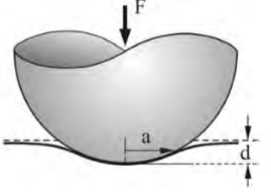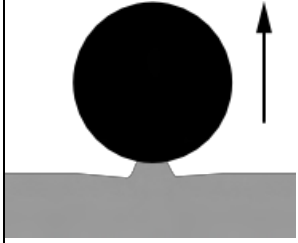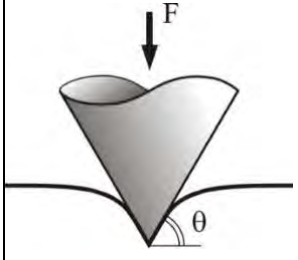
Equations 2-14, 2-15, 2-16 and 2-17 (from table 2-4) allow to obtain according to the selected model the local modulus E* from forces (applied force and adhesive force) and deformation data, measurable at each point of an AFM image with the Peak Force QNM mode (the force and the indentation being known, E* can be deduced). Indeed, knowing the Poisson's ratio of the sample (υ_s) and the tip (υ_{tip}) and assuming infinite elastic modulus for the tip (E_{tip}), the elastic modulus for the sample (E_s) can be calculated using equation 2-13:

$$E^* = \left(\frac{1 - v_S^2}{E_S} + \frac{1 - v_{tip}^2}{E_{tip}} \right)^{-1}$$

(2-13)

Hereafter, it is chosen to consider a fixed Poisson's ratio of 0.3, which is a reasonable average value for common polymers, for all experiments at the nanoscale. Thus, the local modulus (generally the DMT modulus,) considered in this work includes the potential shift of the Poisson's ratio from its default value of 0.3.

Table 2-4. Tip/sample contact illustration for each model with the respective relations for the reduced elastic modulus calculations

Hertz		(a)
	$F = \frac{4}{3}E^*\sqrt{Rd^3}$ (2-14)	

DMT	$F = \frac{4}{3}E^*\sqrt{Rd^3} + F_{adh}$ (2-15)	
JKR	$a = \sqrt[3]{\frac{3E^*}{4R}(F + 2F_{adh} + 2\sqrt{F_{adh}(F + F_{adh})})}$ (2-16)	(b)
Sneddon	$F = \frac{4E^*}{\pi \tan(\theta)}d^2$ (2-17)	(c)

2.5.4.4. Real tip/sample contact on polymers

Dokukin et al. have emphasized several challenges caused by the scale and the unpredicted factors of a real tip/sample contact on reference polymer surfaces (i.e. 2.7 GPa for polystyrene and 0.6-0.7 GPa for polyurethane)[156][157]. Regarding the contact model to use in polymer science, a debate between JKR and DMT model is still ongoing. Tabor [158] has pointed that the adhesion is not only determined by the intrinsic properties of the material in contact but also by the roughness of the surface, which can dramatically modify the adhesion. He showed then that both JKR and DMT theories can be validated experimentally, depending on the adhesion behavior of solids in contact. As a general rule, it can be considered that the stiffer the scanned sample is, the better it is described by the DMT model, while the softer and more adhesive it is, the closer it gets from a JKR type behavior.

Moreover, the DMT model is currently the most used in atomic force microscopy for the calculation of the local elastic modulus. It is, with the Sneddon model, the two only models implemented in Bruker's Peak Force QNM mode, in the version used in this work (Nanoscope v. 8.15). Because the Sneddon model is applied when the tip is assimilable to a cone and the DMT model when the tip is considered to be spherical (at its extremity), it was chosen to use the DMT

one which suits better the TAP525 tip geometry used in this study for nanomechanical measurements.

2.5.4.5. Calibration parameters

For quantitative nanomechanical measurements, according to the used contact model, a three steps calibration must be performed prior to any session [159]. The calibrated parameters are then given to the software to allow the calculations of local mechanical properties from the force curves:

Deflection sensitivity

The first calibration step consists on adjusting the sensitivity to deflection, related to the tip and photodiode [160]. The sample placed must be flat and much more rigid than the cantilever. After that, the laser position must no longer be touched. During data acquisition, the deflection of the cantilever (in V) and the position of the piezo (Z in nm) are recorded at each tap (or pixel). In order to convert these data into force (in nN) versus separation (in nm), the deflection sensitivity of the cantilever should be measured. This is the distance that the cantilever is really deflected for a measured change in the photo-detector voltage (nm/V).

Deflection sensitivity depends on the cantilever type and the laser path from the back of the cantilever to the detector. Static (ramp mode) and dynamic (scan mode) deflection sensitivity are determined using Force Distance Curve and Scanning mode respectively on hard sapphire sample. In order to calculate the Young modulus, the "Sync Distance New" parameter should also be measured on the sapphire sample at first. Then the obtained value could be applied to an unknown sample. This parameter represents the distance (in 2 μs time steps) between the start point of an extend-retract cycle and the point of peak force. The force F can then be easily calculated in nN, by multiplying the deflection Δl of the cantilever by its spring constant k (F = k.Δl).

Spring constant

To know exactly the tip/sample interaction force, the spring constant k of the cantilever must be known. There are many ways to determine k, but the most reliable and convenient are the Thermal Tune method (adapted for any kind of soft cantilever i.e. k < 1 N/m [160][161]) and the Sader method (adapted to stiffer cantilevers such as the TAP525 probe one [162] [163]). In both methods the cantilever must be free (not engaged on a sample). As the nominal spring constant k for TAP525 tip is high (200N/m), thermal tune is no long appropriate and the Sader method [164] needs to be applied for a rectangular cantilever following equation 2-18 :

$$K = 0.1906.L.b^2.\rho f.Qf.\Gamma i.(\omega f).\omega f^2 \qquad (2\text{-}18)$$

where b and L are the width and the length of the cantilever respectively. These values were experimentally measured using the JEOL JSM-6060LV Scanning Electron Microscope (SEM) as shown in figure 2-23. ρ_f is the density of the fluid in which the cantilever is immersed (air in this case), Q_f the quality factor in air, ω_f the resonant frequency in air and i the imaginary component of the hydrodynamic function Γ as explained in [164]. Γ depends on the Reynolds number which states:

$$Re = \frac{\rho_f \cdot \omega_f \cdot b^2}{4\eta} \qquad (2\text{-}19)$$

where η is the viscosity of the surrounding fluid (air) and is independent of the cantilever thickness and density. The resonance frequency ω_f and the quality factor Q_f of the cantilever required in Sader method were obtained by using the mechanical tune function in tapping mode AFM. Spring constant k calculation was done on Sader's website [165] from the data mentioned above.
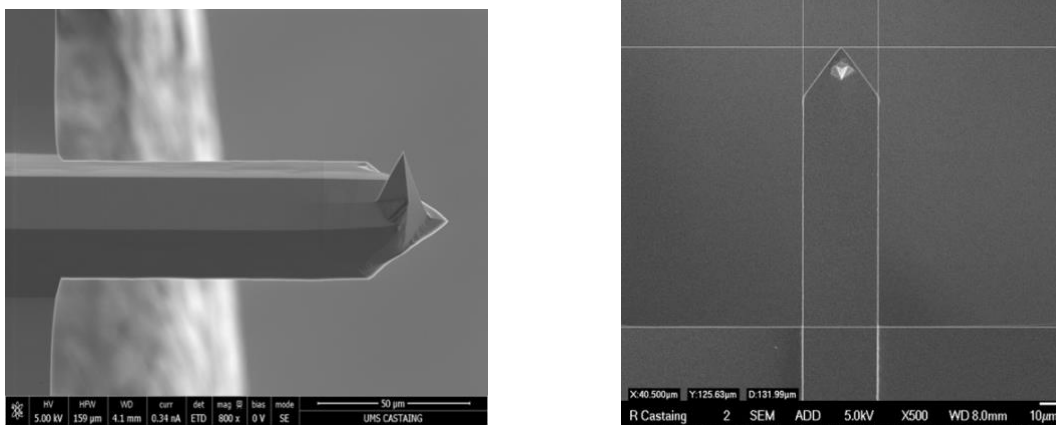
Figure 2-23. TAP525 cantilever SEM image for spring constant determination

Tip radius

The last calibration step to be able to calculate local mechanical properties is related to the shape of the end of the tip. There are two methods of obtaining calibrated tip radius (R_{tip}), the absolute method and the relative method [147].

The first method (the absolute method) requires accurate measurement of the tip end radius, typically by scanning a tip calibration artifact sample and analyzing the resulting image. This type of sample exhibits a very high roughness, due to features. The shape of the tip can be revealed from AFM topography image of those features. By automatically choosing the appropriate peaks and by estimating if the tip is blunt or not (in order to use the sphere plane contact models), the tip radius (R_{tip}) calculation is then provided using the Nanoscope Analysis software. Unfortunately, because of the accumulation of error factors that are not compensated, and that are impossible to

evaluate (i.e. the fact that the tip apex is never perfectly spherical), this method is decreasing in popularity.

The second method (the relative method) avoids accumulated errors that can cause errors in modulus measurements. The tip radius here is not directly measured but evaluated by scanning a sample of known modulus using Peak Force QNM, by adjusting the Tip Radius parameter to make the measured modulus equal to the expected value of the reference sample. The advantage of using the real modulus of the reference sample bypasses the mentioned error factors. However, it requires a reference sample that can be measured by the same probe as the unknown sample (see figure 2-21). Moreover, the calculated tip radius is here virtual and relative to the conditions in which it is determined. To be able to consider the measurements quantitative, the tip/sample contact geometry on the reference sample should be similar to the studied samples. It is thus often advised to choose a reference sample with an elastic modulus close to that of the studied sample, but the most important is to adjust the applied force (Peak Force Setpoint in QNM mode on Bruker systems) so that the deformation matches reasonably the one obtained on the reference sample. For the nanomechanical imaging of polymers, the reference samples have thus to be amorphous, isotropic and as flat as possible.

In this work, tip radius was calibrated using the relative method over a polystyrene film (provided by Bruker with a nominal modulus of 2.7 GPa) as a reference sample, whose mechanical properties are close to PI ones. As the results for this calibration on TAP525 probe used for PI local nanomechanical measurement, the deflection sensitivity is 36 nm/V, spring constant (k) is 159 N/m, sync distance new value is 77.28 and the peak force setpoint is 0.05 V $\approx$150 nN to get 1<d<3 nm deformation depth. TAP525 cantilever width and length are around 40.5μm and 125.63μm respectively. The resonance frequency (ω_f) and quality factor (Q_f) of the cantilever that are required in Sader's method were obtained by using mechanical tune in tapping mode AFM. Their respective values are 519.6 kHz and 1002. Once the calibration steps completed, the Peak Force QNM measurement operation was proceeded for nanocomposite samples using Nanoscope software v8.15 as user interface.

2.5.5. Electrostatic Force Microscopy (EFM) for dielectric permittivity probing

2.5.5.1. Electrostatic Force Microscopy - principle

The electrostatic force microscopy (EFM), first introduced by Martin *et al*.[166] [167], detects weak but long-range electrostatic forces. EFM differs from a conventional AFM by a conductive probe acting as an upper electrode, and a metallic sample holder used as a counter-electrode,

creating together an equivalent of a capacitor. In order to make the probe sensitive to electrostatic interactions, the cantilever and the tip are metallized through the deposition of a thin metal film on their surface (the deposited thickness is of the order of 25 nm), such as: chromium, chromium-gold, platinum-iridium, titanium-platinum, carbide Tungsten, titanium nitride etc. [168].

EFM measurements are performed with a two steps process (Figure 2-24) [169]. (i) First, the topography is obtained with tapping mode, (ii) then the tip is lifted (lift Mode) and the frequency/phase shift of the mechanical oscillation, induced by electrostatic force, is acquired. The electrostatic force induces a resonance frequency shift Δf_0 expressed as following:

$$\Delta f_0 = -\frac{f_0}{2k}\frac{dF(\omega)}{dz} \qquad (2\text{-}20)$$

where, Δf_0 is the frequency shift, k is the cantilever spring constant, f_0 is the resonance frequency and $\frac{dF(\omega)}{dz}$ is the force gradient. An attractive (repulsive) force induces a shift toward lower (higher) resonance frequencies.
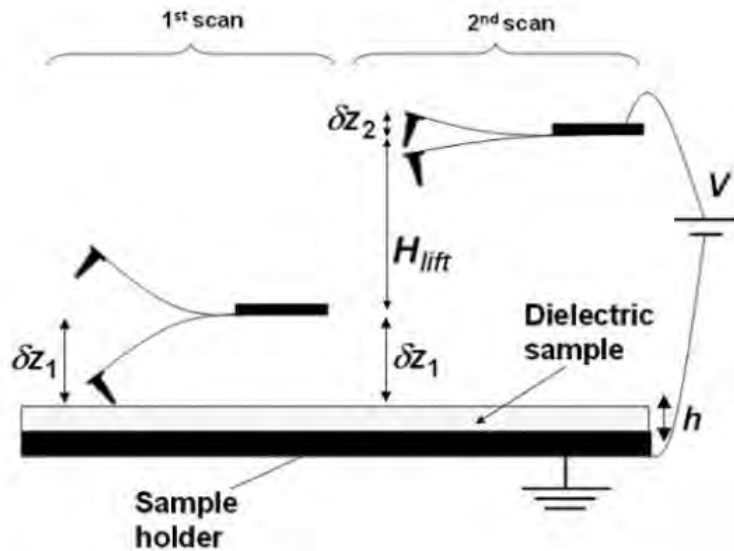
Figure 2-24. Principle of the double-pass method

2.5.5.2. Dielectric permittivity determination using EFM - principle

C.Riedel et al. [169][170] have developed a method based on EFM measurement, which permits to determine dielectric permittivity at nanoscale. This method is based on the measurement of the resonance frequency shift Δf_0 for two different DC-voltage bias.

The $a_{\Delta f}$ parameter is deduced experimentally using the following equation:

$$a_{\Delta f} = \frac{\Delta f_0(V_1) - \Delta f_0(V_2)}{V_1^2 - V_2^2} \qquad (2\text{-}21)$$

where $\Delta f_0(V_i)$ is the frequency shift measured with a bias V_i applied on the tip.

From the theoretical point of view, the $a_{\Delta f}$ parameter is expressed by:

$$a_{\Delta f} = -\frac{f_0}{4k}\frac{d^2 C}{dz^2} \tag{2-22}$$

where $d^2 C / dz^2$ is the second derivative of the capacitance C. The second derivative of the capacitance is determined theoretically using electrostatic force modelling.

2.5.5.3. Dielectric permittivity determination using EFM – experimental conditions

In order to locally characterize the interphase permittivity, EFM appears as a promising technique owing to its sensitivity to the sample capacitive response [110]. In the context of this thesis, interphase permittivity has been calculated using interphase thickness data obtained from PF-QNM.

For EFM measurement, a PtIR-coated silicon tip (figure 2-25) with a resonance frequence f_0 of 66.1kHz, a spring constant k of 2.74N/m (determined by thermal tune) and a radius of 26nm (determined by SEM) was used.

EFM frequency shift Δf_0 measurements were done using bias applied to AFM of 0V as reference and 10V with 50nm-lift. Electric field distribution in air and in the dielectric or nanodielectric layer was computed using a 2D-axisymmetric finite element model on COMSOL Multiphysics®. Mesh was refined close to AFM tip and Si_3N_4 nanoparticle. Dielectric permittivity was fixed at 3.5 and 7.5 for PI and Si_3N_4 respectively. The dielectric layer was assumed free from electrical charges and no charge conditions were applied on the free boundaries of the simulation air box. These conditions ensure no edge effects. Bias was applied on AFM tip and sample backside was grounded. Electrostatic force F_e was computed using electrostatic field E following equation 2-23. Second derivative of the capacitance is consequently deduced from electrostatic force gradient (equation 2-24).

$$\boldsymbol{F_e} = \frac{\varepsilon_0}{2}\iint_{tip}\|\boldsymbol{E}\|^2 d\boldsymbol{S} \tag{2-23}$$

$$\frac{d^2 C}{dz^2} = 2\frac{dF_e}{dz} \tag{2-24}$$

with ε_0 is the dielectric permittivity of free space and S is the tip surface.

We would like to mention that the EFM measurements and modeling have been performed in collaboration with Dr. Christina Villeneuve-Faure from Diélectriques Solides et Fiabilité (DSF) team at LAPLACE laboratory.
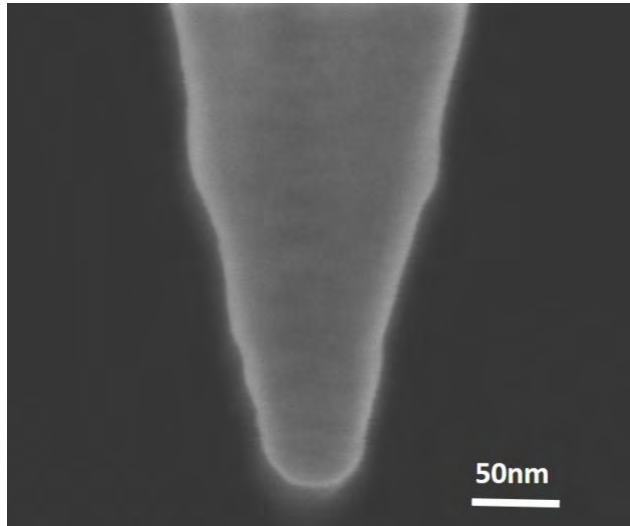
Figure 2-25. Scanning electron image of a typical PtIR-coated silicon probe

2.6. Conclusion

In this chapter, the studied nanocomposite material is presented. The matrix is a polyimide (PI) filled with silicon nitride (Si_3N_4) nanoparticles. The optimization of the manufacturing process leading to a good dispersion of nanoparticles within the matrix is detailed. The test structures and the different multi-scale experimental techniques used to characterize both macroscopic and nanometric properties are also presented. The basic working principles of all these techniques are reported as well.

The aim of this work is to better understand the role of the interphase on the final nanocomposite properties change. So, a local characterization of interphase regions were done in order to measure their structural (thickness), mechanical (Young modulus, deformation and adhesion) and electrical (permittivity). Consequently, methods derived from AFM: the Peak Force Quantitative Nano Mechanical (PFQNM) and Electrostatic Force Microscope (EFM) modes, were used for local measuremenst. In addition, macroscopic experimental technics, such as breakdown strength and dielectric spectroscopy, were used to highlight the effect of nanoparticles (with untreated and treated surface) on functional nanocomposite properties

In the next chapters, we will therefore present the results of local (interphase) and macroscopic (nanocomposites) properties of PI/Si_3N_4 films. The impact of the Si3N4 nano-loading on the dielectric properties of PI, and the effects of Si_3N_4 functionalization will be studied in particular.

3. Nanocomposite local measurements

Content

3.1 Introduction

The aim of this chapter is to characterize the interphase region in PI/Si_3N_4 nanocomposites. For this reason, silane treated and untreated nanoparticles were used in order to analyse the effect of their surface functionalization on their dispersion and on the interphase properties. TEM and AFM tapping mode were used to investigate the quality of the dispersion. Moreover, mechanical (Young modulus) and electrical (permittivity) interphase nanoscale properties were measured using the quantitative nano-mechanical (PF QNM) and the electric force microscopy (EFM) modes of AFM respectively. These mechanical and electrical quantitative results allow us to compare the interphase dimension and properties between treated and untreated Si_3N_4 nanoparticles in order to correlate them to macroscopic properties modification.

3.2 Nanocomposite measurements

3.2.1 Comparison of Si_3N_4 nanoparticles before and after functionalization by TEM

Si_3N_4 nanoparticles used in this study were first dispersed in ethanol (silane was added to the solution for the treated ones), then investigated by TEM in order to show the nanoparticles average diameter, shape and dispersion quality. TEM images of Si_3N_4 nanoparticles suspension before and after modification are shown in figure 3-1 with different scales. The nanoparticles agglomeration can be clearly seen in figure 3-1(a), while their dispersion after functionalization has been greatly improved as shown in figure 3-1(d). One can notice that the silane treatment affects the quality of dispersion. Moreover, it was seen that the surface modification can effectively improve nanoparticles dispersion stability and that the nanoparticles size was less than that of the unmodified Si_3N_4. A grey area was seen on the surface of the solid particles (figure 3-1(b, e)). This area is more visible in the case of modified nanoparticles. This suggests that a chemical reaction takes place on the surface of the Si_3N_4 nanoparticles. The silane agent is grafted on the surface and the agglomeration is decreased.

However, the TEM images of both treated and untreated nanoparticles show a high degree of inhomogeneity in their size with an average diameter between 20-40 nm. Furthermore, it can be seen from these images that nanoparticles have a pseudo-spherical form.
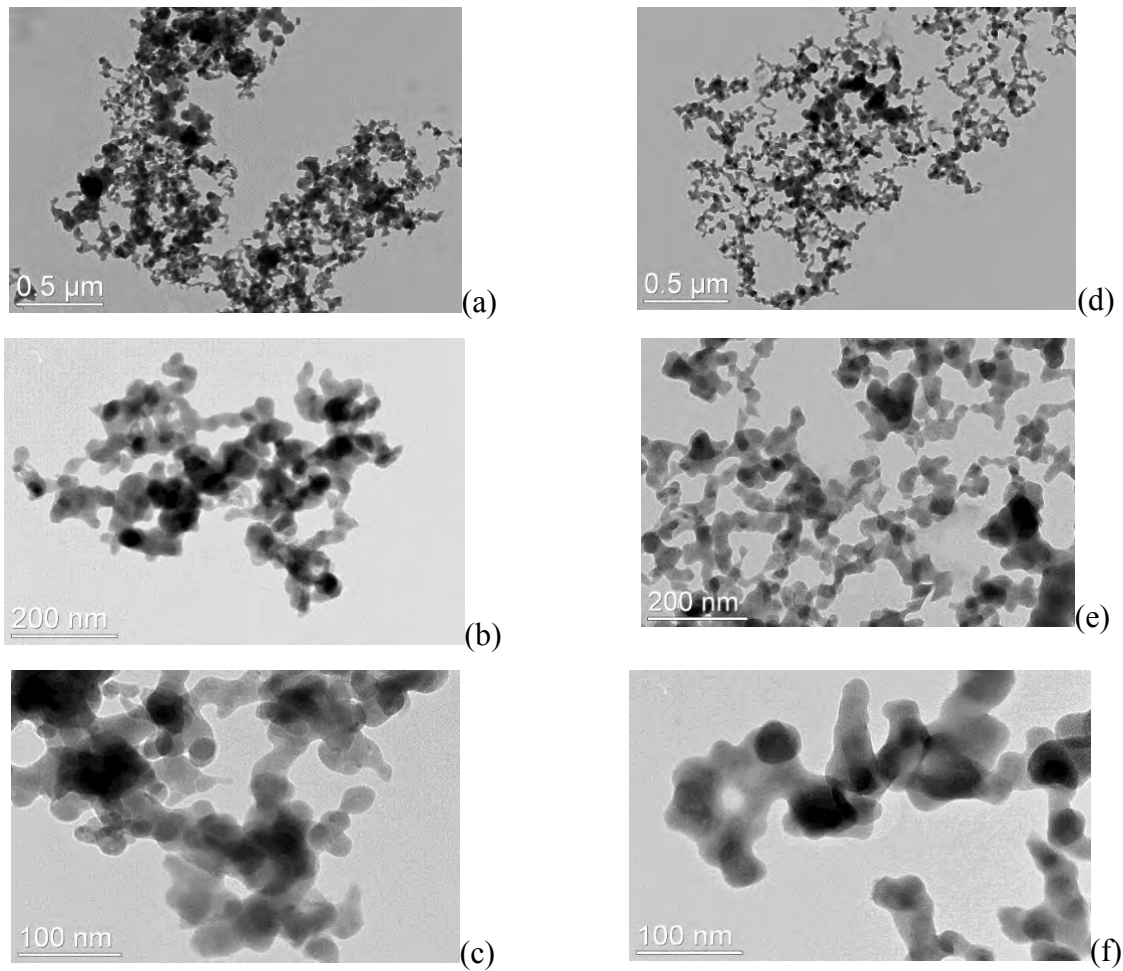
Figure 3-1.Different scale TEM images of Si_3N_4 nanoparticle powder dispersed in ethanol (left) untreated nanoparticles and (right) silane-treated ones

3.2.2 PI/Si$_3$N$_4$ nanocomposite with untreated nanoparticles

The AFM tapping mode is used first to measure the Si_3N_4 nanoparticles diameter on the surface of the nanocomposite as presented in figure 3-2(a). Phase image for 400 nm^2 scan area shows five visible particles. Measurements show different values of particle diameter varying between 34 nm and 73 nm as presented in figure 3-2(b). It can be seen that these nanoparticles have a diameter size of 30 to 40 nm (D_1 and D_2) while the high value of some measured diameters size, as for D_3, D_4 and D_5 indicates the presence of some small clusters within the nanocomposite material. The average diameter of these five particles/clusters is equal to 49.8 nm.
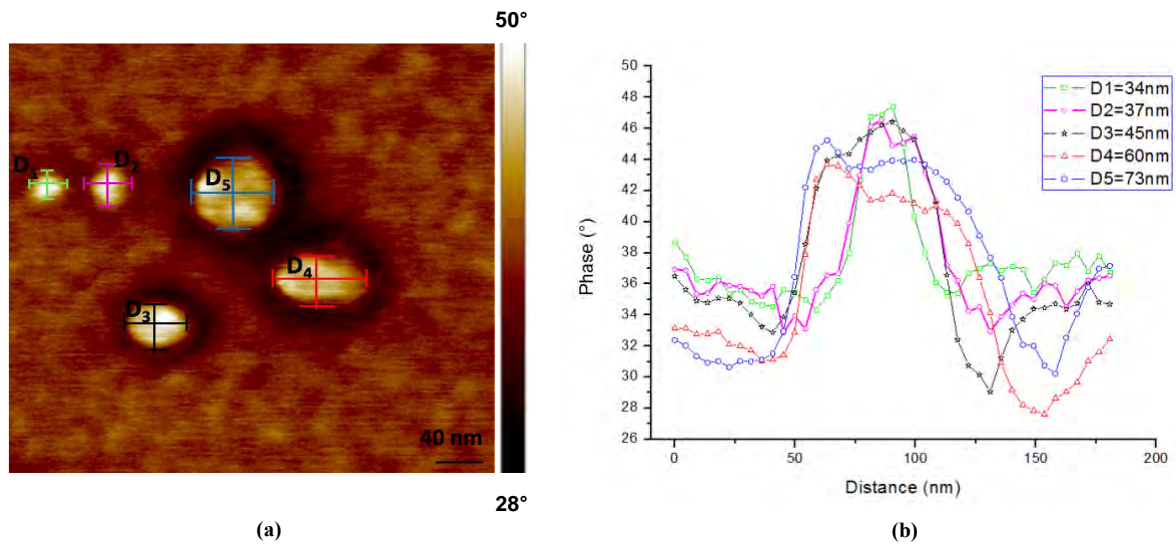
Figure 3-2. (a) PI/Si$_3$N$_4$ phase image, (b) phase cross section for nanoparticles diameter measurement. Scan size of 400nm^2

Moreover, the corresponding 2 μm^2 scan area, where topography and phase images are compared (figure 3-3 (a,b)), shows that the nanocomposite presents a poor dispersion of the Si$_3$N$_4$ nanoparticles within the PI matrix. In addition, 3D AFM images shown in figure 3-3 (c,d) allow us to discuss two typical categories of completely embedded and partially embedded Si$_3$N$_4$ nanoparticles within PI matrix. In fact, topography images show the height profile on the sample surface while phase images are related to the surface material properties. In other words, only the protuberant particles are visible on the topography image while both the protuberant and immersed particles are visible in phase image as illustrated in figures 3-3(c) and (d), respectively.

(c)   **(d)**
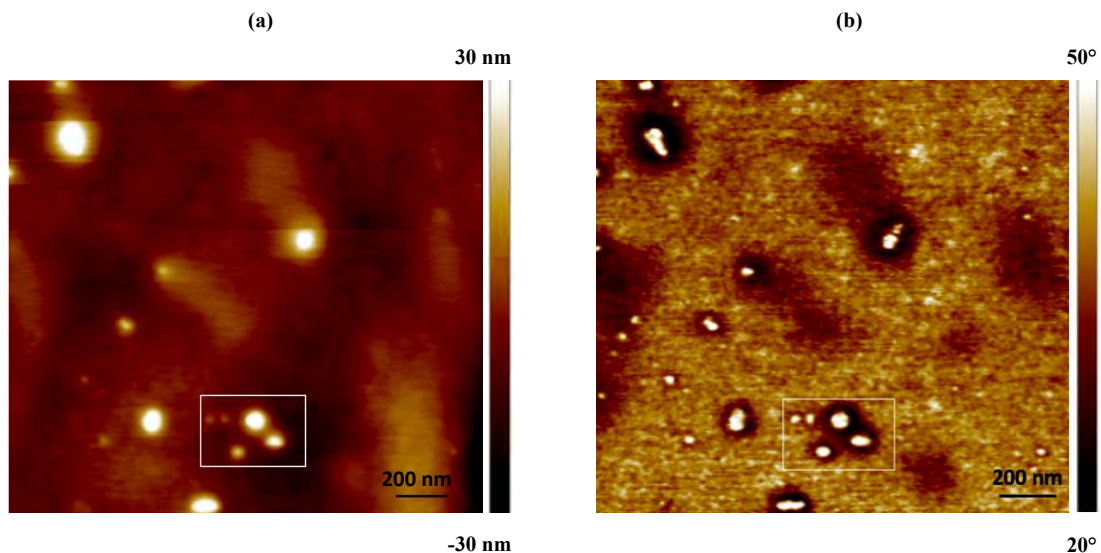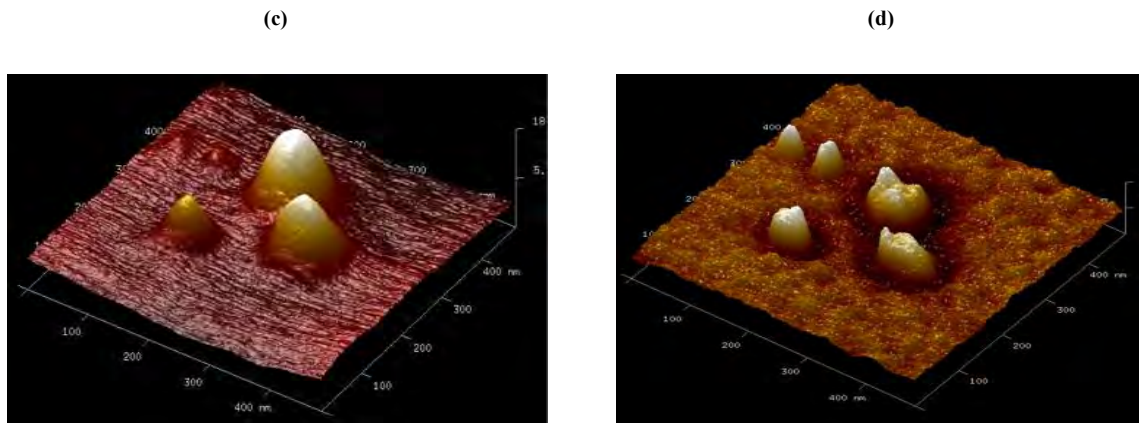
Figure 3-3. PI/Si$_3$N$_4$ tapping mode: top: AFM 2D images (scan size of 2μm^2), (a) Topography, (b)
Phase, bottom: AFM 3D images (scan size of 400 nm^2) (c) Topography, (d) Phase

In addition to particles dimension, particles dispersion in the matrix is another key factor in controlling interfacial bonding between them and the polymer matrix. Figure 3-4 shows TEM images for the untreated PI/Si$_3$N$_4$ film. These TEM images enable us to observe the quality of the nanoparticle dispersion within the film. It can be seen that images show dark clouds. Dark clouds are supposed to be nanoparticles aggregates. In addition, images show a nanoparticles diameter of approximately 20 to 40 nm, which is the mean diameter of the Si$_3$N$_4$ nanoparticles according to the data sheet.
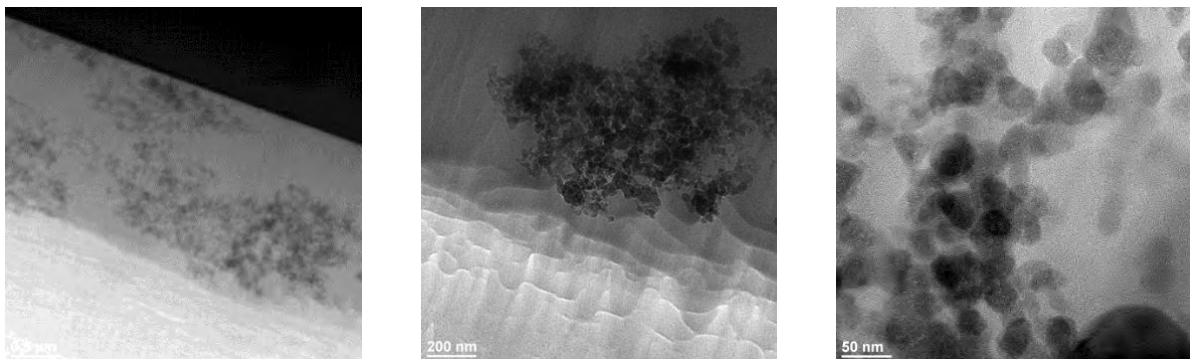
Figure 3-4. TEM images with different scale of untreated PI/Si$_3$N$_4$ sample

Furthermore, on the AFM mapping performed on the untreated PI/Si$_3$N$_4$ nanocomposites (see figure 3-5) oat a large scan area (20 μm^2), it is possible to observe the impact of the Si$_3$N$_4$ nanoparticles on the PI/Si$_3$N$_4$ film surface. According to the AFM tapping mode images in figure 3-5, topography (left) shows a rougher surface for untreated nanocomposite than PI. The measured root mean squared (RMS) roughness is equal to 91.2 nm. In phase images (right), untreated particles appear to be stacked and agglomerated. This might be caused by a high Van der Waals inter-particles attraction between the primary particles themselves.

To sum it up, both TEM and AFM images show that the dispersion of Si_3N_4 untreated nanoparticles within PI matrix leads to aggregate formation. Thus, the NPs dispersion is not optimized and there is still room for improvement, e.g. by suitable surface treatment.
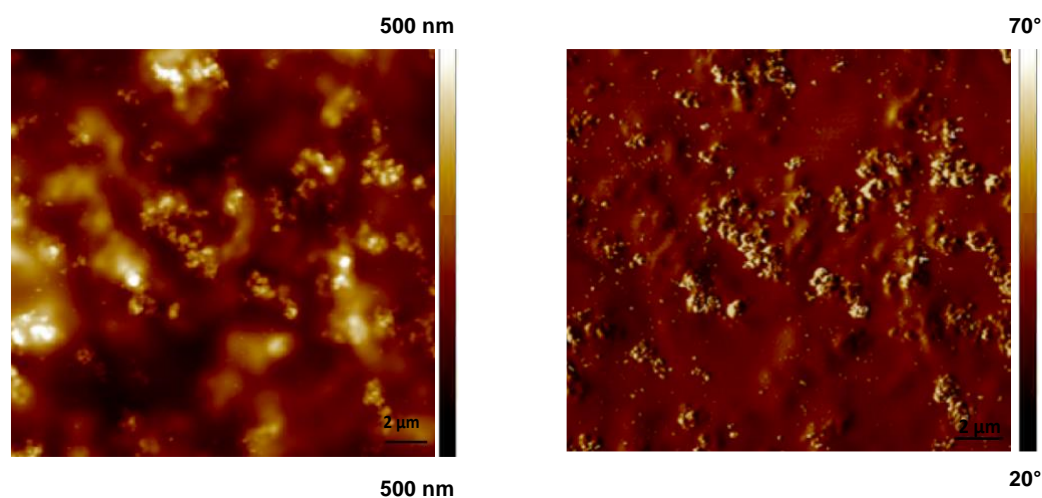
Figure 3-5. Tapping mode images of PI/Si_3N_4 untreated nanoparticles: (left) Topography, (right) Phase. scan size of 20 μm².

3.2.3 Influence of Si_3N_4 silane treatment on NPs dispersion

The affinity is an important parameter to homogeneously mix two kinds of materials. Nanoparticles aggregations lead to the deterioration of not only electrical properties, but also mechanical and thermal properties (section 2.2.3). Therefore, appropriate nanoparticles dispersion within the polymer needs to be achieved to ensure optimized properties for the resulting nanocomposite. In order to disperse inorganic nanoparticles into organic polymer matrices, the affinity between their contact surfaces should be taken into consideration. Generally, silane is commonly used to couple an organic polymer with an inorganic filler particle as described in the first chapter.

Figure 3-6 shows TEM images for the PI/Si_3N_4 untreated and silane-treated nanocomposite films at same weight content (1 wt.% initially dispersed in PAA). For untreated nanocomposite, we can observe a poor dispersion with the presence of large agglomerates (0.5 to 1 μm) into the material. On the contrary, the silane-treated one shows a strong diminution of the agglomerate maximum size (around 200 nm). Thus, from TEM-images it appears for the silane-treated nanocomposites that nanoparticles dispersion is not ideal but quite reasonable compared to untreated one.
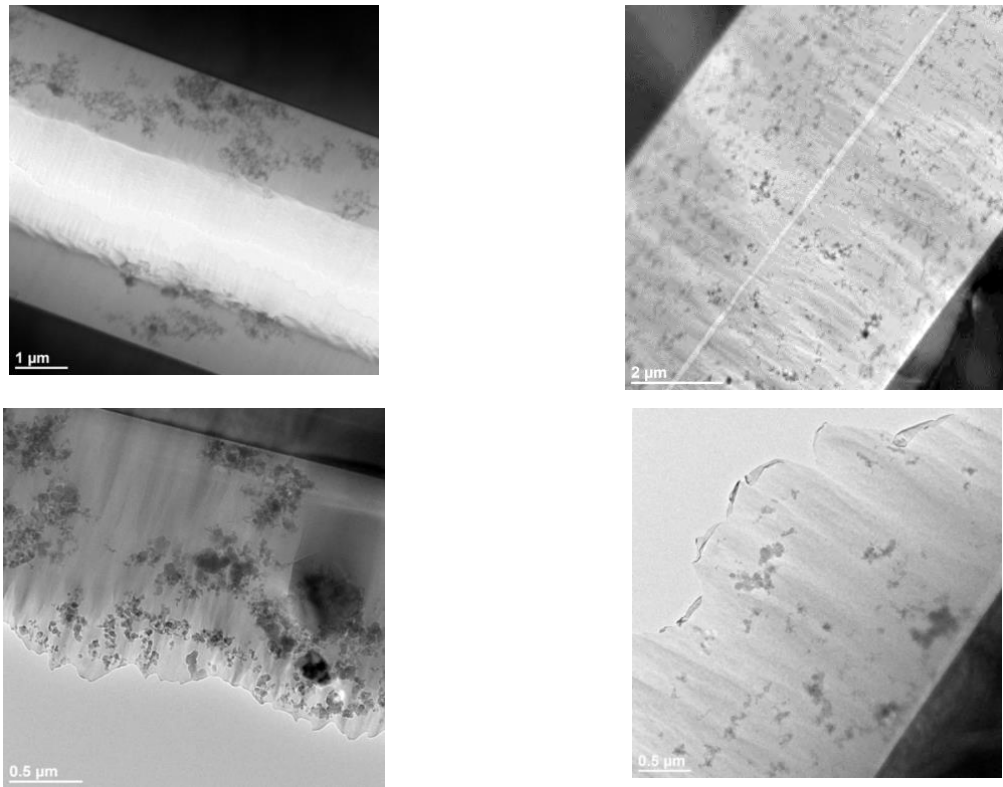
Figure 3-6. PI-nanocomposite TEM images for (left) untreated and (right) treated Si_3N_4 nanoparticles

Furthermore, the effect of a silane coupling agent treatment of the Si_3N_4 nanoparticles on the dispersion was investigated using AFM. According to figure 3-7, topography images for PI/Si_3N_4 nanocomposite with untreated nanoparticles for a 20 μm^2 scan area present rough surface and appear to be stacked and agglomerated compared to treated nanoparticles. This might be caused by the Van der Waals inter-particle attraction between primary particles themselves compared to treated nanoparticles modified by the silane coupling agent. It can be noticed that the particles dispersion within the polymer matrix is better for treated particles.

An average diameter of 550 nm and 250 nm for untreated and treated nanoparticles respectively are deduced from distribution diagrams. The detected diameter is larger than the predicted one for the individual Si_3N_4 nanoparticles (approximately 30 nm). This is the result of the presence of aggregates as well as a known phenomenon due to tip convolution effects. The change of roughness should be more visible using root mean squared values obtained from the topography images, i.e RMS= 91.2 nm and RMS = 21.7 nm for untreated and treated nanoparticles respectively.
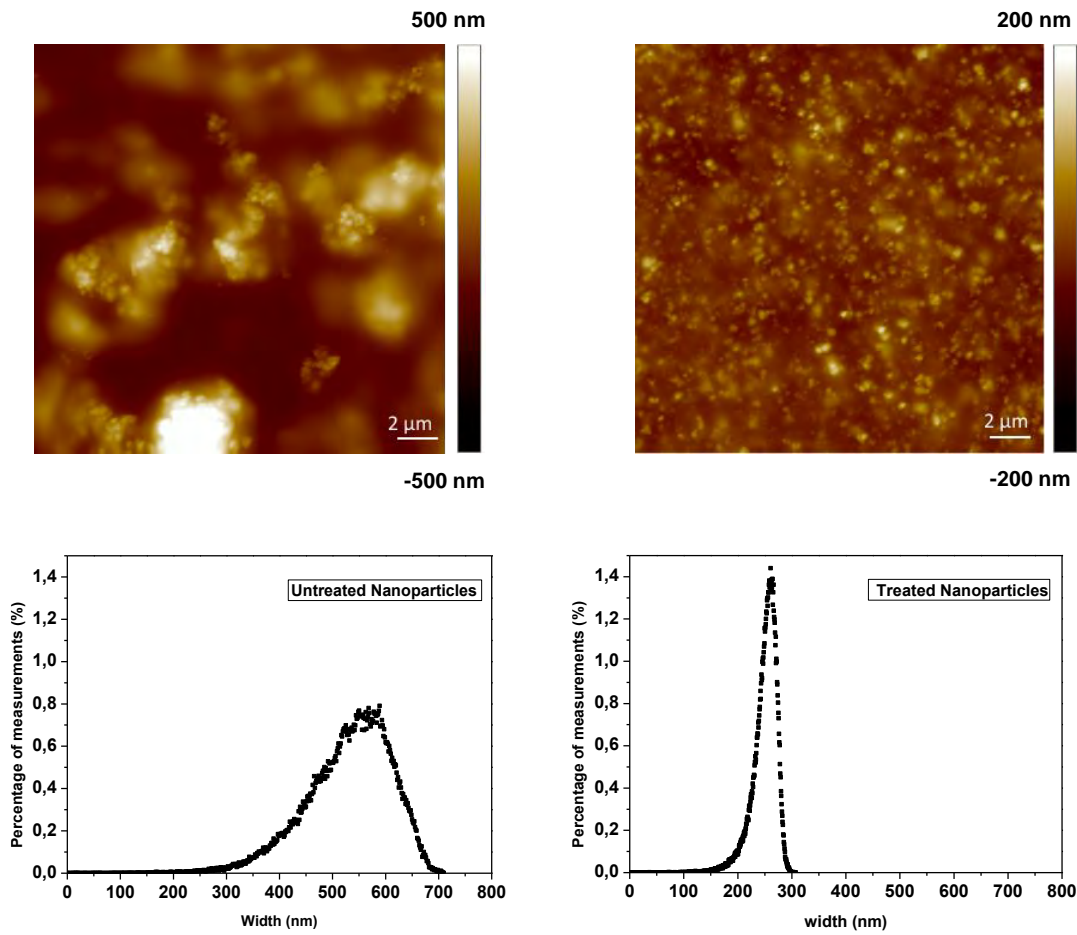
Figure 3-7. Height images for untreated (left) and treated (right) Si_3N_4 within PI and their corresponding distribution diagrams. Scan size of 20 μm^2.

3.3   Nanoscale mechanical characterization

Only qualitative results about the interphase presence are obtained from AFM tapping mode measurements. In order to have quantitative results of the interphase thickness, the PF QNM mode is used in this study allowing the measurement of mechanical local properties as explained in section 2.5.4. It is now possible to obtain quantitative properties mapping with high resolution (5 nm), including elastic modulus, deformation, adhesion and dissipation energy of the nanostructured materials surface.

3.3.1 Calibration

Following calibration results presented in section 2.5.4.5, measurements were performed first on polystyrene (PS) sample in order to establish the values for the working applied force (F_{tip}) related to a deformation between 1 and 3 nm and for the working tip radius (R). Young's modulus measurements after the calibration procedure are shown as histograms in figure 3-8 and a normal

distribution of Young's moduli for each material can be seen. It seems reasonable that a distribution of Young's moduli would be measured due to the effect of polymer chain orientation and semi-crystallinity at the nanoscale. Results show a young modulus value between 3 and 4 GPa for polystyrene (PS) sample and between 8 and 12 GPa for polyimide (PI) sample. These values are in agreement with the theoretical young modulus value of PS and PI sample used in this thesis.
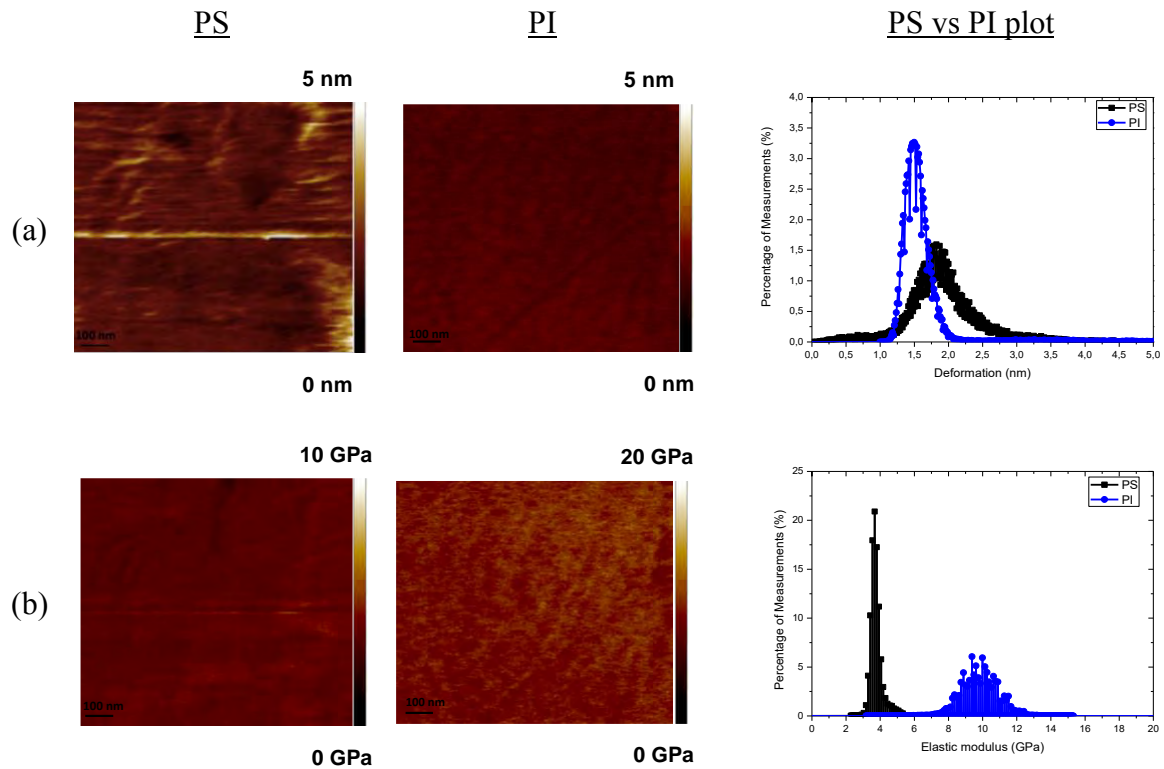
Figure 3-8. PS and PI (a) deformation and (b) young modulus with their corresponding normal distribution

3.3.2 Nanocomposite nanomechanical characterization

To analyze the properties of each phase and their variation with NP silane treatment, DMT modulus (elastic modulus) and deformation maps ($5\mu m^2$ scan size) with their corresponding distribution histograms are shown in figure 3-9. The deformation values vary from 1 to 3 nm for untreated nanocomposite and from 2 to 4 nm for silane-treated nanocomposite as seen in figure 3-9(a). In figure 3-9(b) for DMT modulus maps, the bright and dark dots show higher and lower modulus respectively, for the corresponding hard (nanoparticles or aggregate) and soft (polymer chain) phases. Modulus distribution histograms are also shown in figure 3-9(b). The mean modulus increases slightly from 10 GPa for treated NC to 13 GPa for untreated NC. Furthermore, the maximum modulus dramatically increases from 20 GPa to 50 GPa for untreated nanocomposite. It is clearly seen that the elastic modulus of the majority of the scanned surfaces (peak in the

distribution curve) is higher for untreated NC. The obtained results indicate that the presence of aggregates increase the mean nanocomposites modulus.
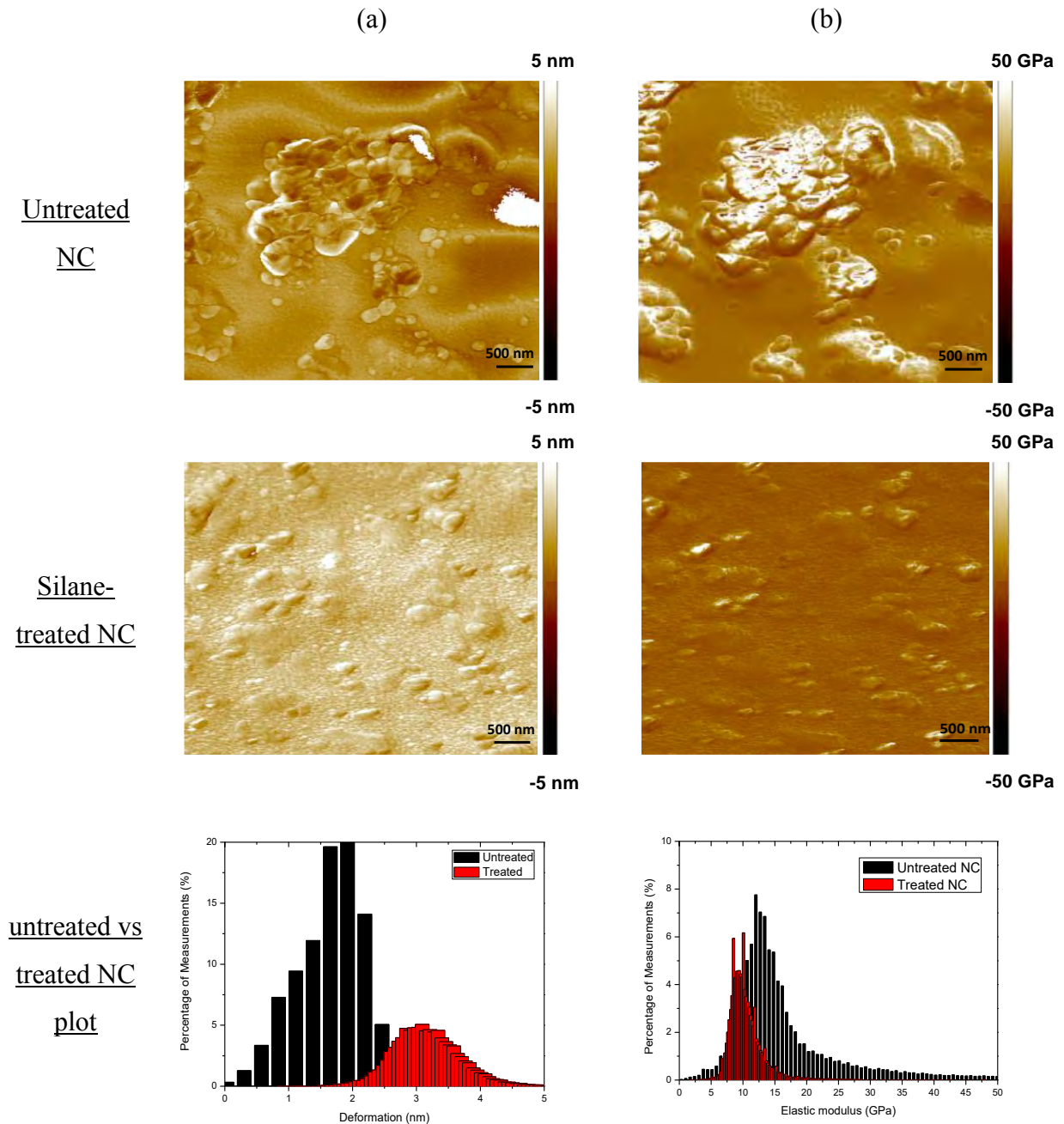
Figure 3-9. Untreated and treated NC (a) deformation and (b) young modulus with their corresponding normal distribution. Scan size of 5μm².

Such maps can be used to identify and characterize successively the composition and properties of multi-phase materials. A small variation of the deformation from 1 nm to 4 nm was obtained with an applied peak force equal to 600 nN to all nanocomposite samples and a working radius equal to 150 nm. The measurements were done using 384x384 digital pixel resolution, which corresponds to a pixel size of 13.02 nm and 5.2 nm for 5μm² and 2μm² image size respectively.

3.3.3 Interphase characterization

In order to measure the interphase thickness, the PF QNM mode is used. First, topography cartographies ($2\mu m^2$ scan size) allow us to understand the nanoparticles profile within the polyimide matrix. Height profile information permits identifying the immersed nanoparticle with a small height profile (around 10nm) in order to measure mechanical properties without any height effect.

3.3.3.1 Untreated nanoparticles

From topography image (figure 3-10(a)) and for different cross section measurements (figure 3-10(b)), the particles height is varying from 3 to 14 nm and width from 135 to 178 nm. The corresponding Young modulus (DMT cartography) is presented in figure 3-11(a).

Knowing that the interphase is a zone where the presence of a nanoparticle affects the matrix properties (chains rearrangement, chemical bonds, crystallinity degree…), it is probable that the mechanical properties of the matrix, the nanoparticle and the interphase would be different. Particularly, the change of the matrix mechanical properties around nanoparticles corresponds to the interphase zone and allow us to estimate its thickness.

For the chosen immersed particles, the elastic modulus profiles crossing both the matrix and the nanoparticle are shown in figure 3-11(b). These profiles show regions with a higher young modulus compared to the PI one. These regions could be interpreted as the interphase situated on both sides of a nanoparticle. Thus, the particles height and width are obtained from topography profiles and the interphase thickness and modulus from modulus profiles.

The corresponding results for untreated nanocomposites are presented in table 3-1. For the interphase thickness calculation, the width average of both peak from each side of a nanoparticle was used. Results show an interphase thickness value of about 32 nm for untreated NC.

Table 3-1. Untreated nanoparticles (width, height) and interphase (thickness and modulus) data

Particles	Width (nm)	Height (nm)	Interphase thickness (nm)	Interphase Modulus (GPa)
P1	183	13.9	34 ± 2	45 ±1
P2	164	10.07	33 ± 2	45 ± 6
P3	131	5.4	34 ± 3	22 ± 2
P4	94	3.7	31 ± 1	27 ± 3
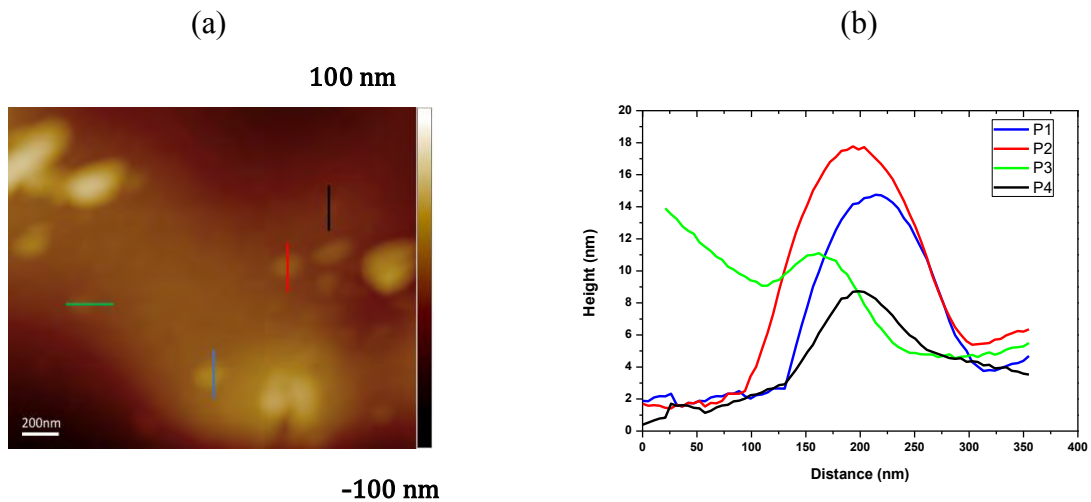
Figure 3-10. (a) AFM Topography image of untreated NC scan size of 2μm², (b) height particles profiles
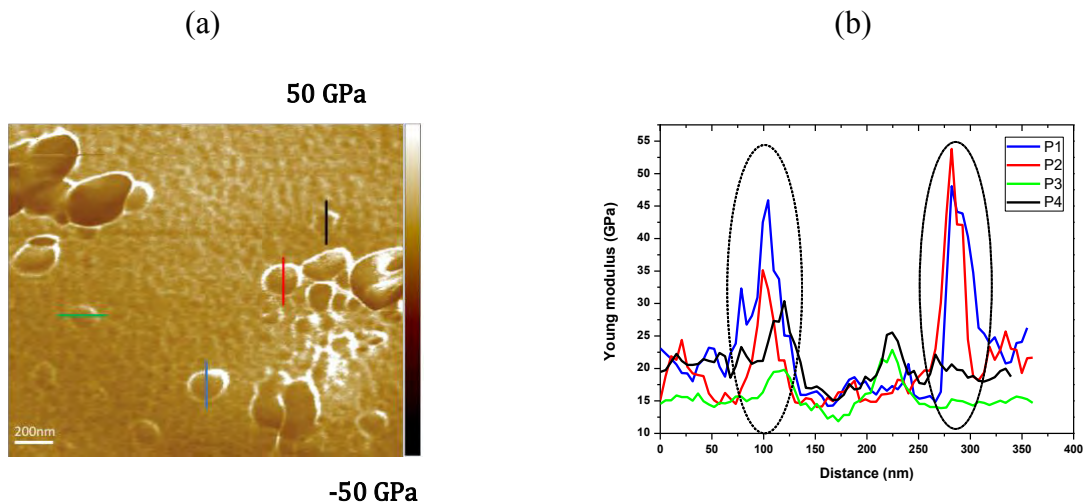
Figure 3-11. (a) The DMT cartography for untreated NC scan size of 2μm², (b) Young modulus profiles. The encircled zones correspond to the interphase.

3.3.3.2 Treated nanoparticles

As for the untreated nanocomposites, the same cross section profiles are taken across height and DMT modulus images for treated nanoparticles (figure. 3-12 and 3-13). Nanoparticles show a height varying between 3 and 22 nm and a width varying between 100 and 150 nm. The elastic modulus profile is drawn according to each colored line, which crosses both the matrix and the nanoparticle in the case of immersed particles.

Regions with higher Young modulus than PI one are also observed around nanoparticles and represent the interphase. Particles diameter and height as well as interphase modulus and thickness for treated NP are presented in table 3-2. Results show an interphase thickness value of about 48 nm for treated NC. This higher value of interphase compared to untreated particles shows that the silane surface treatment increases the interaction between the particle and the matrix, i.e larger

interphase. However, the presence of the silane coupling agent in the interphase zone on the surface of the nanoparticle leads to a lower value of the interphase Young modulus.

(a) (b)
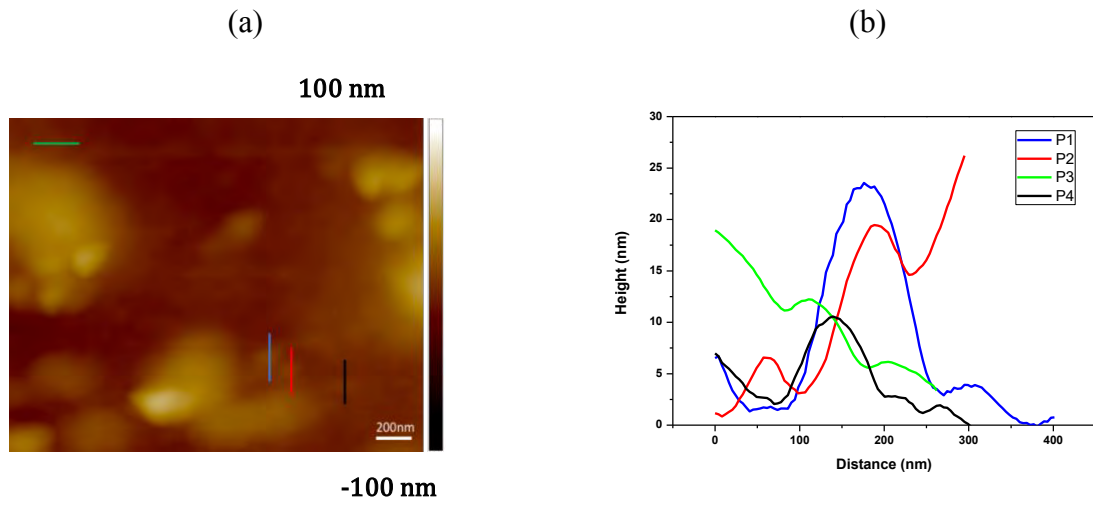
Figure 3-12. (a) AFM Topography image of treated NC scan size of 2μm², (b) height particles profiles

(a) (b)
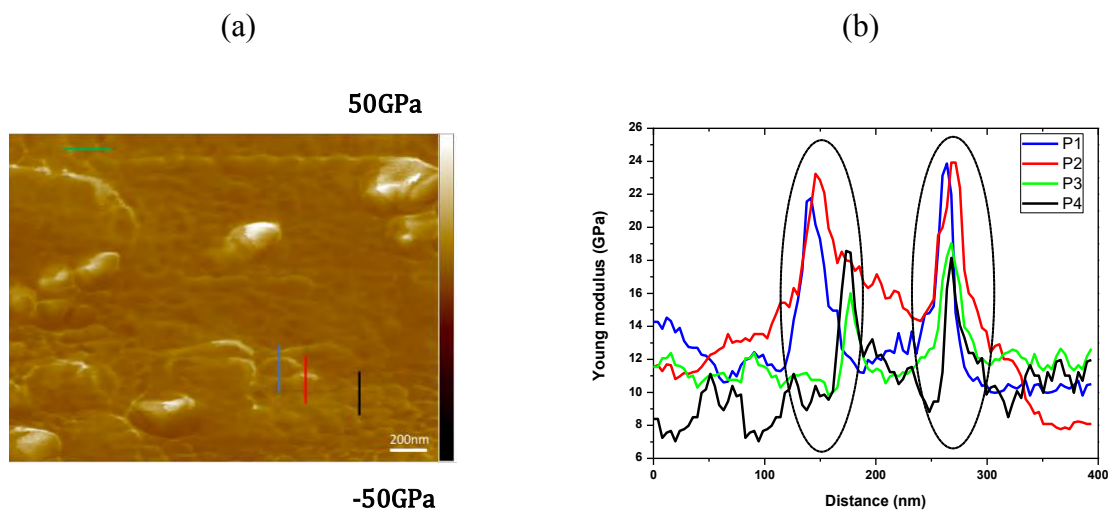
Figure 3-13. (a) The DMT cartography for treated NC scan size of 2μm², (b) Young modulus profiles. The encircled zones correspond to the interphase.

Table 3-2. Treated nanoparticles (width, height) and interphase (thickness and modulus)

Particles	Width (nm)	Height (nm)	Interphase thickness (nm)	Interphase Modulus (GPa)
P1	150	22.8	54 ± 3	23 ± 2
P2	125	15.3	52 ± 4	24 ± 1
P3	107	2.5	41 ± 2	18 ± 1
P4	100	6.5	41 ± 2	18 ± 1

3.4   Discussion on nanomechanical characterization

To complete previous DMT modulus results, the corresponding deformation images are presented in figure 3-14. Both untreated and treated nanocomposites deformation cartographies are presented. Results show an increase of the deformation on the top of nanoparticles (especially the protuberant ones identified from topography images) and aggregates. The reason behind may be attributed to the free horizontal movements (shear flow) of polymer chains on the top of a nanoparticle (or aggregate) during the force application. Moreover, a deformation decrease around nanoparticles, where the interphase is supposed to be localized, for both protuberant and immersed nanoparticles is observed. It can be deduced that this region is stiffer than the matrix and the top of nanoparticles. One can also notice that the interphase stiffness is lower for treated NC compared to untreated one. This is in agreement with the lower Young modulus value of treated particles interphases compared to untreated ones.

To sum it up, the Peak Force QNM AFM mode was revealed to be a powerful tool to access to very local mechanical properties. First, it is interesting to notice that the neat Polyimide (PI) DMT mean modulus obtained by PF-QNM (i.e. 10 GPa) is close to the PI theoretical Young's Modulus (i.e. 8.5 GPa). Moreover, the interphase young modulus around nanoparticles appears with higher modulus and lower deformation for both treated and untreated nanocomposites compared to the matrix. With a small height profile taken into consideration, the interphase thickness was measured quantitatively. Results have shown a region with a 32 nm thickness where the polymer chains are supposed to be aligned to the nanoparticles. It was also shown that the particles treatment using silane coupling agent increases the interphase thickness to 48 nm. Clearly, the addition of silane tends to make the interphase thicker compared to untreated one. The lower interphase DMT modulus in the treated NC, indicates that the phases may be locally miscible because of the silane molecules which are probably located in this zone.
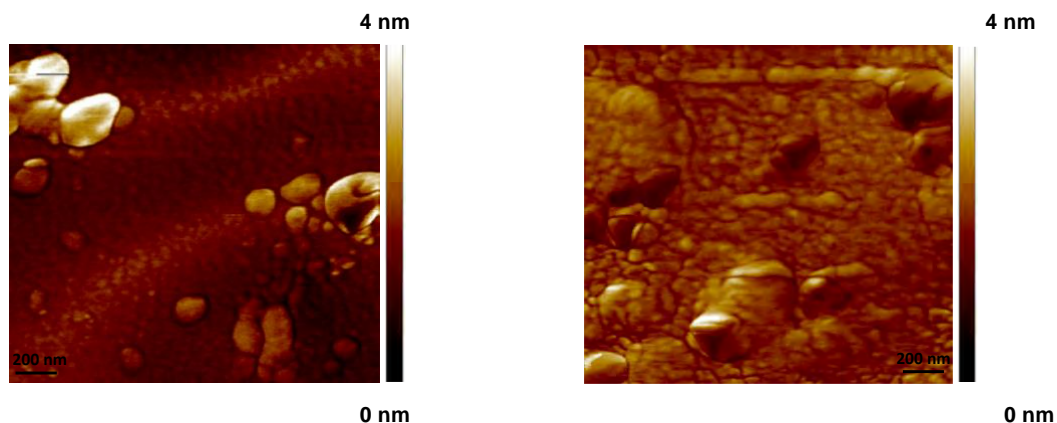
Figure 3-14. Deformation maps for (right)untreated and (left) treated nanocomposite. Scan size of 2µm²

Finally, it could be interesting to highlight the nanoparticles location possibilities on the surface during the different measurements as shown in figure 3-15. Cases 1 and 2 present untreated nanoparticles with thin interphase and cases 3 and 4 show the treated particles with a thicker interphase. Moreover, the immersed particles can show a bump (cases 1 and 3) or an exposed bump (cases 2 and 4).
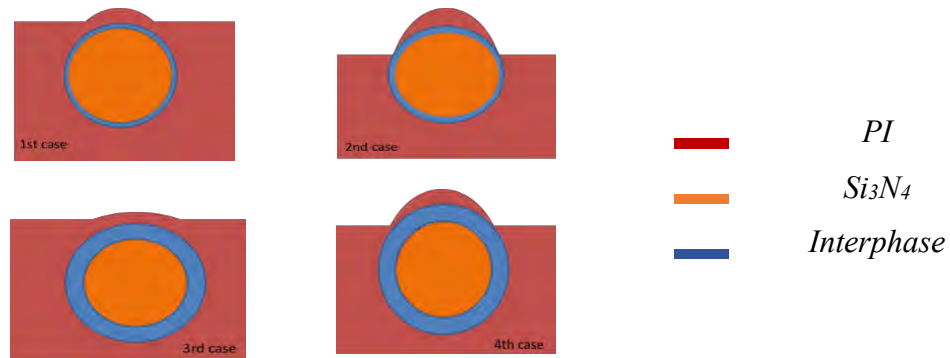
Figure 3-15. Si3N4 nanoparticles profile within the PI matrix for untreated (1st,2nd case) and treated (3rd ,4th case) nanocomposite interphase

3.5 **Nanoscale dielectric characterization**

Figure 3-16 summarizes EFM measurements performed on nanocomposite layer with and without silane treatment on Si_3N_4 NPs. Topography map emphasizes isolated NP close to the surface for samples without (figure 3-16(a)) and with (figure 3-16(d)) treatment. Following the methodology described in part 2.5.5, the frequency shift parameter $a_{\Delta f}$ obtained using equation 2-21 is presented in figure 3-16(b) and (e). The permittivity map (figure 3-16(c) and (f)) is deduced from $a_{\Delta f}$ using COMSOL model, which considers the nanocomposite layer as a homogeneous material. Results emphasize that, whatever surface treatment is, the relative dielectric permittivity (i.e. frequency shift parameter $a_{\Delta f}$) is lower on the NP. Indeed, as summarize in table 3-3, relative dielectric permittivity is around 2.9-3 over nanoparticle and around 3.35 on the matrix, which is close to the theoretical value for PI. Moreover, dielectric permittivity over silane-treated NP is lower than the one over non-treated NP.
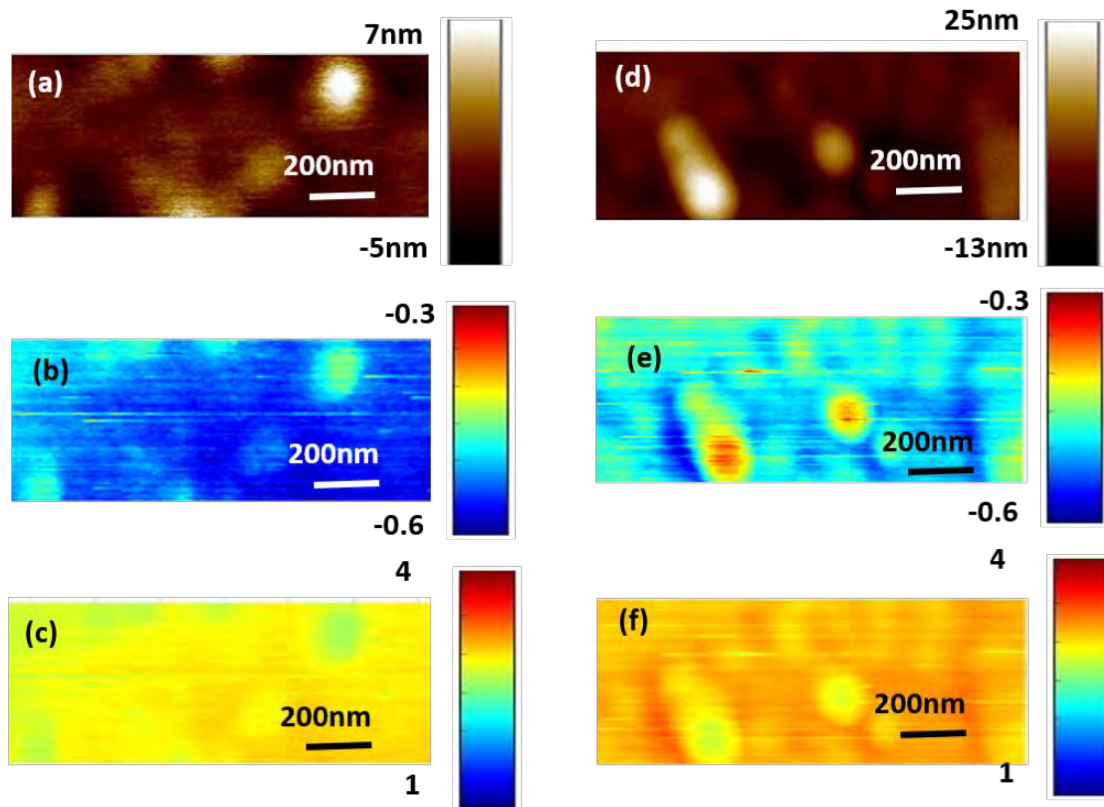
Figure 3-16. Nanocomposite without (a-c) and with (d-f) silane treatment for Si3N4 nanoparticles. (a, d) Surface topography, (b, e) frequency shift parameter aΔf and (c, f) relative permittivity

To explain the decrease of the apparent dielectric permittivity over Si_3N_4 NP, a Finite Element Modeling (FEM) representing the real sample geometry is proposed. This is composed of a PI matrix and a 20 nm width Si_3N_4 NP with a dielectric permittivity respectively equal to 3.5 and 7.5. The resulting electric field distribution is represented on figure 3-17(a). Figure 3-17(b) shows the apparent dielectric permittivity evolution as a function of the distance between the NP and the nanocomposite surface. Results emphasize that dielectric permittivity increases when NP is close to the surface. Consequently, the only presence of Si_3N_4 NP close to the surface fails to explain apparent dielectric permittivity decreasing over NP. This kind of conclusion was already obtained by Peng et al on TiO_2/LDPE nanocomposite [110]. The main hypothesis to explain this phenomenon is related to the interphase.

Table 3-3. Relative dielectric permittivity for matrix and over nanoparticle as a function of the NP treatment

	No treatment	Silane treatment
Matrix	3.35	3.35
Over NPs	3	2.9
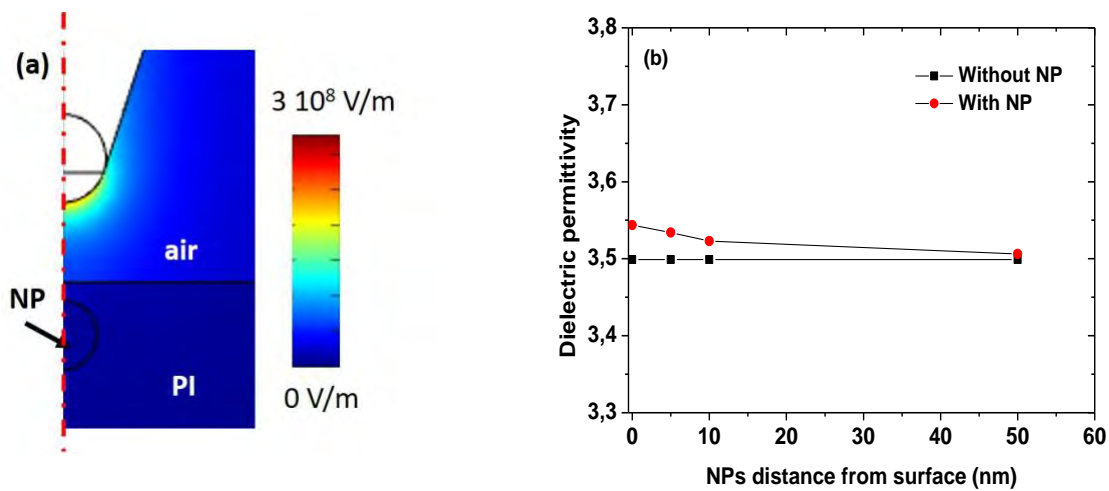
Figure 3-17. (a) Electric field computed for 10V applied on AFM tip and a Si3N4 nanoparticles localized at 5nm from the surface. (b) Evolution of dielectric permittivity computed for different distances between NP and the surface. NP presents a radius of 20nm and sample is 2.3μm-thick which corresponds to nanocomposite without treatment

Consequently, a more complex FEM taking into account the presence of the interphase is proposed. As previously, this is composed of a PI matrix and a 20nm-width Si_3N_4 NP with dielectric permittivity respectively equal to 3.5 and 7.5. In addition, an interphase with tuned thickness and dielectric permittivity is taken into consideration (figure 3-18(a)). Figure 3-18(b) represents the evolution of the computed frequency shift parameter $a_{\Delta f}$ as a function of the interphase dielectric permittivity for different interphase thicknesses. Results highlight that all curves intercept at $a_{\Delta f}$ =-0.53Hz/V² and ε_r=3.5 which correspond to the PI matrix parameters. When the interphase permittivity is lower than the matrix one, the interphase thickness increase induces a frequency shift parameter increase as well. Whereas when the interphase permittivity is higher than the matrix one, the interphase thickness increase induces a frequency shift parameter decrease. Moreover, when the interphase thickness increases, a characteristic behavior tending to a homogeneous material one is observed. We can identify that an interphase with a lower permittivity than the matrix one is needed to explain experimental results presented on figure 3-16. In the following, interphase properties (thickness and dielectric permittivity) will be determined using this model.
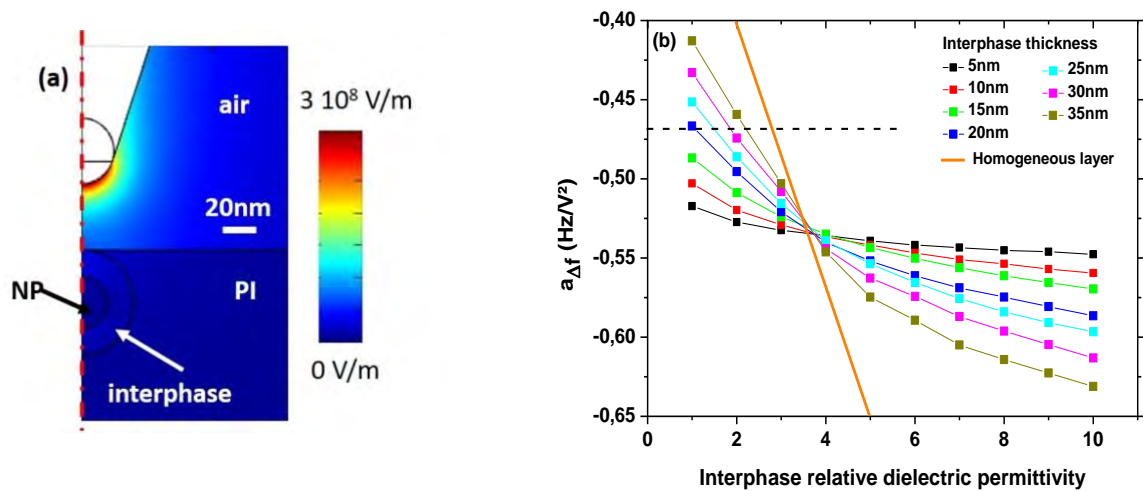
Figure 3-18. (a) Electric field computed for 10V applied on AFM tip and a 20nm-NP with interphase (thickness of 20nm and dielectric permittivity of 2) and sample thickness of 2.3µm-thick which corresponds to nanocomposite without treatment. (b) aΔf evolution as function of interphase dielectric permittivity for different interphase thickness

3.6 Interphase morphological and dielectric properties

Figure 3-19(a) compares topography and frequency shift parameter $a_{\Delta f}$ profiles over NPs without treatment. A frequency shift parameter $a_{\Delta f}$ is equal to -0.53 Hz/V² over the matrix and -0.47Hz/V² over NP. According to figure 3-18(b), a lot of permittivity/thickness couples are possible to describe the interphase. Indeed, the interphase thickness needs to be higher than 20nm and its permittivity should be between 1 and 3. Consequently, with only EFM results it is only possible to conclude that the interphase permittivity is lower than the matrix one.

On the other hand, Figure 3-19(b) compares topography and frequency shift parameter $a_{\Delta f}$ profiles over a NP with silane treatment. This nanoparticle has been chosen because it has the same topographical shape as NP without treatment (figure 3-19(a)), which permits considering that, in a first approximation, NPs are located quite at the same distance from the surface. A frequency shift parameter $a_{\Delta f}$ is equal to -0.47 Hz/V² over the matrix and -0.39Hz/V² over NP.
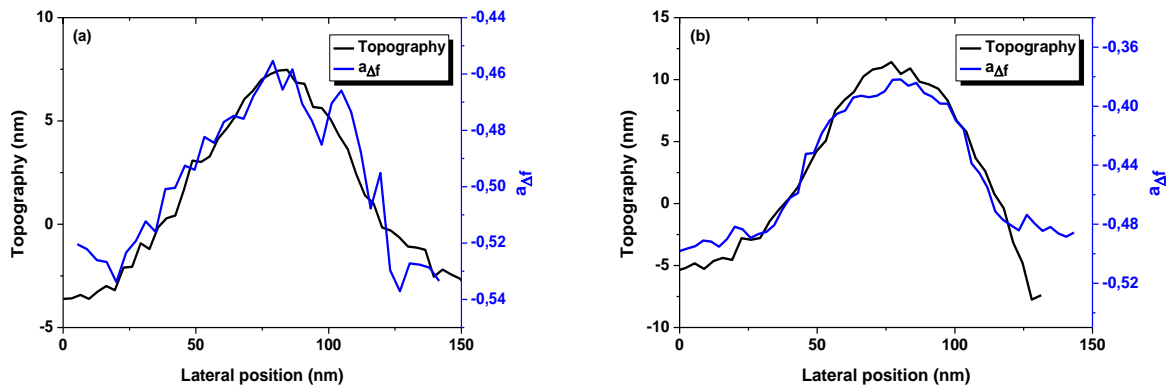
Figure 3-19. (a) Comparison of topography and aΔf profile over Si3N4 nanoparticle (a) without and (b) with silane treatment

Consequently, to characterize the interphase properties at nanoscale a two steps processes is proposed (figure 3-20). (i) The first step consists in mechanical properties characterization using PF-QNM to determine interphase lateral width w. (ii) Interphase relative dielectric permittivity was determined modifying the 2D-axisymetric FEM model to introduce the Si3N4 nanoparticle (diameter 10-20nm, ε_r=7.5) and interphase (thickness w, ε_r = unknown).

According to PF-QNM measurements, the interphase thickness is between 25nm and 35nm for untreated NC, which represents for 20nm and 10nm-width nanoparticle an interphase dielectric permittivity between 1 and 2 (figure 3-18(b)). Following the same method, interphase dielectric permittivity was determined as a function of interphase thickness (45nm and 55nm) for silane-treated NP. Concerning sample without NPs treatment an interphase relative dielectric permittivity of 1.8±0.4 and 1.5±0.4 was found considering 10nm-width or 20nm-width nanoparticles respectively. Concerning sample with treated NPs an interphase relative dielectric permittivity of 2±0.5 and 1.8±0.5 was found considering 10nm-width or 20nm-width nanoparticles respectively. This interphase relative permittivity decrease was previously observed but never quantified at the nanoscale, combined with an interphase thickness experimental determination. Results, summarized in table 3-4, show that the relative permittivity of the interphase is lower than the matrix one and remains quite the same, around 1.8, for treated and untreated samples.
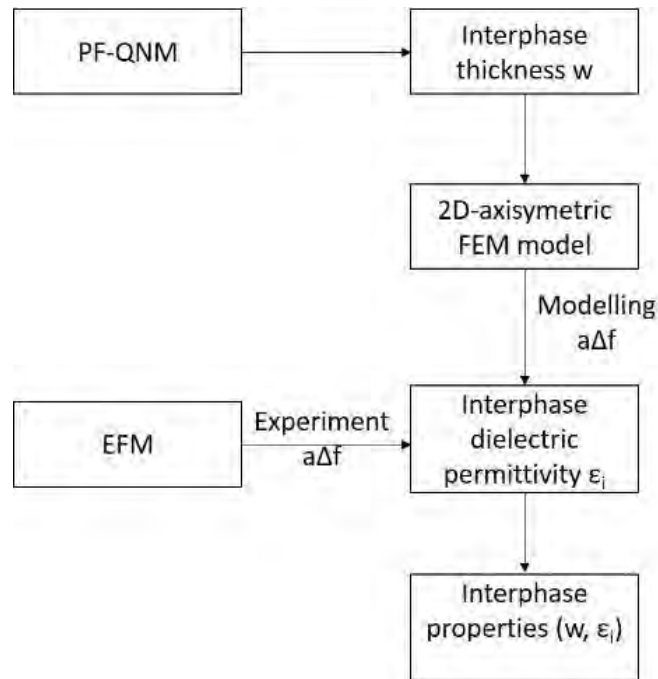
Figure 3-20.Interphase characterization processes

Table 3-4. Interphase thickness and relative permittivity as a function of NP treatment

NP treatment	NP radius	Interphase thickness	Interphase relative permittivity
Untreated	10nm	30nm ±2nm	1.8±0.4
	20nm		1.5 ±0.5
Treated	10nm	48nm±6nm	2±0.5
	20nm		1.8±0.5

These results are in agreement with previous studies. Indeed, the interphase thickness was estimated around 20nm using the multi-core model [60] and an interphase dielectric permittivity (1.6) lower than LDPE matrix one (around 2.2) was pointed out by Peng [110].

3.7 Interphase Phenomenological Model Proposal

In this study, the performed nanoscale characterization provides an opportunity for a fundamental comprehension of the interphase area based on quantitive values of its mechanical and dielectric properties. Results have shown that the interphase presents higher young modulus and lower relative dielectric permittivity than the PI matrix. This can be explained by a better polymer chain organization in the interphase around the nanoparticle. Indeed, the nanoparticle plays the role of a nucleation agent around which self-organized matrix chains appear. This organized or crystallized

zone have a higher Young modulus than the amorphous matrix. Moreover, the low chain mobility in this zone due to chain organization or to the chain movement restriction by the nanoparticle leads to a lower dielectric permittivity.

These observations are similar for untreated and treated nanoparticles with a difference concerning the interphase thickness. However, one can notice that the interphase relative dielectric permittivity is quite the same for both nanocomposites. So, nanoparticles treatment seems to influence mainly spatial extension of the interphase without modifying significantly its dielectric properties. Figure 3-21 illustrates our phenomenological model to describe the interphase for untreated and treated particles.
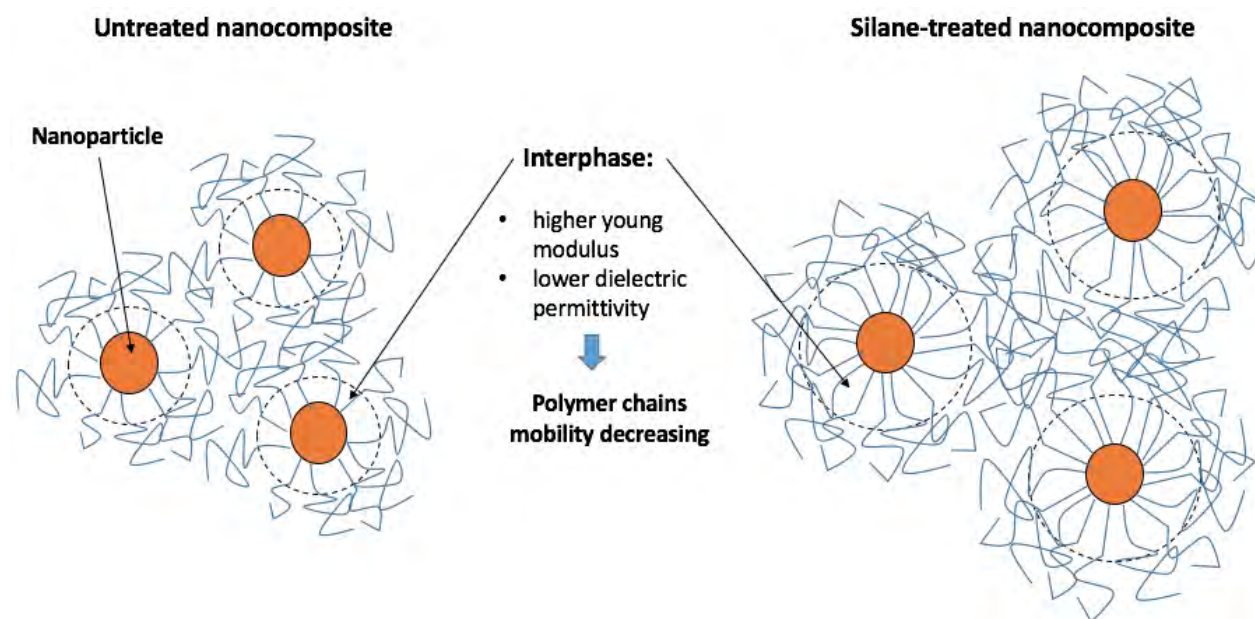
Figure 3-21. Illustration of the proposal model for nanoparticles/polymer chain interphase zone for untreated (left) and treated nanocomposites (right)

3.8 Conclusion

In this chapter, the PF QNM and EFM AFM modes were applied to directly measure the mechanical and dielectric local properties of PI/Si_3N_4 nanocomposites with a particular focus on the interphase region over untreated and silane treated particles surface. A particular attention was given to the study of nanoparticles dispersion within the host matrix in both cases using TEM and AFM measurements. Results show a better dispersion of treated Si_3N_4 within the PI matrix compared to untreated particles.

This work has presented in detail a new approach to quantitatively measure the interphase thickness and properties. Experimental results indicate that the interphase area have a higher Young modulus and a lower permittivity than the matrix. Thus, the interphase represents an organized polymer chain area around the nanoparticle where the chain mobility is restricted. Moreover, the particle surface silane treatment has an effect on increasing the interphase thickness (from 32nm to 48 nm) but do not influence its dielectric properties. Finally, a phenomenological model was given in order to describe the interphase behavior within nanocomposite materials. Understanding the interphase area properties at the nanoscale may be the key process to explain the improvements observed for nanocomposites electrical properties at the macroscopic scale. In the following chapter, macroscopic electrical properties, i.e dielectric spectroscopy and breakdown strength, will be studied in order to correlate the macroscopic nanocomposite behavior to its local interphase properties.

4. The interphase effect on macroscopic properties

Content

4.1. Introduction

This chapter aims to present the Si_3N_4 nanoparticles effect on macroscopic electrical properties of the polyimide matrix (PI), particularly at high temperatures (>200°C). For this reason, dielectric spectroscopy and breakdown strength measurements are performed on unfilled PI, untreated and silane-treated PI/Si_3N_4 nanocomposites. After eliminating the humidity effect on the macroscopic electrical properties, the influence of the presence as well as the treatment of Si_3N_4 nanoparticles on the final properties is analyzed. This analysis will be correlated to previous results obtained from nanoscale characterization (cf. chapter 3). Thus, both nano and macro scale characterizations will allow us to better understand the behavior of electrical insulation nanocomposite materials.

4.2. Dielectric spectroscopy results

4.2.1. Humidity effect on dielectric properties

For dielectric spectroscopy measurements, two temperature cycles were applied to the sample. A heating cycle (from -150°C to 350 °C) followed by a cooling cycle (from 350°C to -150°C). At low temperatures a difference between the two cycles is observed in term of the temperature dependence on permittivity (ε') and loss factor ($\tan\delta$) for different frequencies (0.1 Hz to 100 kHz). Indeed, as shown in figure 4-1(a, b), a peak, noted γ, is observed during the heating cycle. This peak appears around -80°C at 0.1Hz and shifts to high temperatures when the frequency increases. However, this peak disappears for the cooling cycle as shown in figure 4-1(c, d). This result can be related to the hydrophilic nature of PI. In fact, the PI matrix is known to absorb water from the environment. Therefore, its molecular chains could interact with water molecules. For this reason, it was suggested that this γ peak was due to carbonyl motions, which were plasticized by the localized water (i.e. creation of bonds between H_2O and C=O) [171]. Consequently, the peak related to moisture disappears after heating up to 350°C. Thus, the macromolecular structure recovers its rigidity, which is accompanied by a decrease in permittivity and dielectric losses at low temperatures.

(a)   (b)

(c)   (d)
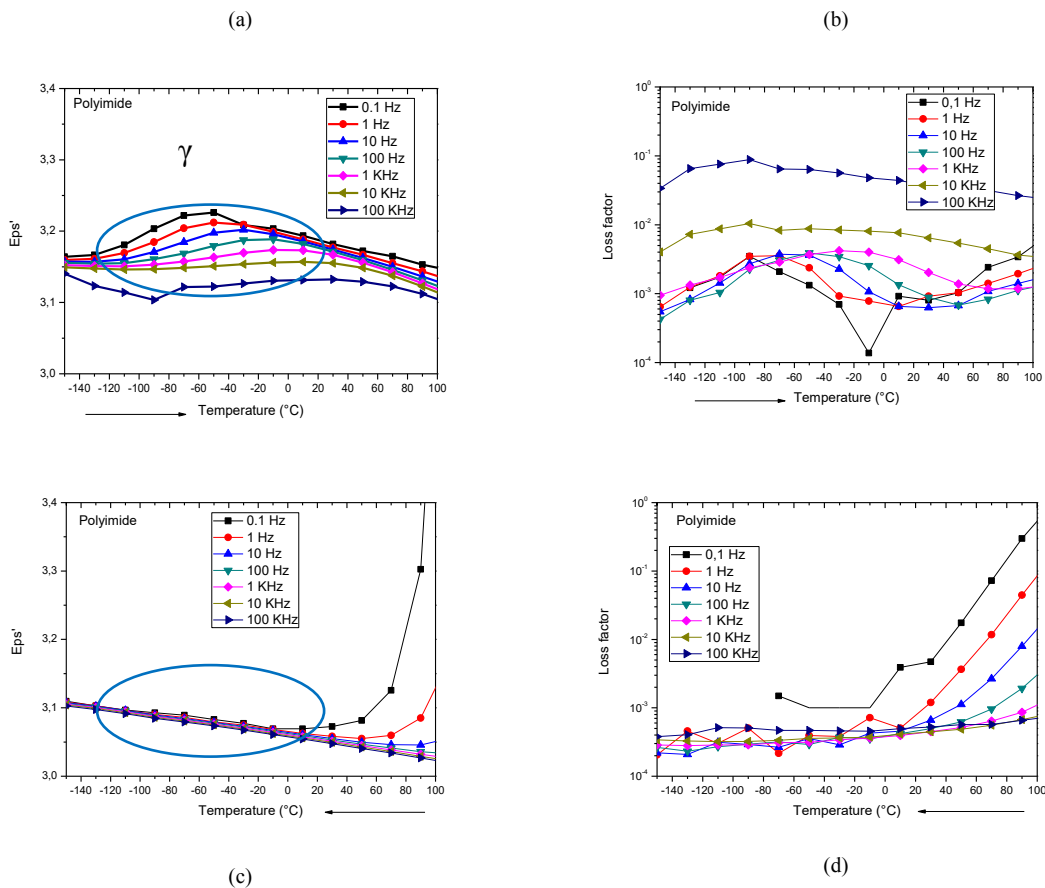
Figure 4-1.Polyimide real permittivity (a-c) and loss factor(b-d) between -150 and 100°C under the heating (a-b) and cooling (c-d) temperature cycles for frequencies from 0.1 Hz to 100 kHz

The same behavior is observed in the case of untreated and silane-treated nanocomposites. Moreover, an investigation on the impact of thermal heating and water absorption on the dielectric response of all samples was realized at 30°C. The obtained results of the relative permittivity and loss factor as a function of frequency are shown in figure 4-2(a,b). As it can be seen, the real permittivity (ε') and loss factor become lower after the heating treatment (AH), an effect which is depicted by the arrows. The heating treatment decreases the value of the permittivity (see figure 4-2-a) due to the evaporation of water molecules which have a much higher value of permittivity (around 80) than PI and Si_3N_4. In addition, nanoparticles absorb water from the environment due to their hydrophilic nature. Consequently, their surface tends to attract moisture which increases the hydroxyl group in the nanocomposite. This effect is more visible in the case of untreated NC as it can be seen from figure 4-2-b. Indeed, a high loss factor for untreated NC is observed at low frequencies. It can be attributed to the DC and ionic conductivity which is linked to the water uptake. Additionally, after silane treatment, there is a strong reduction in the loss factor. Therefore, it seems that there is a decrease in the amount of moisture absorbed in the films when the nanoparticles have been treated on the surface. Furthermore, the dielectric permittivity significantly decreases for all samples as well after heat treatment. The same

110

behavior was already mentioned by Kochetov *et. al* on the impact of postcuring and water absorption on dielectric response of epoxy-based composites filled with MgO nanoparticles [172].
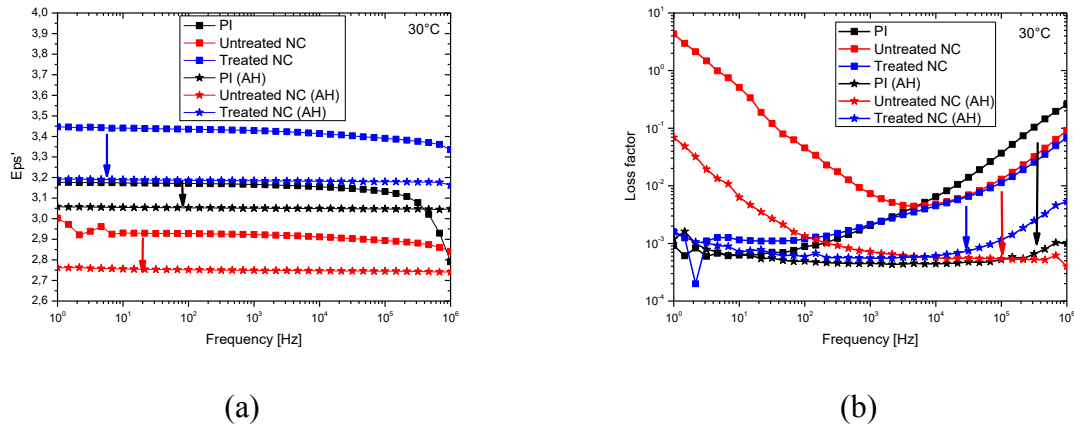
Figure 4-2. Real permittivity (a) and loss factor (b) as a function of frequency at 30°C

4.2.2. Dielectric properties at low temperatures (<150°C): what about the interphase effect?

In order to eliminate the water effect and for a better understanding of the dielectrics properties modification related to the interphase zone, a heating treatment was applied to PI and nanocomposites samples for all the following results.

4.2.2.1. Permittivity behavior

Figure 4-3 shows that over a wide range of temperatures, between -150°C and 150°C, the values of permittivity for unfilled PI, untreated and silane-treated nanocomposites remain constant for the different frequencies between 10 Hz and 1 MHz. Moreover, when particles are untreated, the NC has a lower permittivity. This phenomenon is intriguing and interesting since the addition of fillers with a higher permittivity (7.5 for silicon nitride NP) to a polymer is supposed to cause an increase in the effective permittivity of the nanocomposite, mostly due to the influence of filler permittivity. Similar observations have been earlier stated. The corresponding literature has reported that a restriction in the polymer chains mobility occurs mainly due to the interaction process between nanoparticle surfaces and polymer chains [173][29].

In the case of untreated NC, the effective permittivity decrease is probably due to the interaction between fillers and polymer chains. Thin immobile nanolayers can be formed in the interphase area, where the mobility of PI chains is restricted as already shown from nanoscale characterization. In this case, the influence of Si_3N_4 nanoparticles permittivity which is higher than that of polyimide will not be very effective. Nevertheless, with filler silane functionalization,

there is an increase in the nanocomposite permittivity values compared to unfilled and untreated one. The relative permittivity of treated nanocomposite increases because of the influence of the silane molecules permittivity (located at the nanoparticles surface). Indeed, the silane permittivity value measured at 25 °C is between 9.48 and 8.61 at frequencies from 1 kHz to 1 MHz as presented in figure 4-4. Moreover, one can notice that the permittivity values start to increase for unfilled and untreated NC above 100°C at low frequency (10 Hz).
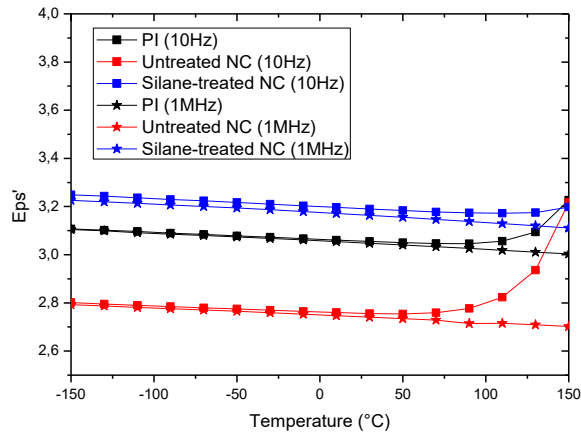
Figure 4-3. The temperature effect on the real part of permittivity for neat polyimide, untreated and silane-treated nanocomposites
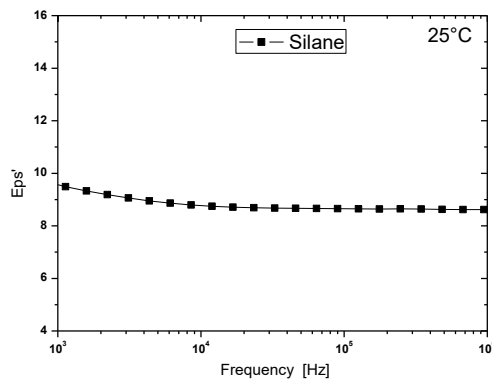
Figure 4-4. The frequency dependence of the real part of permittivity for the silane coupling agent at 25°C

In order to quantitatively compare the different permittivity values, it was decided to consider permittivities at -150°C for unfilled PI, untreated and silane-treated nanocomposite, where the effect of temperature has little influence as shown in figure 4-5. Indeed, permittivity decreases from 3.1 for the unfilled polyimide to 2.8 in the case of untreated nanocomposite. This can be attributed to the low permittivity of the interphase compared to polyimide as already confirmed by EFM measurements. The same behavior was found by Singha *et al.* [174] [175], where lowering of permittivity is attributed to a minimum influence of filler permittivity and a strong

polymer-nanoparticle interaction. However, an increase in the permittivity value from 2.8 to 3.25 with nanoparticles surface treatment was observed over all the frequency and temperature ranges.
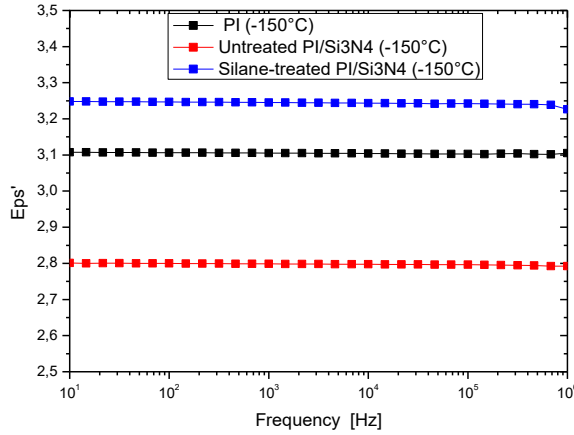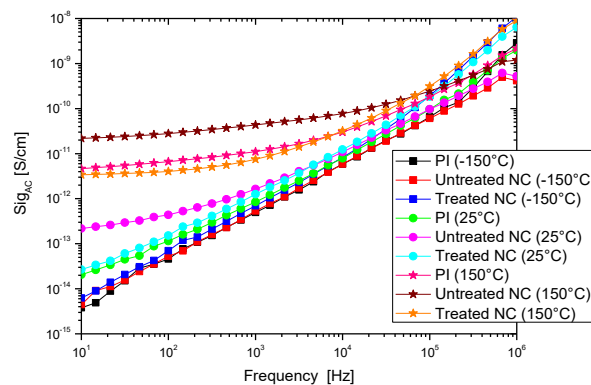

Figure 4-5. The frequency dependence of the real part of permittivity for neat polyimide, untreated and silane-treated nanocomposites at -150 °C

The use of the mixing law for permittivity values interpretation:

In order to explain the obtained permittivity values in both untreated and silane-treated NC, we propose to use the basic form of the mixing law, where the matrix, the nanoparticle and the interphase are taken into consideration. In fact, Daily.et al [176] have proposed a three-dimensional theoretical model permitting the calculation of the effective permittivity taking into account the particle, the matrix and the interphase permittivities and volume fractions (equation 4-1). In equation 4-2, the same model was adapted in order to take into consideration the presence of silane as well in the case of treated nanoparticles:

Untreated NC relative permittivity	ε_{eff} =2.8	$\varepsilon_{eff} = \varepsilon_i \emptyset_i + \varepsilon_p \emptyset_p + (1 - \emptyset_i - \emptyset_p)\varepsilon_m$ (4-1)
Silane-treated NC relative permittivity	ε_{eff}=3.25	$\varepsilon_{eff} = \varepsilon_i \emptyset_i + \varepsilon_p \emptyset_p + \varepsilon_s \emptyset_s + (1 - \emptyset_i - \emptyset_p - \emptyset_s)\varepsilon_m$ (4-2)

where ε_{eff} is the effective nanocomposite permittivity measured experimentally at -150°C, ε_i, ε_p, ε_s and ε_m are the interphase, nanoparticles, silane and matrix permittivity respectively. $\emptyset_i$, $\emptyset_p$ and $\emptyset_s$ are the interphase, nanoparticles and silane volume fraction respectively.

First, the volume fraction of each individual phase is analytically calculated from weight fraction using the following relation:

$$\%\emptyset_p = \frac{\frac{\%wt\ P}{\rho_P}}{\frac{\%wt\ P}{\rho_P} + \frac{\%wt\ M}{\rho_M} + \frac{\%wt\ S}{\rho_S}}$$
(4-3)

where P, M and S are particle, matrix and silane respectively, $\%\emptyset$ and $\%wt$ are the volume and the weight fraction for each phase, the corresponding values are summarized in Table 4.1.

Table 4-1. Density, weight and volume fraction of each phase for untreated and silane-treated nanocomposite

	density (g/cm^3)	weight (g)	Untreated NC		Silane-treated NC	
			%wt	%∅	%wt	%∅
PI	1.48	10	99.001	99.449	90.090	86.277
Si$_3$N$_4$ NP	2.6755	0.1	0.999	0.551	0.901	0.477
Silane	0.964	1	-	-	9.009	13.246

The volume fraction of polyimide, Si$_3$N$_4$ nanoparticles and silane phase was calculated from the weight fraction assuming that all silane is incorporated in the case of silane-treated NC. In addition, the following equation (4-4) proposed by Todd and Shi [177] allows the calculation of interphase volume fraction from NP radius and interphase thickness:

$$\emptyset_i = \frac{4\pi\emptyset_{NP}}{3r^3}((r+R)^3 - r^3)$$
(4-4)

Table 4-2 summarizes the obtained results for interphase volume fraction obtained by local measurements (Tapping and PFQNM modes). Here also we suppose that no overlap occurs between the adjacent particle's interphase due to the low filler content (filler loading <1%).

Table 4-2. Interphase volume fraction obtained from PFQNM mode results for untreated and silane-treated nanocomposite

	Untreated NC	Silane-treated NC
%∅ (NP)	0.551	0.477
NP radius (nm)	200	100
Interphase thickness (nm)	30	48
%∅i (Interphase)	**3.50**	**40.53**

Results indicate that the silane treatment increases the volume fraction of the interphase from 3.5% to 40.53%. This result can be explained by the better dispersion and the improvement of the coupling between the nanoparticles surface and the polyimide molecular chains.

Finally, the volume fractions and the experimentally obtained permittivities for the Si_3N_4 nanoparticles, unfilled polyimide, silane and the interphase (measured by EFM nanoscale measurements) (Table 4-3) are used into the mixing law.

Table 4-3. Permittivity and volume fraction for each phase

	Measured ε	Calculated %Ø (for each phase)	
		Untreated NC	Silane-treated NC
Interphase	2	3.50	40.53
PI	3.1	95.949	45,75
Si_3N_4 NP	7.5	0.551	0.477
Silane	8.6		13.246

Results show higher values (3.08 for untreated NC and 3.56 for silane-treated NC) compared to measured ones (2.8 for untreated NC and 3.25 for silane-treated NC). In addition, if we do not consider the interphase presence, the difference with the measured value is bigger (3.12 for untreated NC and 3.84 for silane-treated NC).

Consequently, we have considered different interphase volume fractions in order to obtain the right value measured experimentally (Table 4-4). Results show that the interphase volume fraction value is higher than 27% and 55 % for untreated and silane-treated NC respectively.

Table 4-4. Interphase volume fraction vs effective Permittivity

Untreated NC			Silane-treated NC		
%Ø (Interphase)	%Ø (PI)	Effective permittivity	%Ø (Interphase)	%Ø (PI)	Effective permittivity
3	96.44	3.09	40	46.2	3.40
6	93.44	3.05	43	43.2	3.37
9	90.44	3.02	46	40.2	3.34
12	87.44	2.99	49	37.2	3.31
15	84.44	2.95	52	34.2	3.27
18	81.44	2.92	**55**	**31.2**	**3.24**
21	78.44	2.89	58	28.2	3.21
24	75.44	2.86	61	25.2	3.17
27	**72.44**	**2.82**	64	22.2	3.14
30	69.44	2.79	76	10.2	3.01

4.2.2.2. Tan Delta and AC conductivity characteristics

Figure 4-6 shows the variation of the samples loss factor (tanδ) over the range of frequencies between 10 Hz and 1 MHz at -150°C and 25°C.

For -150°C temperature measurements, we can notice that dielectric losses of all samples are similar at low frequencies. However, the tanδ value for silane-treated nanocomposite increases at high frequencies (>10 kHz). This is to do with the high value of the silane loss factor at these frequencies.

Besides, at 25°C and for low frequencies, tanδ values are higher for all samples compared to the one measured at -150°C, particularly for the untreated Si_3N_4 nanocomposite. Indeed, at 10 Hz the loss factor values are tanδ = $1.5×10^{-3}$ and tanδ = $1.2×10^{-2}$ for treated and untreated NC respectively. This is likely a result of interfacial polarization at low frequencies and a higher temperature. This effect was also discussed by Dang *et al.* who have explained their similar results by an increase of interface and dipole polarizations at low frequency [178] [179]. For the composite made with silane-treated nanoparticles, the loss factor below 10 kHz has reduced values, indicating that the presence of the silane layer around nanoparticles modifies the charge distribution at the interface. Thus, interfacial effects are decreased and silane acts as an insulating loss barrier that reduces conducting charge carriers [180]. Moreover, the decrease of tanδ for the silane-treated nanocomposite may be attributed mostly to the better particles dispersion [181].
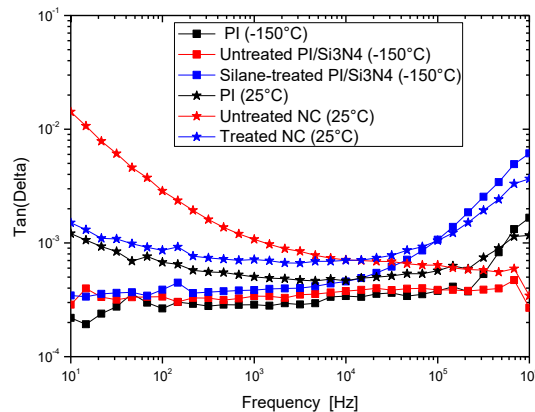
Figure 4-6. The frequency dependence of the loss factor for neat polyimide, untreated and silane-treated nanocomposites at -150 °C and 25 °C

In addition, figure 4-7 shows the frequency dependence of the AC conductivity (σ_{AC}) for different samples at different temperatures -150°C, 25°C and 150°C. At high frequencies, the AC conductivity linearly changes with the frequency. At low frequencies, it becomes frequency independent and a permanent value appears which corresponds to the DC (or quasi-static) conductivity following the equation:

116

$$\sigma_{AC} = \omega \varepsilon_0 \varepsilon^{"}(\omega) = \sigma_{DC} + A\omega^n \qquad (4\text{-}4)$$

where A is a temperature parameter and 0.6<n<1 is the exponent of the power law.

Furthermore, it can be seen that as the temperature increases the amplitude of the DC conductivity also increases and extends towards higher frequencies. These two observations imply two notions. The first is that the DC conductivity in dielectric materials is a thermally activated parameter which follows an Arrhenius behavior. The second reflects the fact that at higher temperatures the charge carriers can move more easily in the conduction band: the time for establishing a steady state becomes shorter and, consequently, the conduction phenomenon is observed at higher frequencies.

Figure 4-7. The frequency dependence of the AC conductivity for neat polyimide, untreated and silane-treated nanocomposites at -150 °C, 25 °C and 150°C

4.2.3. Dielectric properties at high temperatures (>150°C): What about the interphase effect?

Figure 4-9(a,d) shows the dielectric response of the neat PI as a function of temperature between -150 and 350°C for different isofrequencies between 0.1 Hz and 1 MHz. We can clearly observe the presence of two relaxation phenomena above 150°C. They are both characterized by a significant increase in the dielectric permittivity associated to an increase in dielectric losses within the PI sample. These relaxations were previously observed by Sombel *et al.* [182] where they were called ρ and ρ* respectively in order of appearance when the temperature increases. They were attributed to the dispersion of mobile charge carriers at low frequencies, followed by their accumulation at the volume/electrode interfaces. The accumulated carriers then form a gigantic dipole of gigantic size (macroscopic dipole presented in figure 4.8) which induces a strong variation in permittivity and dielectric losses. These same relaxation phenomena, also called space charge relaxations [1], were observed in our sample and represent the electrodes polarization (EP) due to space charges accumulation. Indeed, when thermally activated, positive (or negative) charge carriers (electron, holes or ions) can drift to the negative (or positive)

polarized electrode in order to build up a space charge at the sample/electrode interface. Moreover, the electrical conduction in PI films is influenced by macroscopic migration of H^+ ions (coming from unreacted PAA [183]) to the electrode/sample interfaces. This conduction is superposed to the second relaxation at low frequencies and high temperature.

In addition, PI/Si_3N_4 untreated and silane treated nanocomposites show the same relaxation phenomena (figure 4-9-b,c,e,f). However, a decrease in the permittivity amplitude is observed, especially in the case of silane-treated NC. It should also be noted that the conduction, which is manifested by a permittivity increase, appears from 250°C and at low frequencies for only unfilled polyimide and untreated NC.
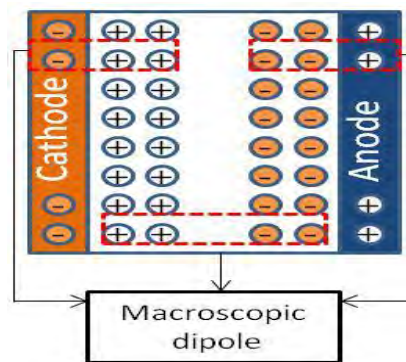
Figure 4-8. Schematic representation of the macroscopic dipole
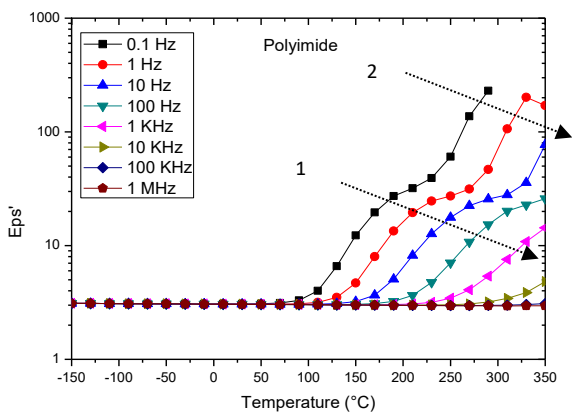
(a)
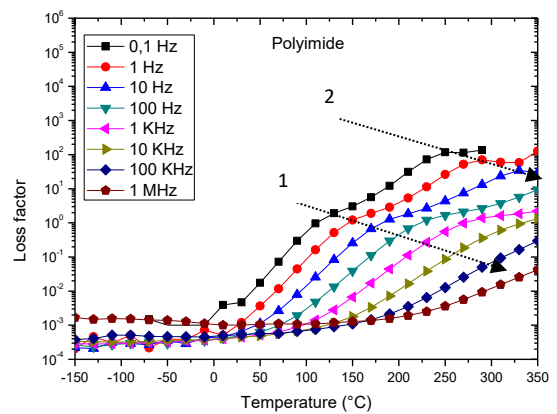
(d)
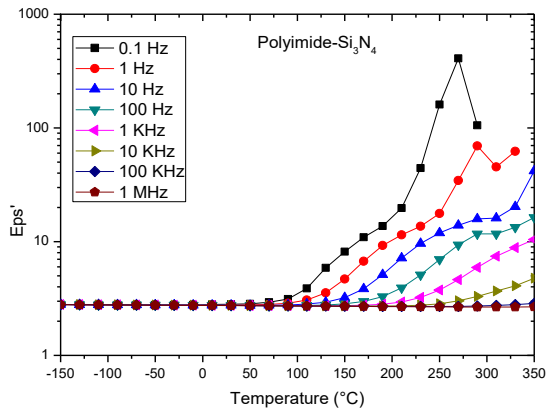
(b)
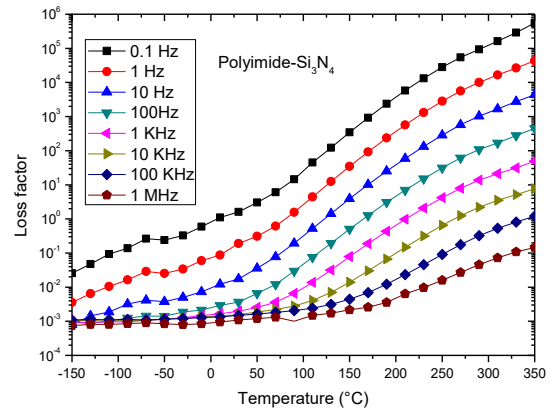
(e)
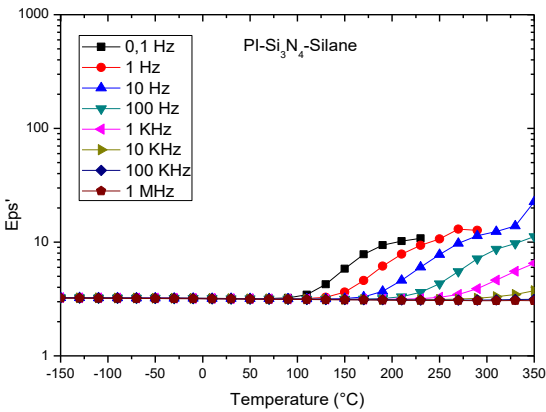
(c)
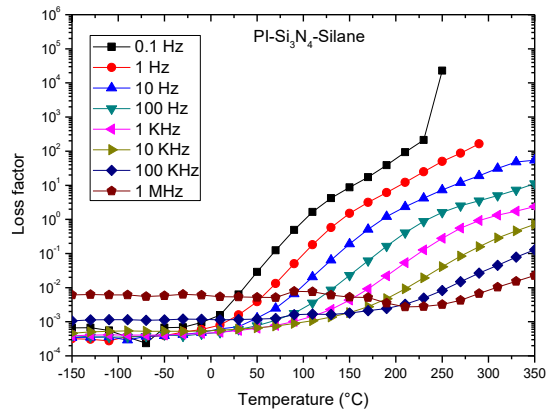
(f)

Figure 4-9. PI, PI-Si$_3$N$_4$ untreated and silane-treated real permittivity (a-c) and loss factor (d-f) between -150 and 350°C for isofrequencies from 0.1 Hz to 1 MHz

In the following, the nanoparticles presence effect, and thus the interphases presence effect, on the matrix dielectric behavior at high temperatures is analyzed. Figure 4-10 represents a comparison of the temperature dependence (from 150°C to 350°C) on the dielectric permittivity of neat PI, untreated and silane treated PI/Si$_3$N$_4$ at 10 Hz and 1 MHz.

It can be seen that EP or space charge relaxation appears between 200°C and 300°C at 10 Hz for all samples. However, this relaxation is less significant for nanocomposite samples compared to neat PI, especially for the one with treated particles.
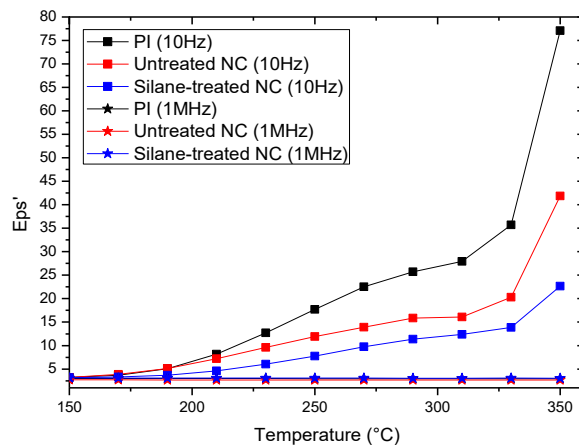
Figure 4-10. The high temperature effect on the real part of permittivity for neat polyimide and its nanocomposites

An insight into the way the interphase dimensions and chemistry at high temperature affect the dielectric properties may be obtained by examining the variation of the relative permittivity as a function of frequency at fixed temperature of 200°C, 250°C, 300°C and 350°C. Figure 4-11 shows the effect of temperature on the permittivity values difference between PI, untreated and treated nanocomposites. This difference is more and more significant when temperature increases as shown in table 4-5.

Tableau 4-5. Real permittivity values at high temperatures (>200°C)

	200°C	250°C	300°C	350°C
unfilled PI	8	18	27	77
untreated nanocomposite	7	12	16	42
silane treated nanocomposite	5	8	12	22
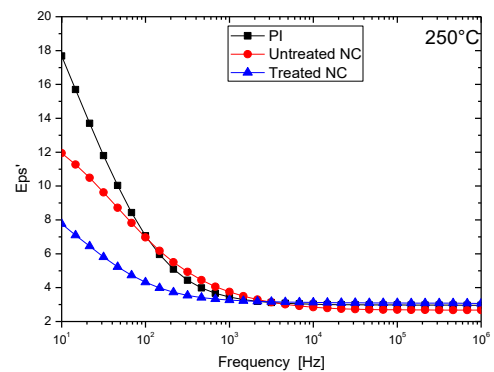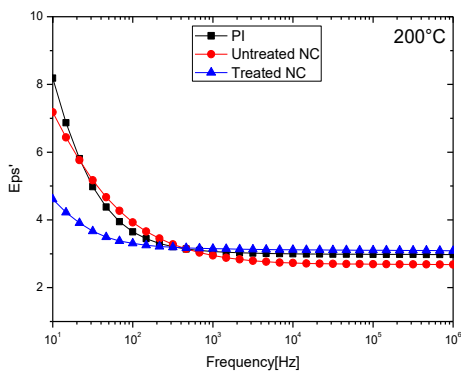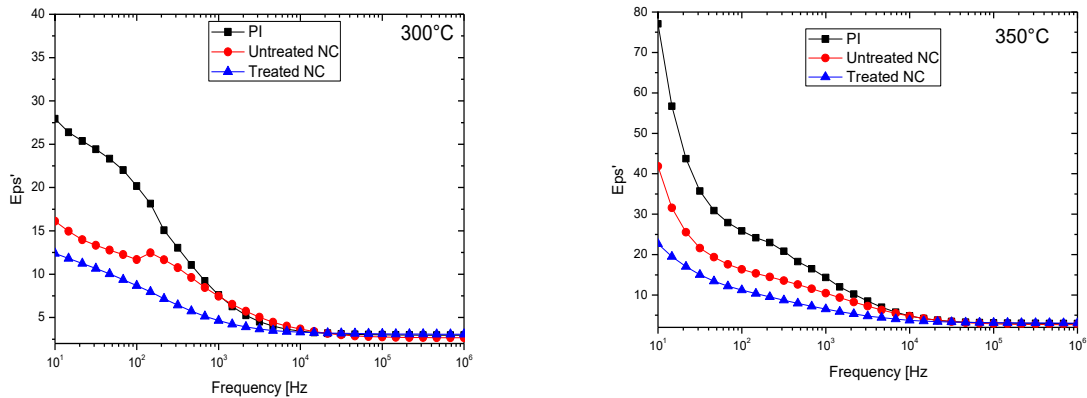
Figure 4-11. Electrode polarization (EP) evolution as a function of frequency

One can notice from the above results that at high temperatures, where ion charge carriers are highly mobile, the presence of nanoparticles seems to decrease this mobility responsible of the degradation of the PI dielectric properties. It is thus envisaged that Si_3N_4 nanoparticles may strongly limit ionic movements (but not completely inhibit them) by increasing their mean free path in the PI. These carriers are therefore in lower density in the electrodes vicinity (reduction of the variation of ε') which makes it possible to limit the collapse of metal/sample energy barriers and thus to reduce injection phenomena. Indeed, the interphase region around nanoparticles is a region where H^+ ions are blocked and could less reach the sample/electrode interface. Moreover, the silane coupling agent acts as a more efficient grafting link between the PI macromolecular chains and the Si_3N_4 improving the interphase volume where the ion charge mobility is reduced. Such improvement after the NP surface functionalization by a silane-treatment is related to the interphase and its thickness.

Moreover, figure 4-12 shows the evolution of the AC conductivity (σ_{AC}) as a function of the frequency for the three samples at (a) 200 °C and (b) 350 °C. AC conductivity values increase with temperature. Indeed, it is a thermally activated parameter. The silane-treated nanocomposite AC conductivity remains lower than both untreated and unfilled PI ones.
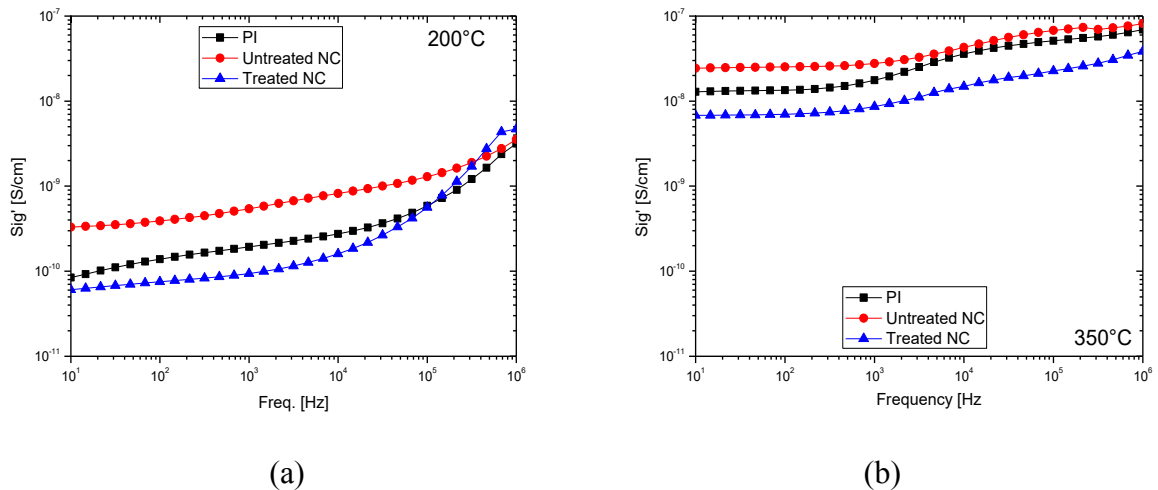
Figure 4-12. AC condictivity of unfilled PI, untreated and silane treated PI/Si_3N_4 at (a) 200°C and (b) 350°C

4.3. Breakdown strength results

4.3.1. Temperature effect on breakdown strength

In the following, the Weibull statistical law (cf. section 2.4.2) on a population of more than10 samples was applied in order to extract the value of the breakdown field (breakdown strength) for each material at each test condition. Breakdown fields injected into the law are calculated from the breakdown voltage divided by the thickness of each sample. Figure 4.13 shows the Weibull plots of PI, untreated and treated nanocomposites at 25°C, 100°C, 200°C and 250°C. The solid lines correspond to the different linear regressions performed on the data with a 90% confidence interval. The cumulative probability (y-axis) at 63.2% (which means that 63.2% of samples would break for this value) gives the breakdown field value (x-axis). In addition, the shape parameter β (slope of the linear plot) presents the results dispersion. When β<<1, results show a high dispersion, when β>>1 results show a low dispersion and β=1 presents a results random dispersion.

For each sample, we can notice from the obtained results that the breakdown field decreases when the temperature increases. This can be related to dielectric spectroscopy results where it was shown that at high temperatures, conduction phenomena and dielectric losses are significant. Indeed, the charge carriers mobility, especially for H^+ ions highly present in the PI matrix [183][184], is increased at high temperatures and under the effect of the field. When all (positive/negative) ions reach the electrode (cathode/anode), a field intensification takes place and the phenomenon of electronic injection intensifies in the sample to give rise to a current. This current may accelerate the sample electrical breakdown. In addition, the shape parameter β for all samples has a big value which indicates that a small breakdown results distribution is at play.

(a)

(b)

(c)
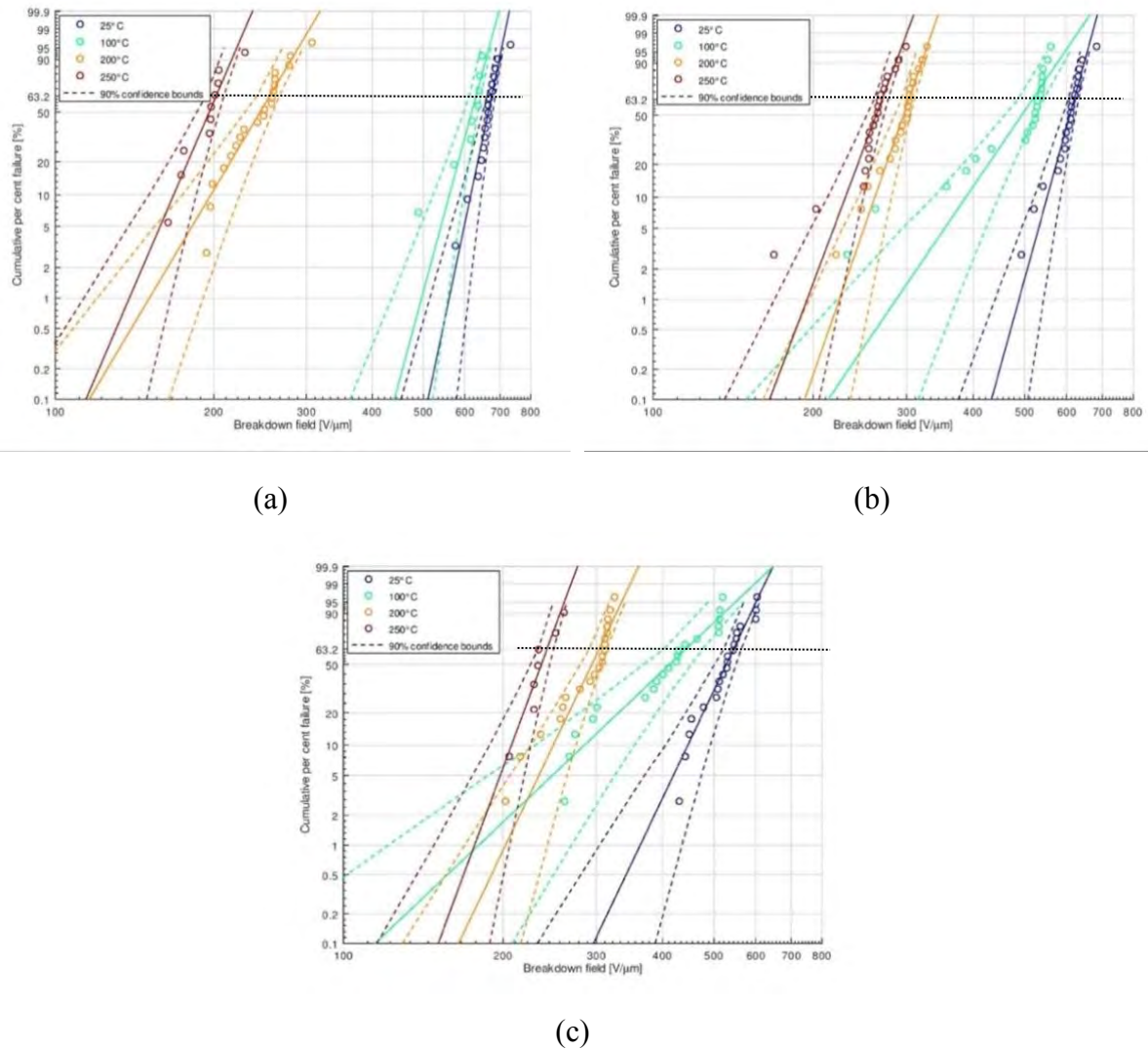
Figure 4-13. Weibull plots for the dielectric breakdown strength determination of (a) neat PI, (b) untreated and (c) silane-treated PI/Si$_3$N$_4$ without drying at different temperature

In the following, a comparison between neat PI and nanocomposites breakdown results is made. Since, results have different behavior at low (<150°C) and high (>150°C) temperatures, it was decided to separate the results presentation depending on the temperature range.

4.3.2. Samples breakdown strength at low temperatures (<150°C)

The Weibull breakdown results comparing untreated, silane-treated nanocomposite and their corresponding neat material are reported in Table 4-6. Under 25 °C (room temperature), breakdown results reveal that the addition of 1 wt% Si$_3$N$_4$ nanoparticles to neat PI generates a slightly breakdown field decrease (about -4.8%), from 674 V/μm to 641 V/μm. Interestingly, a higher decrease is observed for the silane-treated samples (about -20%), to 536 V/μm. The same behavior is seen when samples are heated to 100°C, the breakdown results under this temperature decrease from 630 V/μm to 532 V/μm (about -15.5 %) and 409 V/μm (about -35%) for PI,

untreated and silane-treated nanocomposites respectively. Moreover, a decrease in the dispersion factor (β) was observed for treated particles NC showing a higher dispersion of breakdown results.

Table 4-6. Weibull parameters for 3 samples measured at 25°C and 100°C

		Alpha (Weibull scale parameter V/µm)	Beta (Weibull shape parameter)
F_{br} at 25°C	PI	674	24 .84
	Untreated PI /Si$_3$N$_4$	641	17 .23
	Silane-treated PI /Si$_3$N$_4$	536	10 .81
F_{br} at 100°C	PI	630	19.34
	Untreated PI /Si$_3$N$_4$	532	6.04
	Silane-treated PI /Si$_3$N$_4$	409	4.08

The dielectric strength decreases for nanocomposites compared to unfilled PI could be related to the fact that fillers in polymers create defects and also introduces additional charge carriers in the volume of the material and thereby reduce the dielectric strength in nanocomposites. Moreover, the higher decrease observed for silane-treated NC is probably related to the interphase zone, which is the only phase different between untreated and treated NC. Indeed, a good dispersion was observed (AFM and TEM images) for treated particles with high interphase thickness and volume fraction.

Finally, in order to analyze the breakdown print on the material, all samples were observed with a digital microscope. For temperatures of 25°C and 100°C, all the breakdown zones look similar as shown in figure 4-14. Failures occurred in samples volume. It can be seen that all samples show a "dark" area that would correspond to the evaporation of the gold electrode at failure. In all cases, a black carbonized zone appears where the failure has occurred.

	Neat PI without drying	Untreated PI-Si$_3$N$_4$ without drying	Silane treated PI-Si$_3$N$_4$ without drying
25°C			
100°C			
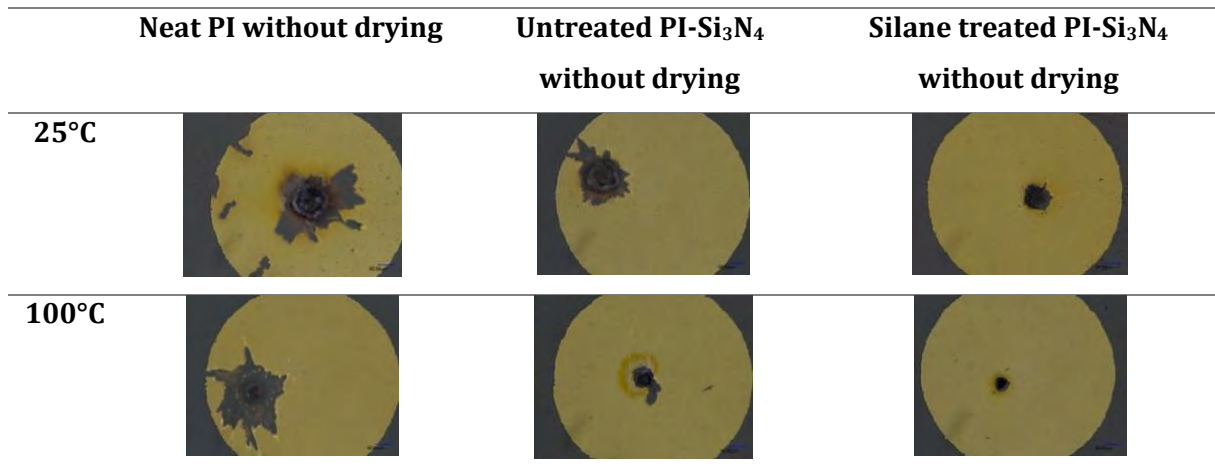
Figure 4-14. Digital microscope images of the failure area

4.3.3. Samples breakdown strength at high temperatures (>150°C)

The temperature dependence of the breakdown strength at 200°C and 250°C of untreated, silane-treated nanocomposite and their corresponding neat material are reported in Table 4-7. It can be noted that PI/Si$_3$N$_4$ NCs show an improvement in their breakdown field compared to the unfilled PI in this temperature range. At 200°C, a BD strength increase of around 19% and 23.5% for untreated and treated NC respectively is observed (from 255 V/μm to 304 and 315 V/μm). At 250°C, an increase of 36% and 22% is noticed for untreated and treated NC. Moreover, in this case the β parameter is higher for the treated NC.

Table 4-7. Weibull parameters for 3 samples measured at 200°C and 250°C

		Alpha (Weibull scale parameter V/μm)	Beta (Weibull shape parameter)
F$_{br}$ at 200°C	PI	255	8.75
	Untreated PI /Si$_3$N$_4$	304	15.23
	Silane-treated PI /Si$_3$N$_4$	315	23.85
F$_{br}$ at 250°C	PI	202	12.13
	Untreated PI /Si$_3$N$_4$	275	9.13
	Silane-treated PI /Si$_3$N$_4$	247	15.98

At high temperature, as already observed for dielectric permittivity results, nanoparticles interphase area may trap ions and/or electronic charge carriers (that causes strong current in the PI) or slow down their mobility. Thus, a reduction of the space charge accumulation occurs [185] as well as an increase of the breakdown strength. This phenomenon is predominant at high temperatures where a high ion mobility is at play.

Moreover, during the breakdown tests, we were able to observe, for high temperatures (>200°C), the presence of self-healing phenomena. When the voltage increases across a metallized sample, weak points such as impurities or defects can lead to localized breakdown in the insulation. The electrical energy supplied is then dissipated through a conductive channel, located at the weak point, collecting locally a high power density which aims to rapidly vaporize the counter electrode on the surface. Thus, this phenomenon can evaporate enough metal from the electrode to isolate the defect, allowing the voltage to be applied again. Irreversible dielectric failure is then reached when the voltage can no longer be applied again across the metallized structure. Figure 4-15 schematically shows the steps of the self-healing process.
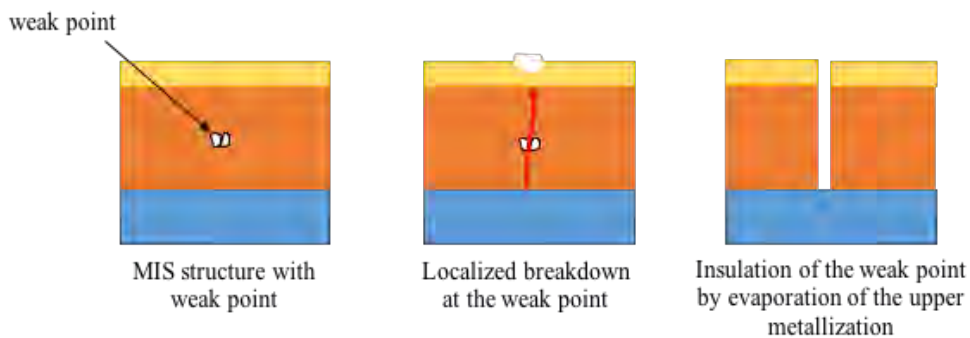
Figure 4-15. Schematic representation of the self-healing phenomenon

The phenomenon of self-healing, when it is very present, appears interesting because it allows the accumulation of a large number of breakdown data, on a reduced population of samples, necessary to obtain a good statistic. However, in our case, self-healing was only observed at some temperatures. Moreover, this phenomenon was very rare since it only appeared 1 to 3 times maximum per sample. Figure 4-16 shows photos of the self-healing phenomenon (bright contours) observed during the breakdown tests.

	Neat PI without drying	Untreated PI-Si$_3$N$_4$ without drying	Silane treated PI-Si$_3$N$_4$ without drying
200°C			
250°C			
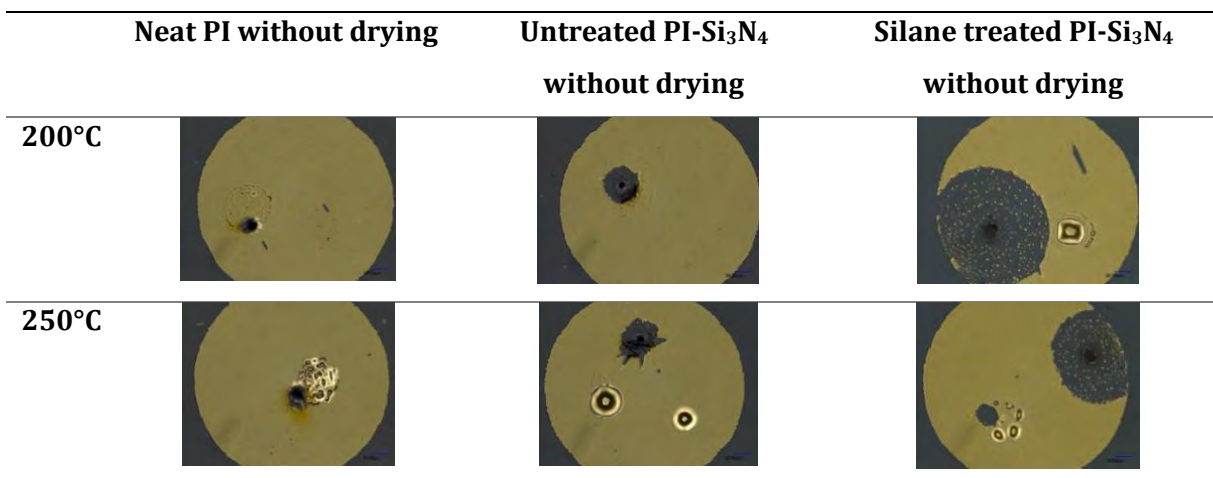
Figure 4-16. Observation of the self-healing phenomenon in MIS structures at high temperatures

4.3.4. Moisture effect on dielectric breakdown strength

The breakdown strength value at high temperature can be affected by the presence of moisture due to the hydrophilicity of the polyimide matrix. Indeed, in dielectric spectroscopy results, the presence of a humidity relaxation peak was observed (see section 4.2.1). In order to eliminate the potential moisture effect, a post-metallization heat treatment was performed on all films just before their BD tests. A drying cycle was chosen by heating all samples at 150°C for 48 hours.

The DC electric strength obtained from Weibull statistics for wet and dry specimens, are reported in Table 4-8. Measurements at 25°C show a small decrease (around 4.3%) of the breakdown value after heating. However, measurements at 200°C show an improvement of the breakdown field, of about 38% for neat PI (from 255 to 352 V/μm before and after heating respectively). For treated and untreated nanocomposite, the difference in the breakdown field before and after drying is less significant (21% and 11% respectively). Consequently, the difference between the breakdown strength of the dried and wet polyimide can be attributed to its high moisture content due to his hydrophilic nature.

Table 4-8. Breakdown strength value at 25°C and 200°C with and without drying.

Breakdown strength measured at 25°C	Without drying	Dried samples
F_{br} **(Polyimide):** Alpha (V/μm)	673	653
F_{br} **(Untreated NC):** Alpha (V/μm)	641	612
F_{br} **(Silane-treated NC):** Alpha (V/μm)	536	506
Breakdown strength measured at 200°C	**Without drying**	**Dried samples**
F_{br} **(Polyimide):** Alpha (V/μm)	255	352
F_{br} **(Untreated NC):** Alpha (V/μm)	304	369
F_{br} **(Silane-treated NC):** Alpha (V/μm)	315	350

4.3.5. Temperature effect on breakdown strength after drying

Table 4-9 shows a comparison of the three samples breakdown strength at 25°C, 200°C, 250°C and 300°C. At low temperatures (25 °C), PI presents a slightly higher breakdown strength than both nanocomposites. However, at high temperature (>200 °C), PI presents a much lower breakdown strength compared to nanocomposites one. In comparison with neat PI, which becomes a semi-insulating material above 300 °C, it seems that PI/Si_3N_4 nanocomposites with silane-treated and untreated nanoparticles are able to keep an extended insulating behavior over 300 °C. Indeed, from temperatures above 200°C, the dielectric strength of the nanocomposite remains almost constant around a value above 3 MV/cm up to 300°C. On the other hand, the

dielectric strength of the unfilled PI deteriorates drastically to 1.58 MV/cm at 300°C. At high temperatures, as seen above, nanoparticles tend to trap and/or slow down the ionic charge carriers that cause strong currents in the PI. This may explain the improvement in dielectric strength in nanocomposite compared to unfilled PI.

Table 4-9. Samples breakdown strength comparison at 25°C, 200°C, 250°C and 300°C

	F_{br} (Polyimide) Alpha (V/μm)	F_{br} (Untreated NC) Alpha (V/μm)	F_{br} (Silane-treated NC) Alpha (V/μm)
25°C	653	612	505
200°C	352	369	350
250°C	240	362	348
300°C	158	300	319

To sum it up, the evolution of the breakdown strength before and after drying of PI, untreated and silane-treated PI/Si$_3$N$_4$ films as a function of temperature from 25°C to 250°C are shown in figure 4-17. Results show that there is a negligible effect for drying at low temperatures. However, at high temperatures, a significant increase in the BD field values occurs after drying. At high temperature (> 200°C), as already observed for dielectric permittivity results, interphase area may trap ions charge carriers or slow down their mobility and thus, increase the breakdown strength. This phenomenon is predominant at high temperatures where high ion mobility is at play. The results reveal that the effect of nanoparticles addition on dielectric strength at this temperature range resulted in the introduction of deep trapping sites that reduce charge carriers mobility. This is certainly related to the more effective control of space charge formation phenomena that can lead to breakdown. Consequently, the interphase might have a good effect on the increase of breakdown strength at high temperatures.
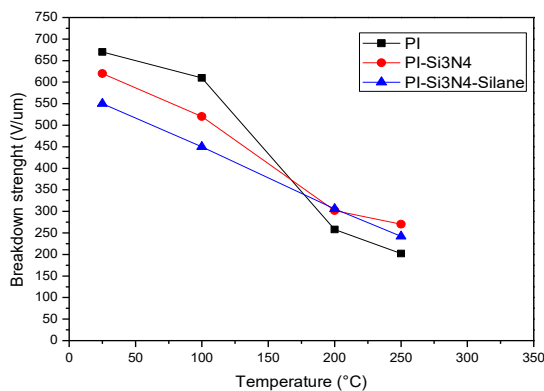
(a)
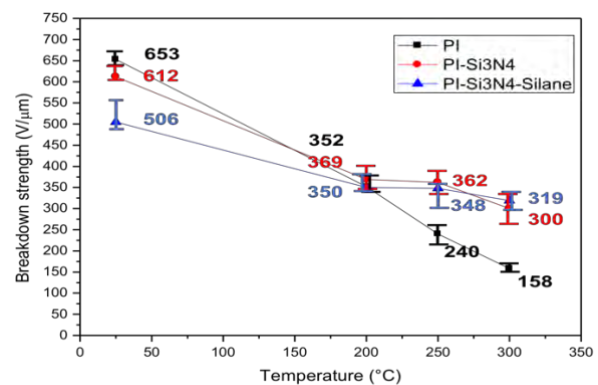
(b)

Figure 4-17. Samples breakdown strength evolution as a function of temperature: (a) before drying and (b) after drying

4.4. Discussion and phenomenological model proposition

From the above results, it can be deduced that the interphase between the nanoparticle and the polymer plays a significant role in the determining of final nanocomposite properties. Based on the interphase model proposal obtained by local measurements (see chapter 3), the purpose of this part is to complete this latter with more details on the interphase characteristics and influence. As a start, we have chosen to consider a dual nanolayer description of the interphase as shown in figure 4-18. The dual nanolayer model was first introduced by Alhabil *et al.* [186]. Indeed, the interphase consists of two regions:

- (i) an interphase layer within nanoparticles boundaries called the **nanoparticle interphase**. This 1st nanolayer is formed close to the nanoparticles surface and is assumed to be tightly bonded and highly immobile. Indeed, it represents an interaction zone where chemical strong bonds, as ionic, covalent or hydrogen bonds relate the NP to the matrix. In addition, this layer presents deep trap for charge carriers.

- (ii) the 2nd nanolayer is an extended and aligned polymer chains over the 1st nanolayer. It is called the **polymer interphase**. It represents a different polymer chain conformation than the matrix, with a better organization as mentioned in section 3.7 Polymer chains are loosely bounded in this layer which presents shallow traps for charge carriers.
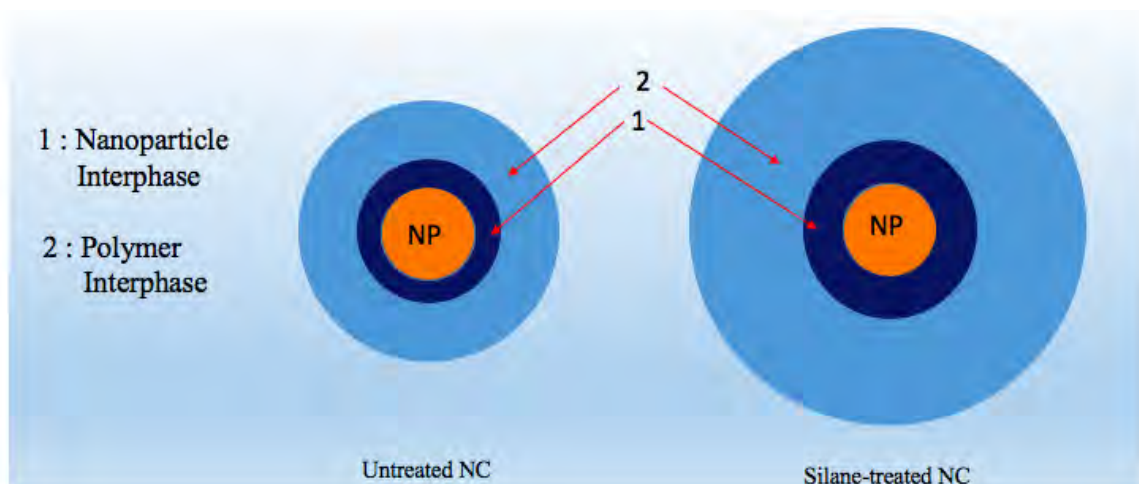
Figure 4-18. The dual nanolayers model of the interphase (not to scale)

4.4.1. Nature of interactions at the nanoparticle interphase

Hydroxyl groups can be present on the nanoparticles as free OH groups attached to the nanoparticle surface (figure 4-19(a)) [187], as OH groups attached to absorbed water molecules or both (figure 4-19(b)) [173]. Indeed, inorganic nanoparticles can absorb water when exposed to a humid environment due to the affinity of H_2O molecules to get bonded to OH groups through

hydrogen bonding. H_2O is a polar molecule and its O is highly prone to hydrogen bonding with the free OH present on the nanoparticle surface.
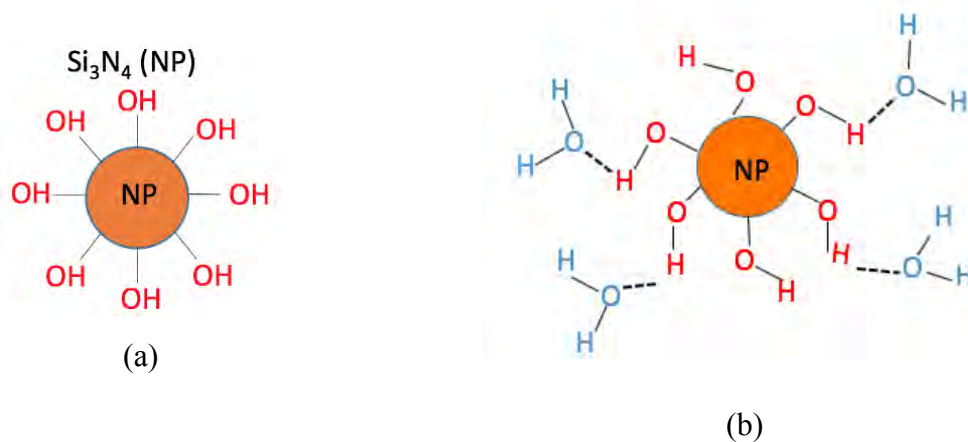
Figure 4-19. Different configurations of the presence of OH groups on the NP surface: (a) free OH groups and (b) free and water bonded OH groups (not to scale)

The NP silane surface chemical treatment has shown a beneficial effect on polymer/nanoparticle coupling (AFM and TEM images). The reason behind this better interaction between particles and polymer is shown in figure 4-20. Indeed, the presence of silane decreases the number of sites on the surface of NP capable of hosting adsorbed OH bonds. This latter is replaced by O-Si-O-NH2 bonds [188] as described in the functionalization scheme on figure 4-20(b). These new bonds, within the nanoparticle interphase area, allow a better interaction with PI chains.
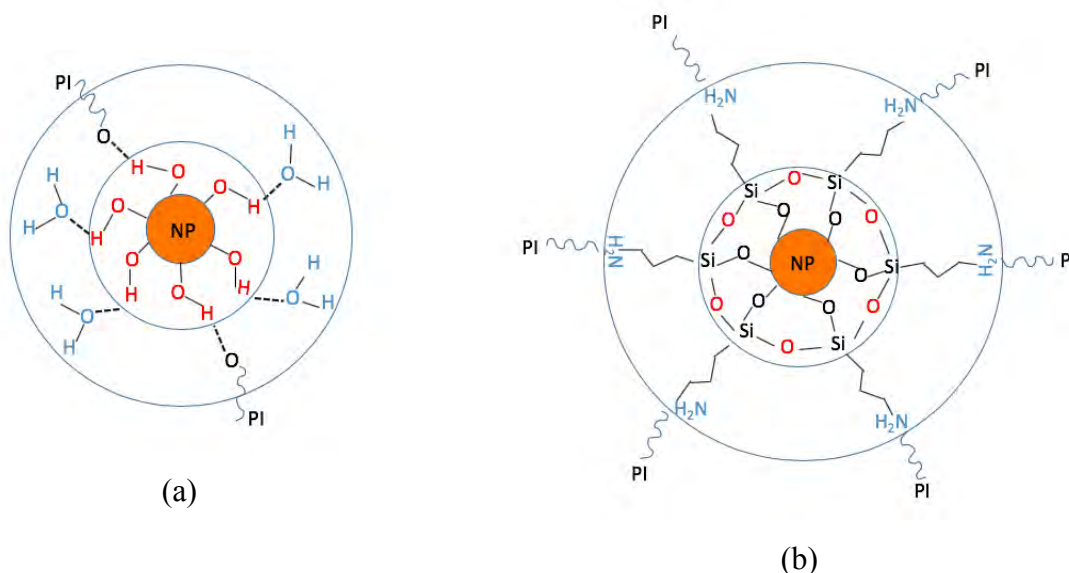
Figure 4-20. The effect of silane treatment on the interphase chemical treatment: (a) untreated particles and (b) treated particles (not to scale)

4.4.2. Impact of the interphase on dielectric properties

Experimental measurements showed that the relative permittivity of the untreated nanocomposite (below 150°C) was lower than those of the silane-treated nanocomposite and the unfilled polymer. This is probably related to the nature of bonding at the nanoparticle interphase (1st nanolayer). Indeed, an abundance of strong hydrogen bonds exists between OH groups and both PI and H_2O molecules. Therefore, the inhibition in the mobility of polyimide chains leading to the reduction in the untreated nanocomposite permittivity is probably due to this strong hydrogen bonding [19]. However, the presence of silane group in the nanoparticle interphase in the case of silane-treated nanocomposite may be the raison in the effective permittivity increasing. It is important to mention that at low temperature, where the charge carriers mobility is low, the dielectric behavior is related to the intrinsic structure of the material.

Moreover, the nanoparticle interphase constitution can influence the electrical conduction process in the bulk of the nanocomposite. Results show that the untreated one has, at low frequency, a higher conductivity (related to higher dielectric losses) compared to unfilled and silane-treated nanocomposite. This is attributed to the presence of water in the nanoparticle interphase (1st nanolayer) for untreated NC, surrounding each filler particle as a thin shell as proposed by Zou *et al.* [63]. The water shell model explains how this thin shell can enhance charge transport processes in the dielectric bulk increasing conductivity and losses. The charge transport between adjacent water shells is provided by a charge hopping process between localized conductive states [189].

On the other hand, a lower conductivity (and thus dielectric losses) is observed for the treated NC. This reduction of the conductivity, previously related to moisture absorption in untreated nanocomposite, is due to the hydrophobic nature of the interphase after silane treatment (at the 1st nanolayer). Moreover, the silane treatment affects the chemical structure of this nanolayer where stronger interactions with the nanoparticle may act as barriers to the charge carriers mobility.

It is suggested that polymer interphase (2nd nanolayer) has a larger conductivity than the nanoparticle interphase (1st nanolayer) due to the presence of loose polyimide segments. This may allow the existence of free charge carriers (due to impurities) with a higher mobility.

A last explication of the different conductivity between untreated and treated NC could be related to the nanoparticles dispersion within the polymer matrix. (i) In the case of untreated nanoparticles, the inter-particle distances are small due to the aggregates formation as shown in figure 4-21(a). The fraction of the nanoparticle interphase (1st nanolayer) which is a conductive layer is high within aggregates. Hence, electrical conduction can take place easily due to the close

proximity of nanoparticle interphase regions. However, (ii) in the case of silane-treated nanoparticles, the inter-nanoparticle distances are large leading to a more tortuous conducting path compared to untreated NC due to the good dispersion as shown in figure 4-21(b). Thus, the treated NC presents a less conductivity than the untreated one.

(a)   (b)
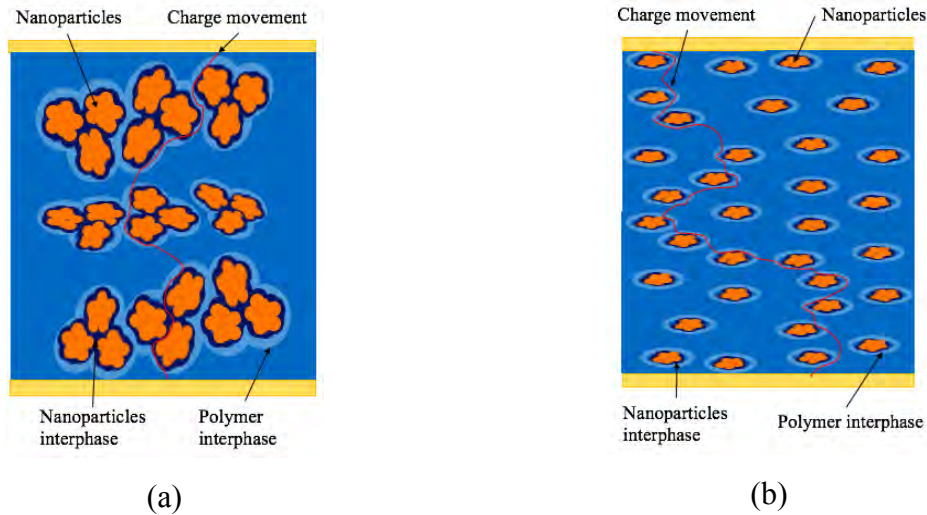
Figure 4-21. Scematic representation of the nanoparticles dispersion effect on dielectric conductivity: (a) for untreated NC and (b) for treated NC

4.4.3. Impact of the interphase on dielectric strength

Charge carriers in a DC electrical breakdown process experience a rapidly changing electric field from a very low value to a very high value in a very short period of time (between 10 to 20 s). Hence, the electrical conduction mechanism changes from a low E-field process to a very high E-field process. At very high E-fields, the electrical conduction can also be significantly influenced by charge carriers injection from electrodes into the nanocomposite material. Therefore, on the basis of our previous results on the interphase role on charge carriers mobility, we suppose that the characteristics of the interphase region have also an influence on the nanocomposite dielectric breakdown.

In this study, it has been shown that the dielectric strength values for both untreated and silane-treated nanocomposites decrease compared to unfilled PI at temperatures below 200°C. This was related to the fact that fillers in the polymer matrix create defects and also introduce additional charge carriers in the volume of the material thereby reducing the dielectric strength in composites. Moreover, the breakdown value for silane-treated NC is lower than that of the untreated one. Two reasons could be behind this behavior: (i) in silane-treated NC, the conduction of charge carriers is inhibited between electrodes due to the presence of a high fraction of polymeric regions between the well dispersed particles (tortuous path for charge carriers). (ii) Nanoscale measurements have shown that the interphase fraction volume is higher in silane-

treated NC. It was also demonstrated that the interphase permittivity is lower than the matrix one. So, the higher volume of a lower permittivity phase could generate a local electric field enhancement and accelerate the breakdown process.

At high temperatures, nanocomposites present a higher breakdown strength than neat PI. Indeed, PI shows ionic space charge contribution leading to a field reinforcement (hetero space charge) and secondary injection phenomena at the sample/electrode interface (figure 4-22(a)). For nanocomposites, Si_3N_4 nanoparticles act as deep traps for mobile ionic species particularly activated with temperature (see figure 4-22(b) and (c)). Thus, these results prove that an efficient control of the trapping parameters allows huge enhancement of the insulating properties of PI nanocomposites. High temperature breakdown can be delayed by free carriers reduction through deep trap formation caused by nanoparticles addition.

(a)

(b)   (c)
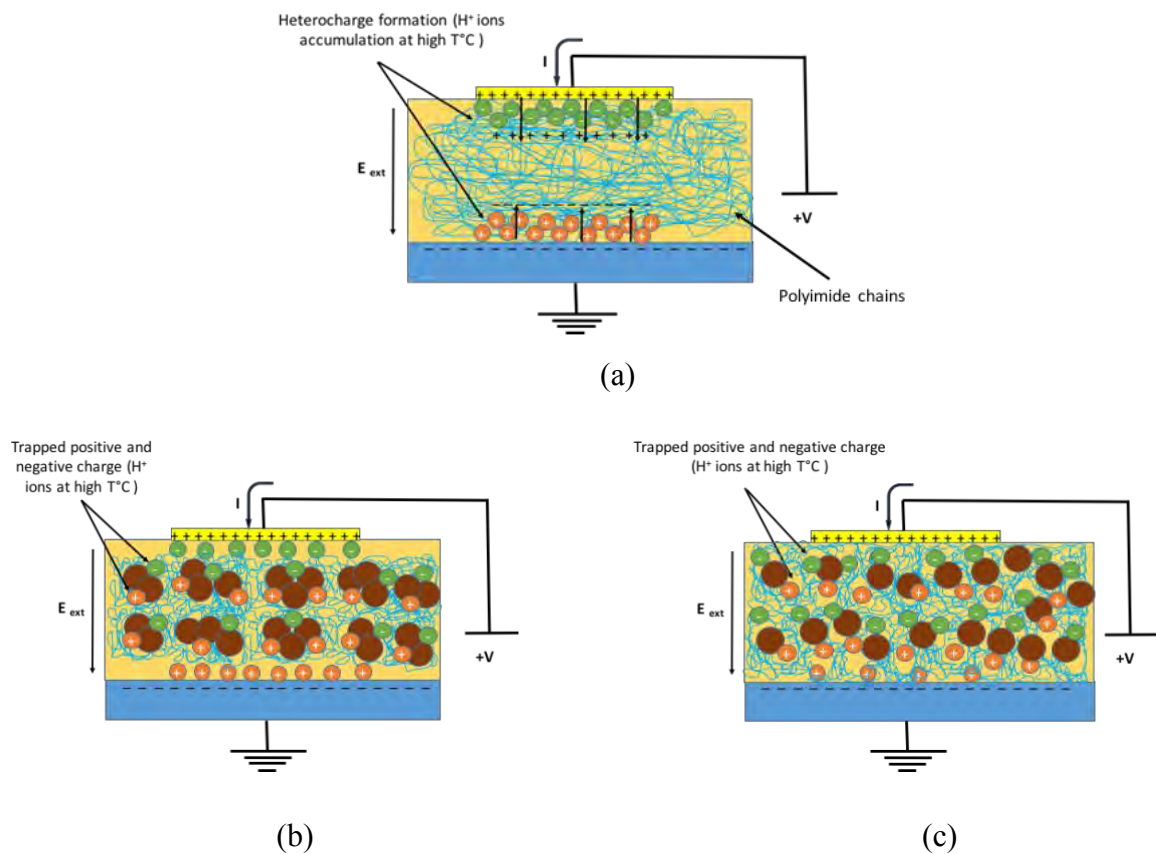
Figure 4-22. Schematic representation of ionic species behavior at high temperature and under electric field: (a) for neat PI, (b) for untreated NC and (c) for treated NC.

4.5. Conclusion

This chapter focuses on the influence of the interphase on NC macroscopic properties. For this reason, dielectric spectroscopy and breakdown strength measurements were performed on unfilled PI, untreated and silane-treated PI/Si3N4 nanocomposites.

At low temperature, the measurement of the macroscopic effective nanocomposite permittivity has allowed us to determine the interphase volume fraction by using the nanoscale permittivity results injected in a mixing law treatment. Moreover, the interphase chemical nature (water or silane coupling agent presence) effect on the AC conductivity and dielectric losses was discussed.

At high temperature, dielectric spectroscopy and breakdown strength measurements emphasize that NPs modify nanocomposite properties (breakdown strength increase and dielectric permittivity decrease). This evolution was attributed to the reduction of H+ ions mobility in nanocomposites layer due to the presence of the interphase, which acts as traps for ions. In addition, the improvement is higher for treated nanoparticles than untreated ones due to their higher interphase thickness/volume fraction.

A phenomenological model was proposed to describe experimental results and phenomena at play in the interphase region in order to correlate nanoscale observations to macroscopic nanocomposites final properties.

Furthermore, these results seem to have highlighted nanodielectric effects, especially at high temperatures, in PI/Si3N4 films conditioned by the introduction of nanoparticles. The electrical properties obtained seem promising and compatible with high temperature electrical insulation.

General conclusions and perspectives

Conclusion

The work presented in this thesis gives a new vision on how local measurements with Atomic Force Microscope (AFM) make it possible, by using polymer nanocomposite surface mapping, to investigate the interphase area. AFM is used to make at the same time qualitative and quantitative measurements of these zones within Polyimide/Silicon Nitride (PI/Si_3N_4) nanocomposite. Results show that the Peak Force Quantitative Nano Mechanical (PF QNM) AFM mode reveals the presence of the interphase by measuring its mechanical properties (Young modulus). However, in order to achieve quantitative measurements, a meticulous calibration step has to be done. Moreover, Electrostatic Force Microscopy (EFM) mode is used in order to detect and characterize matrix and interphases local permittivities. The effect of the surface functionalization of spherical Si_3N_4 nanoparticles on the interphase within the PI matrix is also reported. These mechanical and electrical quantitative results have permitted comparing the interphase dimension and properties between treated and untreated Si_3N_4 nanoparticles. Results show that the interphase presents a higher Young modulus and a lower permittivity compared to neat PI. The particles silane treatment increases the interphase thickness but has no effect on its dielectric properties. Thus, experimental results are confronted with theoretical models. A new model based on these experimental results is proposed.

In order to correlate the local characterization to macroscopic properties modification, especially at high temperatures, the second part of this study has concerned an investigation on the macroscopic dielectric properties and breakdown strength of PI/Si_3N_4 nanocomposite films. The dielectric properties of neat PI, untreated and treated nanocomposite are investigated from -150 to 350 °C. The role of the Si_3N_4 nanofillers on the reduction of the electrode polarization relaxation phenomenon due to ionic movements is reported. For untreated nanoparticles, effects are less important due to aggregate formation within the films. In contrast, a higher decrease is obtained by functionalizing the nanofillers surface with a silane coupling agent which improves the grafting of PI chains on nanoparticles. The variation in the dielectric performance point to the nanoparticle interphase as an essential reason. On the other hand, breakdown strength characterizations show that the nanocomposite has considerably better performance at high temperature (>200°C) compared to neat PI. In such temperature range (up to 350 °C), the electrical properties of neat PI are controlled by ionic motions, which make it a semi-insulating material. Consequently, this study has helped to explain why it is possible to extend both the

electric field and temperature ranges of PI films thanks to an adequate nano-structuration. Thus, these results show the paramount importance of the interphase thickness and nature for designing dielectric properties of nanodielectrics.

Perspectives

The work presented in this thesis could be continued towards 2 main axes.

The first axe aims at identifying physical phenomena and pertinent parameters impacting the interphase dimension. This can be achieved thanks to a design of different matrix and fillers (different nature, shape, size and volume fraction) to propose appropriate mixed rules for dielectric permittivity, which manage to reproduce macroscale properties. A new experiments approach combining several matrixes and surface controlled nanofillers, i.e. controlled interphases, with recent nanoscale characterization methods could be proposed.

The second aim is to understand the interphase influence on macroscale properties. Nanocomposites should be characterized at nanoscale and macroscopic scale in terms of morphology (nanofillers dispersion, …), dielectric properties (space charges, dielectric permittivity, charges transport…) and interphase properties (thickness, dielectric permittivity). Some characterization tools are well controlled. However, some techniques related to multiscale characterization of dielectric properties and charge density need to be developed. Multiscale models also need to be developed to confirm and predict the dielectric behavior of the nanocomposites.

References

[1]   S. Diaham, M.-L. Locatelli, and R. Khazak, "BPDA-PDA Polyimide: Synthesis, Characterizations, Aging and Semiconductor Device Passivation," in *High Performance Polymers - Polyimides Based - From Chemistry to Applications*, 2012.

[2]   K. Kinoshita and A. Yamaji, "Grain-size effects on dielectric properties in barium titanate ceramics," *J. Appl. Phys.*, 1976.

[3]   Y. He, "Heat capacity, thermal conductivity, and thermal expansion of barium titanate-based ceramics," *Thermochim. Acta*, 2004.

[4]   A. Kishimoto, K. Koumoto, and H. Yanagida, "Mechanical and dielectric failure of BaTiO3 ceramics," *J. Mater. Sci.*, 1989.

[5]   T. Tanaka, G. C. Montanari, and R. Mülhaupt, "Polymer nanocomposites as dielectrics and electrical insulation- perspectives for processing technologies, material characterization and future applications," in *IEEE Transactions on Dielectrics and Electrical Insulation*, 2004.

[6]   Camargo Pedro Henrique Cury, Satyanarayana Kestur Gundappa, and Wypych Fernando, "Nanocomposites : Synthesis , Structure , Properties and New Application Opportunities," *Mater. Res.*, 2009.

[7]   J. K. Nelson, "Background, principles and promise of nanodielectrics," in *Dielectric Polymer Nanocomposites*, 2010.

[8]   B. Suresha, G. Chandramohan, N. M. Renukappa, and Siddaramaiah, "Influence of silicon carbide filler on mechanical and dielectric properties of glass fabric reinforced epoxy composites," *J. Appl. Polym. Sci.*, 2009.

[9]   L. Desmars, J. Galy, D. Bachellerie, A. Cristiano-Tassi, S. Haller, and S. Pruvost, "High Voltage Electrical Properties of Epoxy / h-BN Microcomposites," in *2018 IEEE 2nd International Conference on Dielectrics, ICD 2018*, 2018.

[10]   A. Alias, Z. Ahmad, and A. B. Ismail, "Preparation of polyimide/Al2O3 composite films as improved solid dielectrics," *Mater. Sci. Eng. B Solid-State Mater. Adv. Technol.*, 2011.

[11]   Y. S. Ham and J. H. Koh, "A study on the electrical properties of SrTiO3-epoxy composite thick films for embedded capacitor applications," in *Ferroelectrics*, 2010.

[12]   S. Kume, I. Yamada, K. Watari, I. Harada, and K. Mitsuishi, "High-thermal-conductivity AlN filler for polymer/ceramics composites," in *Journal of the American Ceramic Society*, 2009.

[13]   D. Ma *et al.*, "Influence of nanoparticle surface modification on the electrical behaviour

of polyethylene nanocomposites," *Nanotechnology*, 2005.

[14] J. K. Nelson and J. C. Fothergill, "Internal charge behaviour of nanocomposites," *Nanotechnology*, 2004.

[15] J. K. Nelson and Y. Hu, "Nanocomposite dielectrics - Properties and implications," in *Journal of Physics D: Applied Physics*, 2005.

[16] J. Castellon *et al.*, "Electrical properties analysis of micro and nano composite epoxy resin materials," *IEEE Trans. Dielectr. Electr. Insul.*, 2011.

[17] T. Tanaka, "Dielectric nanocomposites with insulating properties," in *IEEE Transactions on Dielectrics and Electrical Insulation*, 2005.

[18] S. Singha and M. J. Thomas, "Dielectric properties of epoxy nanocomposites," *IEEE Trans. Dielectr. Electr. Insul.*, 2008.

[19] S. Singha and M. J. Thomas, "Reduction of permittivity in epoxy nanocomposites at low nano-filler loadings," in *Annual Report - Conference on Electrical Insulation and Dielectric Phenomena, CEIDP*, 2008.

[20] Q. Wang and G. Chen, "Effect of nanofillers on the dielectric properties of epoxy nanocomposites," *Adv. Mater. Res.*, 2012.

[21] G. Iyer, R. S. Gorur, R. Richert, A. Krivda, and L. E. Schmidt, "Dielectric properties of epoxy based nanocomposites for high voltage insulation," *IEEE Trans. Dielectr. Electr. Insul.*, 2011.

[22] Z. Han and R. Garrett, "Overview of Polymer Nanocomposites as Dielectrics and Electrical Insulation Materials for Large High Voltage Rotating Machines," *NSTI-Nanotech*, 2008.

[23] L. Zhe, K. Okamoto, Y. Ohki, and T. Tanaka, "Role of nano-filler on partial discharge resistance and dielectric breakdown strength of micro-Al2O3/ epoxy composites," *9th Int. Conf. Prop. Appl. Dielectr. Mater.*, 2009.

[24] T. Imai, F. Sawa, T. Yoshimitsu, T. Ozaki, and T. Shimizu, "Preparation and insulation properties of epoxy-layered silicate nanocomposite [insulating material applications]," *Electrical Insulation and Dielectric Phenomena, 2004. CEIDP '04. 2004 Annual Report Conference on*. 2004.

[25] J. Castellon *et al.*, "Space charge behaviour on epoxy based dielectrics filled with micro and nano silica," in *Proceedings of the 2010 IEEE International Conference on Solid Dielectrics, ICSD 2010*, 2010.

[26] C. Stancu *et al.*, "Electric Field Computation in Water Treed Polyethylene with Space Charge Accumulation," 2006.

[27] L. A. Dissado, G. Mazzanti, and G. C. Montanari, "The role of trapped space charges in the electrical aging of insulating materials," *IEEE Trans. Dielectr. Electr. Insul.*, vol. 4, no. 5, pp. 496–506, 1997.

[28] J. Castellon, S. Agnel, A. Toureille, and M. Fréchette, "Space charge characterization of multi-stressed microcomposite nano-filled epoxy for electrotechnical applications," in *Annual Report - Conference on Electrical Insulation and Dielectric Phenomena, CEIDP*, 2008.

[29] T. Andritsch, R. Kochetov, B. Lennon, P. H. F. Morshuis, and J. J. Smit, "Space charge behavior of magnesium oxide filled epoxy nanocomposites at different temperatures and electric field strengths," in *2011 Electrical Insulation Conference, EIC 2011*, 2011.

[30] F. Magraner, A. García-Bernabé, M. Gil, P. Llovera, S. J. Dodd, and L. A. Dissado, "Space charge measurements on different epoxy resinalumina nanocomposites," in *Proceedings of the 2010 IEEE International Conference on Solid Dielectrics, ICSD 2010*, 2010.

[31] D. Fabiani, G. C. Montanaril, A. Dardano, G. Guastavino, L. Testa, and M. Sangermano, "Space charge dynamics in nanostructured epoxy resin," in *Annual Report - Conference on Electrical Insulation and Dielectric Phenomena, CEIDP*, 2008.

[32] J. K. Nelson, "Overview of nanodielectrics: Insulating materials of the future," in *2007 Electrical Insulation Conference and Electrical Manufacturing Expo, EEIC 2007*, 2007.

[33] T. Andritsch, R. Kochetov, Y. T. Gebrekiros, P. H. F. Morshuis, and J. J. Smit, "Short term DC breakdown strength in epoxy based BN nano- and microcomposites," in *Proceedings of the 2010 IEEE International Conference on Solid Dielectrics, ICSD 2010*, 2010.

[34] G. H. Meier, *Thermodynamics of surfaces and interfaces: Concepts in inorganic materials*. 2014.

[35] Y. Li, Y. Huang, T. Krentz, B. Natarajan, T. Neely, and L. S. Schadler, "Polymer Nanocomposite Interfaces: The Hidden Lever for Optimizing Performance in Spherical Nanofilled Polymers," in *Interface/Interphase in Polymer Nanocomposites*, 2016.

[36] T. J. Lewis, "Nanometric Dielectrics," *IEEE Trans. Dielectr. Electr. Insul.*, 1994.

[37] J. K. Nelson, *Dielectric polymer nanocomposites*. 2010.

[38] D. EL KHOURY, "Towards the use of Electrostatic Force Microscopy to study interphases in nanodielectric materials," 2018.

[39] M. F. Fréchette, M. L. Trudeau, H. D. Alamdari, and S. Boily, "Introductory remarks on nanodielectrics," in *IEEE Transactions on Dielectrics and Electrical Insulation*, 2004.

[40] G. C. Psarras, "Nanodielectrics: an emerging sector of polymer nanocomposites," *Express Polym. Lett.*, 2008.

[41] Y. Sun, Z. Zhang, and C. P. Wong, "Influence of interphase and moisture on the dielectric spectroscopy of epoxy/silica composites," *Polymer (Guildf).*, 2005.

[42] S. Diaham, F. Saysouk, M. L. Locatelli, and T. Lebey, "Huge nanodielectric effects in polyimide/boron nitride nanocomposites revealed by the nanofiller size," *J. Phys. D. Appl. Phys.*, 2015.

[43] J. K. Nelson, J. C. Fothergill, L. A. Dissado, and W. Peasgood, "Towards an understanding of nanometric dielectrics," 2003.

[44] S. Diaham, E. Pizzutilo, and M.-L. Locatelli, "DC dielectric strength of epoxy/Si<inf>3</inf>N<inf>4</inf> nanocomposites," in *Proceedings of the 2016 IEEE International Conference on Dielectrics, ICD 2016*, 2016.

[45] S. Raetzke and J. Kindersberger, "Role of interphase on the resistance to high-voltage arcing, on tracking and erosion of silicone/SiO2nanocomposites," *IEEE Trans. Dielectr. Electr. Insul.*, 2010.

[46] C.-H. Lee and J.-J. Park, "The Partial Discharge Resistances of Epoxy-Nano-and-Micro Composites," *Trans. Electr. Electron. Mater.*, 2010.

[47] R. Y. Hong and Q. Chen, "Dispersion of inorganic nanoparticles in polymer matrices: Challenges and solutions," *Adv. Polym. Sci.*, 2014.

[48] M. Roy, J. K. Nelson, R. K. MacCrone, and L. S. Schadler, "Candidate mechanisms controlling the electrical characteristics of silica/XLPE nanodielectrics," *J. Mater. Sci.*, 2007.

[49] M. Roy, J. K. Nelson, L. S. Schadler, C. Zou, and J. C. Fothergill, "The influence of physical and chemical linkage on the properties of nanocomposites," in *Annual Report - Conference on Electrical Insulation and Dielectric Phenomena, CEIDP*, 2005.

[50] M. Roy *et al.*, "Polymer nanocomposite dielectrics - The role of the interface," *IEEE Trans. Dielectr. Electr. Insul.*, 2005.

[51] E. Helal, E. David, M. Fréchette, and N. R. Demarquette, "Thermoplastic elastomer nanocomposites with controlled nanoparticles dispersion for HV insulation systems: Correlation between rheological, thermal, electrical and dielectric properties," *Eur. Polym. J.*, 2017.

[52] T. Andritsch, R. Kochetov, P. H. F. Morshuis, and J. J. Smit, "Proposal of the polymer chain alignment model," in *Annual Report - Conference on Electrical Insulation and Dielectric Phenomena, CEIDP*, 2011.

[53] M. Z. Rong, M. Q. Zhang, and W. H. Ruan, "Surface modification of nanoscale fillers for improving properties of polymer nanocomposites: a review," *Mater. Sci. Technol.*, 2006.

[54] "Sibond Inc.: Silane Coupling Agents." [Online]. Available: http://www.sibond.com/index.php/Home/Index/coupling_agent. [Accessed: 08-Jul-2019].

[55] R. K. MacCrone, J. K. Nelson, R. C. Smith, and L. S. Schadler, "The use of electron paramagnetic resonance in the probing of the nano-dielectric interface," *IEEE Trans. Dielectr. Electr. Insul.*, 2008.

[56] M. Stamm, "Polymer surface and interface characterization techniques," in *Polymer Surfaces and Interfaces: Characterization, Modification and Applications*, 2008.

[57] A. I. RUSANOV, "Recent Investigations on the Thickness of Surface Layers," 2013.

[58] T. J. Lewis, "Interfaces are the dominant feature of dielectrics at the nanometric level," in *IEEE Transactions on Dielectrics and Electrical Insulation*, 2004.

[59] T. J. Lewis, "Nano-Composite Dielectrics: The Dielectric Nature of the Nano-Particle Environment," *IEEJ Trans. Fundam. Mater.*, 2007.

[60] T. Tanaka, M. Kozako, N. Fuse, and Y. Ohki, "Proposal of a multi-core model for polymer nanocomposite dielectrics," *IEEE Trans. Dielectr. Electr. Insul.*, 2005.

[61] G. Tsagaropoulos and A. Eisenberg, "Dynamic Mechanical Study of the Factors Affecting the Two Glass Transition Behavior of Filled Polymers. Similarities and Differences with Random Ionomers," *Macromolecules*, 1995.

[62] V. Arrighi, I. J. McEwen, H. Qian, and M. B. Serrano Prieto, "The glass transition and interfacial layer in styrene-butadiene rubber containing silica nanofiller," *Polymer (Guildf).*, 2003.

[63] C. Zou, J. C. Fothergill, and S. W. Rowe, "The effect of water absorption on the dielectric properties of epoxy nanocomposites," *IEEE Trans. Dielectr. Electr. Insul.*, 2008.

[64] D. PITSA and M. G. DANIKAS, "INTERFACES FEATURES IN POLYMER NANOCOMPOSITES: A REVIEW OF PROPOSED MODELS," *Nano*, 2011.

[65] T. Tanaka, "A novel concept for electronic transport in nanoscale spaces formed by islandic multi-cored nanoparticles," in *Proceedings of the 2016 IEEE International Conference on Dielectrics, ICD 2016*, 2016.

[66] A. M. Pourrahimi, R. T. Olsson, and M. S. Hedenqvist, "The Role of Interfaces in Polyethylene/Metal-Oxide Nanocomposites for Ultrahigh-Voltage Insulating Materials," *Adv. Mater.*, 2018.

[67] P. Maity, N. Gupta, V. Parameswaran, and S. Basu, "On the size and dielectric properties of the interphase in epoxy-alumina nanocomposite," *IEEE Trans. Dielectr. Electr. Insul.*, 2010.

[68] E. Vassileva and K. Friedrich, "Epoxy/alumina nanoparticle composites. I. Dynamic

mechanical behavior," *J. Appl. Polym. Sci.*, 2003.

[69] C. Daily, W. Sun, M. Kessler, X. Tan, and N. Bowler, "Modeling the interphase of a polymer-based nanodielectric," *IEEE Trans. Dielectr. Electr. Insul.*, 2014.

[70] W. Wang and S. Li, "A transition of interface characteristics in LDPE/Al2O3 nanocomposites by permittivity simulation," *IEEE Trans. Dielectr. Electr. Insul.*, 2018.

[71] M. Paredes, C.Angammana, and S.Jayaram, "Modeling the Interphase of Silicone/SiO2 Nanodielectrics," in *Proc. 2015 ESA Annu. Meet. Electrostat., (California State Polytechnic University, Pomona)*, 2015.

[72] O. Dugne, S. Prouhet, A. Guette, R. Naslain, and J. Sevely, "Interface Characterisation by Transmission Electron Microscopy and Auger Electron Spectroscopy in Tough SiC Fiber (Nicalon)-SiC Matrix Composite with a Boron Nitride Interphase," in *Developments in the Science and Technology of Composite Materials*, 2011.

[73] Q. Wu, M. Li, Y. Gu, Y. Li, and Z. Zhang, "Nano-analysis on the structure and chemical composition of the interphase region in carbon fiber composite," *Compos. Part A Appl. Sci. Manuf.*, 2014.

[74] Q. Wu, M. Li, Y. Gu, S. Wang, and Z. Zhang, "Imaging the interphase of carbon fiber composites using transmission electron microscopy: Preparations by focused ion beam, ion beam etching, and ultramicrotomy," *Chinese J. Aeronaut.*, 2015.

[75] B. E. B. Uribe and J. R. Tarpani, "Interphase analysis of hierarchical composites via transmission electron microscopy," *Compos. Interfaces*, 2017.

[76] D. R. Clarke and P. R. Stuart, "An anomalous contrast effect in the scanning electron microscope," *J. Phys. E.*, 1970.

[77] M. A. Stevens Kalceff, M. R. Phillips, and A. R. Moon, "Electron irradiation-induced changes in the surface topography of silicon dioxide," *J. Appl. Phys.*, 1996.

[78] D. C. Joy, "Control of charging in low-voltage SEM," *Scanning*, 1989.

[79] M. Belhaj, S. Odof, K. Msellak, and O. Jbara, "Time-dependent measurement of the trapped charge in electron irradiated insulators: Application to Al2O3-sapphire," *J. Appl. Phys.*, 2000.

[80] S. Fakhfakh, O. Jbara, M. Belhaj, Z. Fakhfakh, A. Kallel, and E. I. Rau, "An experimental approach for dynamic investigation of the trapping properties of glass-ceramic under electron beam irradiation from a scanning electron microscope," *Eur. Phys. J. Appl. Phys.*, 2003.

[81] D. A. Jesson and J. F. Watts, "The interface and interphase in polymer matrix composites: Effect on mechanical properties and methods for identification," *Polymer Reviews*. 2012.

[82] J. K. Kim, M. L. Sham, and J. Wu, "Nanoscale characterisation of interphase in silane treated glass fibre composites," *Compos. Part A Appl. Sci. Manuf.*, 2001.

[83] G. M. Pharr, "An improved technique for determining hardness and elastic modulus using load and displacement sensing indentation experiments," *J. Mater. Res.*, 1992.

[84] A. Hodzic, Z. H. Stachurski, and J. K. Kim, "Nano-indentation of polymer-glass interfaces. Part I. Experimental and mechanical analysis," *Polymer (Guildf).*, 2000.

[85] A. Hodzic, S. Kalyanasundaram, J. K. Kim, A. E. Lowe, and Z. H. Stachurski, "Application of nano-indentation, nano-scratch and single fibre tests in investigation of interphases in composite materials," *Micron*, 2001.

[86] A. Hodzic, J. K. Kim, A. E. Lowe, and Z. H. Stachurski, "The effects of water aging on the interphase region and interlaminar fracture toughness in polymer-glass composites," *Compos. Sci. Technol.*, 2004.

[87] A. M. Díez-Pascual, M. A. Gómez-Fatou, F. Ania, and A. Flores, "Nanoindentation assessment of the interphase in carbon nanotube-based hierarchical composites," *J. Phys. Chem. C*, 2012.

[88] E. Mäder, S.-L. Gao, and J.-K. Kim, "New Nano-Scale Characterization Techniques for Interphases," in *Interface Controlled Materials*, 2005.

[89] S. B. Yedla, M. Kalukanimuttam, R. M. Winter, and S. K. Khanna, "Effect of Shape of the Tip in Determining Interphase Properties in Fiber Reinforced Plastic Composites Using Nanoindentation," *J. Eng. Mater. Technol.*, 2008.

[90] E. M der and S. Gao, "Prospect of nanoscale interphase evaluation to predict composite properties," *J. Adhes. Sci. Technol.*, 2001.

[91] Z. Derbali, A. Fahs, J. F. Chailan, I. V. Ferrari, M. L. Di Vona, and P. Knauth, "Composite anion exchange membranes with functionalized hydrophilic or hydrophobic titanium dioxide," *Int. J. Hydrogen Energy*, 2017.

[92] D. M. Panaitescu *et al.*, "Structural and morphological characterization of bacterial cellulose nano-reinforcements prepared by mechanical route," *Mater. Des.*, 2016.

[93] L. Teodonio, M. Missori, D. Pawcenis, J. Łojewska, and F. Valle, "Nanoscale analysis of degradation processes of cellulose fibers," *Micron*, 2016.

[94] F. Khelifa, Y. Habibi, P. Leclère, and P. Dubois, "Convection-assisted assembly of cellulose nanowhiskers embedded in an acrylic copolymer," *Nanoscale*, 2013.

[95] E. D. Cranston *et al.*, "Determination of Young's modulus for nanofibrillated cellulose multilayer thin films using buckling mechanics," *Biomacromolecules*, 2011.

[96] D. M. Panaitescu, A. N. Frone, and C. Nicolae, "Micro- and nano-mechanical

characterization of polyamide 11 and its composites containing cellulose nanofibers," *Eur. Polym. J.*, 2013.

[97] L. Lopez-Figueras, N. Navascues, and S. Irusta, "Polycaprolactone/mesoporous silica MCM-41 composites prepared by in situ polymerization," *Particuology*, 2017.

[98] D. M. Panaitescu, A. N. Frone, and I. C. Spataru, "Effect of nanosilica on the morphology of polyethylene investigated by AFM," *Compos. Sci. Technol.*, 2013.

[99] B. Megevand, S. Pruvost, L. C. Lins, S. Livi, J. F. Gérard, and J. Duchet-Rumeau, "Probing nanomechanical properties with AFM to understand the structure and behavior of polymer blends compatibilized with ionic liquids," *RSC Adv.*, 2016.

[100] D. Wang, T. P. Russell, T. Nishi, and K. Nakajima, "Atomic force microscopy nanomechanics visualizes molecular diffusion and microstructure at an interface," *ACS Macro Lett.*, 2013.

[101] P. Xavier and S. Bose, "Nanomechanical Mapping, Hierarchical Polymer Dynamics, and Miscibility in the Presence of Chain-End Grafted Nanoparticles," *Macromolecules*, 2016.

[102] Y. F. Niu, Y. Yang, S. Gao, and J. W. Yao, "Mechanical mapping of the interphase in carbon fiber reinforced poly(ether-ether-ketone) composites using peak force atomic force microscopy: Interphase shrinkage under coupled ultraviolet and hydro-thermal exposure," *Polym. Test.*, 2016.

[103] A. Pakzad, J. Simonsen, and R. S. Yassar, "Gradient of nanomechanical properties in the interphase of cellulose nanocrystal composites," *Compos. Sci. Technol.*, 2012.

[104] M. Mousa and Y. Dong, "Novel three-dimensional interphase characterisation of polymer nanocomposites using nanoscaled topography," *Nanotechnology*, 2018.

[105] D. Wang *et al.*, "Production of a cellular structure in carbon nanotube/natural rubber composites revealed by nanomechanical mapping," *Carbon N. Y.*, 2010.

[106] M. F. Frechette, I. Preda, R. Veillette, and P. Moraille, "AFM as a tool for probing HV insulation systems involving nanodielectrics," in *EIC 2014 - Proceedings of the 32nd Electrical Insulation Conference*, 2014.

[107] C. Riedel *et al.*, "Nanodielectric mapping of a model polystyrene-poly(vinyl acetate) blend by electrostatic force microscopy," *Phys. Rev. E - Stat. Nonlinear, Soft Matter Phys.*, 2010.

[108] D. El Khoury *et al.*, "Characterization of Dielectric Nanocomposites with Electrostatic Force Microscopy," *Scanning*, 2017.

[109] D. El Khoury, R. Arinero, J. C. Laurentie, M. Bechelany, M. Ramonda, and J. Castellon, "Electrostatic force microscopy for the accurate characterization of interphases in nanocomposites," *Beilstein J. Nanotechnol.*, 2018.

[110] S. Peng, Q. Zeng, X. Yang, J. Hu, X. Qiu, and J. He, "Local Dielectric Property Detection of the Interface between Nanoparticle and Polymer in Nanocomposite Dielectrics," *Sci. Rep.*, 2016.

[111] D. El Khoury, R. Arinero, J. C. Laurentie, and J. Castellon, "Nanoscale surface charge detection in epoxy resin materials using electrostatic force spectroscopy," *AIP Adv.*, 2016.

[112] J. Deschler, J. Seiler, and J. Kindersberger, "Detection of charges at the interphase of polymeric nanocomposites," *IEEE Trans. Dielectr. Electr. Insul.*, 2017.

[113] C. E. Sroog, "Commentary: Reflections on 'Aromatic Polypyromellitimides from Aromatic Polyamic Acids,' by C. E. Sroog, A. L. Endrey, S. V. Abramo, C. E. Berr, W. M. Edwards, and K. L. Olivier, J. Polym. Sci. A., 3, 1373 (1965)," *J. Polym. Sci. Part A Polym. Chem.*, 1996.

[114] G. Hougham, G. Tesoro, and J. Shaw, "Synthesis and Properties of Highly Fluorinated Polyimides," *Macromolecules*, 1994.

[115] M. K. Ghosh and K. L. Mittal, *Polyimides: Fundamentals and applications*. 2018.

[116] A. L. Endrey, "Process for Preparing Polyimides by Treating Polyamides- Acids with Lower Fatty Monocarboxylic Acid Anhydrides, E. I. Du Pont de Nemours and Company, US Patent No. 3179630," 1965.

[117] A. L. Endrey, "Ammonium Salts of Aromatic Polyamides-Acids and Process for Preparing Polyimides Therefrom, E. I. Du Pont de Nemours and Company, US Patent No. 3242136, 1966."

[118] C. E. Sroog, "Polyimides," *Prog. Polym. Sci.*, vol. Vol. 16, no. No. 4, pp. 561–694, 1991.

[119] G. M. Sessler, B. Hahn, and D. Y. Yoon, "Electrical conduction in polyimide films," *J. Appl. Phys.*, 1986.

[120] J. R. Hanscomb and J. H. Calderwood, "Thermally assisted tunnelling in polyimide film under steady-state and transient conditions," *J. Phys. D. Appl. Phys.*, 1973.

[121] S. Diaham, M. L. Locatelli, and T. Lebey, "Conductivity spectroscopy in aromatic polyimide from 200 to 400 °c," *Appl. Phys. Lett.*, 2007.

[122] K. Iida, S. Nakamura, and G. Sawa, "Dielectric breakdown and molecular orientation of Poly(4,4′-oxydiphenylene pyromellitimide)," *Jpn. J. Appl. Phys.*, 1994.

[123] K. Miyairi, "Frequency dependent dielectric breakdown of thin polyimide films prepared by vapor deposition polymerization," *Japanese J. Appl. Physics, Part 1 Regul. Pap. Short Notes Rev. Pap.*, 2001.

[124] W. D. Liu, B. K. Zhu, J. Zhang, and Y. Y. Xu, "Preparation and dielectric properties of polyimide/silica nanocomposite films prepared from sol-gel and blending process,"

Polym. Adv. Technol., 2007.

[125] Y. Cao and P. C. Irwin, "The electrical conduction in polyimide nanocomposites," in *Conference on Electrical Insulation and Dielectric Phenomena (CEIDP), Annual Report*, 2003.

[126] H. Li, G. Liu, B. Liu, W. Chen, and S. Chen, "Dielectric properties of polyimide/Al2O3 hybrids synthesized by in-situ polymerization," *Mater. Lett.*, 2007.

[127] S. Diaham, F. Saysouk, M. L. Locatelli, and T. Lebey, "Huge improvements of electrical conduction and dielectric breakdown in polyimide/BN nanocomposites," *IEEE Trans. Dielectr. Electr. Insul.*, 2016.

[128] W. Yang, R. Yi, X. Yang, M. Xu, S. Hui, and X. Cao, "Effect of particle size and dispersion on dielectric properties in ZnO/epoxy resin composites," *Trans. Electr. Electron. Mater.*, 2012.

[129] M. Houssat, N. Lahoud Dignat, J. P. Cambronne, and S. Diaham, "AFM Measurements of Polyimide/Silicon Nitride Nanocomposite Interphase," *IEEE Trans. Nanotechnol.*, 2018.

[130] C. Menguy, "Mesure des Caractéristiques des Matériaux Isolants Solides," *Tech. l'Ing nieur, Trait. G nie Electrique, Artic. D 2310*, 1997.

[131] V. V. Daniel, *"Dielectric Relaxation", Academic Press, London and New York*. 1967.

[132] A. K. Jonscher, *"Dielectric Relaxation in Solids", Chelsea Dielectrics Press, London*. 1983.

[133] American Society for Testing and Materials, *ASTM D149-97a (2004) : Standard Test Method for Dielectric Breakdown Voltage and Dielectric Strength of Solid Electrical Insulating Materials at Commercial Power Frequencies*. 2004.

[134] L.A.Dissado, J.C.Fothergill, and R.M.Hill, "Weibull statistic breakdown ; theorical basis, applications and implications," *IEEE Trans. Electr. Insul. Vol. 19, n°3. June 1984*.

[135] W. Weibull, "A Statistical Distribution Function of Wide Applicability," *J. Appl. Mech.*, 1951.

[136] J.C.Fothergill, "Estimating the cumulative probability of failure data points to be plotted on Weibull and other probability paper," *IEEE Trans. Electr. Insul. Vol. 25 No 3, pp 489-492, June 1990*.

[137] P. Goodhew, J. Humphreys, and R. Beanland, "2. Electrons and their interaction with the specimen," *Electron Microsc. Anal.*, 2001.

[138] S. Burany, " Scanning Electron Microscopy and X-Ray Microanalysis . J. Goldstein, D. Newbury, D. Joy, C, Lyman, P. Echlin, E. Lifshin, L. Sawyer, and J. Michael. Kluwer Academic, Plenum Publishers, New York; 2003, 688 pages (Hardback, $75.00) ISBN 0-

306-47292-9 ,” *Microsc. Microanal.*, 2003.

[139] G. Binning, H. Rohrer, C. Gerber, and E. Weibel, “Surface studies by scanning tunneling microscopy,” *Phys. Rev. Lett.*, 1982.

[140] G. Binnig and C. F. Quate, “Atomic Force Microscope.pdf,” *Physical Review Letters*. 1985.

[141] U. of H. groupe of Prof. Dr. Roland Wiesendanger, “Atomic force microscopy.” [Online]. Available: http://www.nanoscience.de/HTML/methods/afm.html.

[142] “Fundamentals of Contact Mode and TappingMode Atomic Force Microscopy Sponsored by Bruker Nano Surfaces.” [Online]. Available: https://www.azonano.com/article.aspx?ArticleID=3010.

[143] Bruker, “Application Note # 133 Introduction to Bruker ’ s ScanAsyst and PeakForce Tapping AFM Technology,” *Bruker Appl. Note*, 2011.

[144] Q. Zhong, D. Inniss, K. Kjoller, and V. B. Elings, “Fractured polymer/silica fiber surface studied by tapping mode atomic force microscopy,” *Surf. Sci.*, 1993.

[145] I. Advanced surface Microscopy, “Phase imaging/Chemical Mapping.” [Online]. Available: https://www.asmicro.com/Applications/phase.htm.

[146] T. J. Young, M. A. Monclus, T. L. Burnett, W. R. Broughton, S. L. Ogin, and P. A. Smith, “The use of the PeakForceTM quantitative nanomechanical mapping AFM-based method for high-resolution Young’s modulus measurement of polymers,” *Meas. Sci. Technol.*, 2011.

[147] Bruker Corporation, “PeakForce Tapping & QNM,” *Guide to SPM and AFM modes*, 2011. .

[148] B. Pittenger, N. Erina, and C. Su, *Mechanical Property Mapping at the Nanoscale Using PeakForce QNM Scanning Probe Technique BT - Nanomechanical Analysis of High Performance Materials*. 2014.

[149] B. Pittenger, N. Erina, and C. Su, “Quantitative Mechanical Property Mapping at the Nanoscale with PeakForce QNM,” *Bruker Application Note AN128*. 2010.

[150] HD MicroSystems, “‘PI-2600 Series – Low Stress Applications’ Product Bulletin,” *Stress Int. J. Biol. Stress*, 2011.

[151] “Bruker Afm Probes.” [Online]. Available: https://www.brukerafmprobes.com/p-3915-rtespa-525.aspx.

[152] H. R. Hertz., “Ueber die beruehrung elastischer koerper (on contact between elastic bodies). Gesammelte Werke (Collected Works),” 1895, p. 1:155.

[153] B. V. Derjaguin, V. M. Muller, and Y. P. Toporov, “Effect of contact deformations on the

adhesion of particles," *J. Colloid Interface Sci.*, 1975.

[154] K. L. Johnson, K. Kendall, and A. D. Roberts, "Surface Energy and the Contact of Elastic Solids," *Proc. R. Soc. A Math. Phys. Eng. Sci.*, 1971.

[155] I. N. Sneddon, "The relation between load and penetration in the axisymmetric boussinesq problem for a punch of arbitrary profile," *Int. J. Eng. Sci.*, 1965.

[156] M. E. Dokukin and I. Sokolov, "Quantitative mapping of the elastic modulus of soft materials with HarmoniX and PeakForce QNM AFM modes," *Langmuir*, 2012.

[157] M. E. Dokukin and I. Sokolov, "On the measurements of rigidity modulus of soft materials in nanoindentation experiments at small depth," *Macromolecules*, 2012.

[158] D. Tabor, "International Conference on Colloids and Surfaces Surface forces and surface interactions," *J. Colloid Interface Sci.*, 1977.

[159] M. Houssat, N. L. Dignat, C. Villeneuve-Faure, and L. P. Cambronne, "Impact of particles surface functionalization on interphase properties of PI/Si3N4 nanocomposites using AFM," in *2018 IEEE 13th Nanotechnology Materials and Devices Conference, NMDC 2018*, 2019.

[160] J. L. Hutter and J. Bechhoefer, "Calibration of atomic-force microscope tips," *Rev. Sci. Instrum.*, 1993.

[161] B. Ohler, "Practical Advice on the Determination of Cantilever Spring Constants," *Spring*, 2007.

[162] J. E. Sader, I. Larson, P. Mulvaney, and L. R. White, "Method for the calibration of atomic force microscope cantilevers," *Rev. Sci. Instrum.*, 1995.

[163] J. E. Sader *et al.*, "Spring constant calibration of atomic force microscope cantilevers of arbitrary shape," in *Review of Scientific Instruments*, 2012.

[164] J. E. Sader, J. W. M. Chon, and P. Mulvaney, "Calibration of rectangular atomic force microscope cantilevers," *Rev. Sci. Instrum.*, 1999.

[165] J. E. Sader., "http://sadermethod.org." .

[166] Y. Martin, C. C. Williams, and H. K. Wickramasinghe, "Atomic force microscope-force mapping and profiling on a sub 100-Å scale," *J. Appl. Phys.*, 1987.

[167] Y. Martin, D. W. Abraham, and H. K. Wickramasinghe, "High-resolution capacitance measurement and potentiometry by force microscopy," *Appl. Phys. Lett.*, 1988.

[168] L. Fumagalli, M. A. Edwards, and G. Gomila, "Quantitative electrostatic force microscopy with sharp silicon tips," *Nanotechnology*, 2014.

[169] C. Riedel, "Dielectric and Mechanical Properties of Polymers at Macro and Nanoscale " PhD, Université Montpellier 2," 2010.

[170] C. Riedel *et al.*, "Determination of the nanoscale dielectric constant by means of a double pass method using electrostatic force microscopy," *J. Appl. Phys.*, 2009.

[171] E. Sacher, "Dielectric properties of polyimide film, I. ac properties," *IEEE Trans. Electr. Insul.*, 1978.

[172] R. Kochetov, T. Andritsch, P. H. F. Morshuis, and J. J. Smit, "Impact of postcuring and water absorption on the dielectric response of epoxy-based composites filled with MgO nanoparticles," in *Annual Report - Conference on Electrical Insulation and Dielectric Phenomena, CEIDP*, 2011.

[173] S. Singha and M. J. Thomas, "Dielectric properties of epoxy-Al2O3 nanocomposite system for packaging applications," *IEEE Trans. Components Packag. Technol.*, 2010.

[174] S. Singha and M. J. Thomas, "Dielectric Properties of Epoxy-<formula formulatype="inline"> <img src="/images/tex/19216.gif" alt="{\rm Al}_{2}{\rm O}_{3}"> </formula> Nanocomposite System for Packaging Applications," *Components Packag. Technol. IEEE Trans.*, 2010.

[175] S. Singha, M. Joy Thomas, and A. Kulkarni, "Complex permittivity characteristics of epoxy nanocomposites at low frequencies," *IEEE Trans. Dielectr. Electr. Insul.*, 2010.

[176] C. S. Daily, M. R. Kessler, X. Tan, and N. Bowler, "On the nanoparticle interphase," in *Annual Report - Conference on Electrical Insulation and Dielectric Phenomena, CEIDP*, 2012.

[177] M. G. Todd and F. G. Shi, "Complex permittivity of composite systems: A comprehensive interphase approach," *IEEE Trans. Dielectr. Electr. Insul.*, 2005.

[178] Z. M. Dang, H. P. Xu, and H. Y. Wang, "Significantly enhanced low-frequency dielectric permittivity in the BaTiO3/poly(vinylidene fluoride) nanocomposite," *Appl. Phys. Lett.*, 2007.

[179] Z. M. Dang, J. W. Zha, and B. H. Fan, "Low-frequency dielectric phenomena in BaTiO3/polymer nanocomposites," in *Proceedings of IEEE International Conference on Solid Dielectrics, ICSD*, 2013.

[180] C. W. Beier, M. A. Cuevas, and R. L. Brutchey, "Effect of surface modification on the dielectric properties of BaTiO 3 Nanocrystals," *Langmuir*, 2010.

[181] S. Dalle Vacche, F. Oliveira, Y. Leterrier, V. Michaud, D. Damjanovic, and J. A. E. Månson, "Effect of silane coupling agent on the morphology, structure, and properties of poly(vinylidene fluoride-trifluoroethylene)/BaTiO3 composites," *J. Mater. Sci.*, 2014.

[182] "S. Diaham, Etude du comportement sous haute température de matériaux polyimides en vue de la passivation de composants de puissance   semi-conducteurs grand gap, PhD

thesis, University of Toulouse,France, 2007."

[183] Y. Ito, M. Hikita, T. Kimura, and T. Mizutani, "Effect of Degree of Imidization in Polyimide Thin Films Prepared by Vapor Deposition Polymerization on the Electrical Conduction," *Jpn. J. Appl. Phys.*, 1990.

[184] G. Sawa, K. Iida, S. Nakamura, and M. Ieda, "Transient current of polyimide in the time range 10-4-101 sec at temperatures 180-280°c," *IEEE Trans. Electr. Insul.*, 1980.

[185] F. Tian, Q. Lei, X. Wang, and Y. Wang, "Effect of deep trapping states on space charge suppression in polyethylene/ZnO nanocomposite," *Appl. Phys. Lett.*, 2011.

[186] F. N. Alhabill, R. Ayoob, T. Andritsch, and A. S. Vaughan, "Introducing particle interphase model for describing the electrical behaviour of nanodielectrics," *Mater. Des.*, 2018.

[187] X. Wang and Y. Hu, "Modified silicon nitride nanopowder coating and its influence on the dynamic mechanical property of Polymethyl Methacrylate Nanocomposite," *Polym. Polym. Compos.*, 2017.

[188] Y. Liu, Y. Li, X. M. Li, and T. He, "Kinetics of (3-aminopropyl)triethoxylsilane (aptes) silanization of superparamagnetic iron oxide nanoparticles," *Langmuir*, 2013.

[189] D. Fabiani *et al.*, "Effect of water adsorption on the dielectric properties of polymer nanocomposites," in *Proceedings of the International Symposium on Electrical Insulating Materials*, 2008.

List of figures

List of tables